



Western Michigan University
ScholarWorks at WMU

Masters Theses

Graduate College

12-2018

Design of a Portable Biogas Purification and Storage System

Anilkumar Kosna
Western Michigan University

Follow this and additional works at: https://scholarworks.wmich.edu/masters_theses



Part of the Mechanical Engineering Commons

Recommended Citation

Kosna, Anilkumar, "Design of a Portable Biogas Purification and Storage System" (2018). *Masters Theses*. 3801.

https://scholarworks.wmich.edu/masters_theses/3801

This Masters Thesis-Open Access is brought to you for free and open access by the Graduate College at ScholarWorks at WMU. It has been accepted for inclusion in Masters Theses by an authorized administrator of ScholarWorks at WMU. For more information, please contact wmu-scholarworks@wmich.edu.



DESIGN OF A PORTABLE BIOGAS PURIFICATION AND STORAGE SYSTEM

by

Anilkumar Kosna

A thesis is submitted to the Graduate College
in partial fulfillment of the requirements
for the degree of Master of Science in Engineering (Mechanical)
Mechanical and Aerospace Engineering
Western Michigan University
December 2018

Thesis Committee:

Bade Shrestha, Ph.D., Chair.
HoSung Lee, Ph.D.
Chris Cho, Ph.D.

© 2018 Anilkumar Kosna

ACKNOWLEDGMENTS

This work was supported by funds from the Faculty Research and Creative Activities Award, Western Michigan University. I would also like to acknowledge the support provided by Mechanical and Aerospace department, WMU.

I would be grateful for my thesis advisor Dr. Bade Shrestha for giving me an opportunity to work on this project. I would like to thank for his efforts to understand the logical reasoning behind my work and the motivation to get the best out of it. I am thankful to my committee members Dr. HoSung Lee and Dr. Chris Cho for their valuable suggestions and encouragement. I would like to use this opportunity to thank all MAE professors of Western Michigan University for their guidance and support through my journey.

I thank Richard Sackett (Auto Lab Supervisor), Peter Thannhauser (Lab Technician senior), Mike Konkel (Faculty Specialist), Glenn Hall (Lab Technician), Tony Cekola (Alliance Air US LLC), and Brian Edgington (Depatie Fluid Power Company) for their help in experimental setup. I would like to acknowledge undergraduate students Brandon Rodney Nimtz, Trevor Richardson, Kenton A Vogel, Sterling Phillip Fulton, Tyler Jeffrey Huffman, and Ian Mitchell Cole for their help in this research.

Finally, I would like to thank my parents, brother and my friends especially Meena Madhuri Gandu Vijayakumar for their support, motivation, and belief in me. Without their support, it would not be completed.

Anilkumar Kosna

DESIGN OF A PORTABLE BIOGAS PURIFICATION AND STORAGE SYSTEM

Anilkumar Kosna, M.S.E.

Western Michigan University, 2018

Biogas is produced from the decomposition of organic materials like manure, sewage sludge or crop fodders in anaerobic digesters. It consists mainly of 40 – 75 % of methane (CH_4), 15 – 60 % of carbon dioxide (CO_2) and trace amounts of other components. The principle constituents of biogas are similar to natural gas. Natural gas has 87 – 97 % of methane (CH_4) and 0.1 – 1 % of carbon dioxide. Natural gas is known to be an alternative fuel with a wide range of applications. The commercial purification technologies exist for large-scale biogas units. However, there are no such commercial purification technologies available for small biogas units (farm scale or household). The aim of this project is to propose a commercial portable purification and storage system for small biogas units that can be handled by a single person. This portable technology will provide an opportunity to generate an extra income source to the deprived and poor biogas unit owners, who are often located in the very poor and deprived areas where even general transportations may not be available.

This work has identified and designed the components required for the proposed portable purification and storage system and their components. The proposed system has two compressors, two heat exchangers, a liquid-gas separator and a storage tank, with a total portable weight of about 12 kg excluding the storage tank. The system is capable of purifying 15 kg of biogas per hour producing and storing 4 kg of biomethane. The numerical simulation of each individual component to validate the proposed purification method are also presented and discussed.

TABLE OF CONTENTS

ACKNOWLEDGMENTS	ii
LIST OF TABLES	vi
LIST OF FIGURES	viii
NOMENCLATURE	xi
CHAPTER	
1 INTRODUCTION	1
1.1 Biogas.....	3
1.2 Biogas production	6
1.3 Commercial biogas plants and purification systems	6
1.3.1 Water/ polyethylene glycol scrubbing	8
1.3.2 Chemical absorption/ amine scrubbing.....	9
1.3.3 Pressure swing adsorption.....	9
1.3.4 Membrane separation.....	10
1.3.5 Cryogenic separation	11
1.4 Non-commercial/ household biogas plants	12
1.5 Thesis objective.....	13
2 LITERATURE REVIEW	14
3 THERMOPHYSICAL PROPERTIES AND EQUATION OF STATE OF BIOGAS.....	17
3.1 Equation of state of biogas	21
4 EXPERIMENTAL VALIDATION OF EQUATION OF STATE OF BIOGAS.....	28

Table of Contents - Continued

CHAPTER

4.1	Experiment setup.....	28
4.1.1	Gas mixing equipment	29
4.1.2	Accumulator.....	30
4.1.3	Reciprocating compressor.....	30
4.1.4	Liquid – Gas Separator	31
4.1.5	Cooling system.....	32
4.1.6	Data acquisition system	33
4.2	Experimental procedure	34
4.3	Validation of equation of state of CO ₂ – CH ₄ binary mixture	34
5	PURIFICATION PROCESS AND COMPONENTS DESIGN	39
5.1	Purification process design.....	39
5.1.1	Process 1-2 compression.....	41
5.1.2	Process 2-4 isobaric heat rejection.....	41
5.1.3	Process 4-5 liquid – gas separation	42
5.1.4	Process 5-6 isentropic compression process	43
5.1.5	Efficiency of the purification system	43
5.2	Compressor design and finite element analysis	44
5.2.1	Design	46
5.2.2	FEA structural analysis	62
5.3	Heat exchanger design and conjugate heat transfer analysis	66
5.3.1	The optimum design of tube-fin heat exchanger	67

Table of Contents - Continued

CHAPTER	
5.3.2	CFD Conjugate heat transfer analysis..... 74
5.4	Liquid-Gas separator design and multi-phase analysis 82
5.4.1	Design 83
5.4.2	CFD multi-phase Analysis..... 88
5.5	Light-weight storage tank design and FEA composite analysis 93
5.5.1	Design 94
5.5.2	FEA composite analysis..... 99
6	SUMMARY AND CONCLUSION 106
7	FUTURE SCOPE..... 109
REFERENCES 110

LIST OF TABLES

1-1 Biogas yield and methane composition of various feedstock's [10]	5
1-2 Biogas composition and properties [14]	7
1-3 Domestic biogas plants in major countries	12
3-1 Properties of pure CO ₂ and CH ₄	18
3-2 Empirical constants of specific heat at constant pressure	18
3-3 Empirical constants of dynamic viscosity	19
3-4 Properties of biogas	19
3-5 Various equation of state (EOS) models	21
4-1 Specifications of commercial compressor	31
4-2 Specifications of Liquid-Gas separator	32
4-3 Inputs of the experiment	34
4-4 Properties of fluid after compression	36
4-5 Saturated vapor properties of the mixtures at specified specific volume	36
4-6 Comparison of theoretical and experimental saturated pressures	38
5-1 Input parameters of compressors	44
5-2 Design parameters of the compressors	49
5-3 Input parameters for piston design	52
5-4 Final dimensions for the piston design	53
5-5 Input parameters required for connecting rod design	57
5-6 Final design parameters of connecting rods	57
5-7 Final design of crankshafts	61
5-8 Specifications of commercial electric motor	65
5-9 design requirements of heat exchangers	66
5-10 Properties of biogas at film temperatures	71
5-11 Properties of convective fluids at inlet temperatures	71
5-12 Final input properties of heat exchangers	72

List of Tables - Continued

5-13 Output properties of the heat exchangers	72
5-14 Final dimensions of the heat exchangers	73
5-15 Domain setup	77
5-16 Boundary conditions	77
5-17 Fluid solid interface	78
5-18 Validation of ANSYS - CFX simulation results with Mathcad design	82
5-19 Input parameters required for LGS design	87
5-20 Final parameters of LGS	87
5-21 Boundary conditions	91
5-22 Design parameters of storage tank	94
5-23 CNG tank weight	95
5-24 Properties of CFRP and GFRP	96
5-25 Properties of the aluminum liner	96
5-26 Final properties of the pressure vessel	98
6-1 Weight of portable biogas purification system	107

LIST OF FIGURES

1-1 Commercial energy usage [6].....	2
1-2 Anaerobic digestion process [9]	4
1-3 Water/Polyethylene scrubbing.....	8
1-4 Amine scrubbing.....	9
1-5 Pressure swing adsorption	10
1-6 Membrane separation	11
1-7 Cryogenic separation	11
3-1 Specific heat at constant pressure (J/kg*K) vs temperature	20
3-2 Specific heat at constant volume (J/kg*K) vs temperature	20
3-3 Dynamic viscosity (kg/m*s) vs temperature	21
3-4 P-V diagram of pure CO ₂	23
3-5 P-V diagram of pure CH ₄	24
3-6 P – V diagram of 50% methane and 50% carbon dioxide mixture	26
3-7 Critical temperature vs CO ₂ mole fraction	26
3-8 Critical pressure vs CO ₂ mole fraction	27
3-9 Critical specific volume vs CO ₂ mole fraction	27
4-1 Layout schematic of the experiment setup	28
4-2 Gas mixing equipment.....	29
4-3 Accumulator	30
4-4 Multi-stage reciprocating compressor	31
4-5 Liquid – Gas Separator	32
4-6 Data acquisition equipment	33
4-7 Pressure rise vs time	35
4-8 Temperature rise vs time	35
4-9 Experimental pressure drop vs temperature.	37

List of Figures - Continued

5-1 Equation of state of CO ₂ of CO ₂ – CH ₄ binary mixture	39
5-2 Portable biogas purification system design	40
5-3 Types of compressors	45
5-4 Parts of compressor [29].....	46
5-5 Thermodynamic compression cycle	47
5-6 Piston parameters [32]	50
5-7 Piston-1 2D and 3D models.....	54
5-8 Piston-2 2D and 3D models.....	54
5-9 Cross- section of a connecting rod [32].....	55
5-10 2D and 3D models of the connecting rod 1 and 2	58
5-11 crankshaft.....	59
5-12 2D and 3D models of the crankshaft 1 and 2	61
5-13 Compressor 1 and 2 assemblies.....	62
5-14 Meshing and boundary conditions (pressures and fixtures applied) assemblies	62
5-15 Von-Misses stresses of compressor assembly	63
5-16 Factor of safety for compressor 1 and 2	63
5-17 Final assemblies of compressors 1 and 2.....	64
5-18 Typical reed valve geometry	65
5-19 Classification of heat exchangers based on their construction	66
5-20 Tube-fin heat exchanger	67
5-21 Process flow of the optimal tube – fin design	70
5-22 3D models of heat exchanger 1 and 2.....	74
5-23 Heat exchanger geometry	75
5-24 Heat exchanger meshing.....	76
5-25 Problem setup	76
5-26 Convergence criteria and workflow	78
5-27 Contours of biogas temperature in HE1	79

List of Figures - Continued

5-28	Contours of biogas temperature in HE2	79
5-29	Temperature contours of convective fluid 1 (air) at the outlet	80
5-30	Contours of convective fluid 2 (expanded liquid CO ₂) temperature at the outlet	80
5-31	Velocity vectors of convective fluid 1	81
5-32	Velocity vectors of convective fluid 2	81
5-33	Types of Liquid-Gas Separators	82
5-34	Gravity Liquid-Gas Separator [38]	83
5-35	2D and 3D model of LGS	88
5-36	a) Imported fluid CAD geometry with named selections and b) Fine mesh	89
5-37	a) Problem setup tree and b) fluid domain with the boundary conditions	89
5-38	Fluid domain setup	90
5-39	Velocity vectors of CH ₄ gas	91
5-40	Velocity vectors of CO ₂ liquid	92
5-41	Volume fraction of CH ₄ gas and CO ₂ liquid	92
5-42	Types of CNG pressure vessels	93
5-43	2D and 3D model of the spherical pressure vessel	99
5-44	ANSYS project schematic	99
5-45	Materials assigned to ACP-Pre and Mechanical model	100
5-46	a) Pressure vessel surface and b) Solid pressure vessel polar opening	101
5-47	a) ACP mesh model and b) Mechanical mesh model	101
5-48	ACP problem setup	102
5-49	Composite laminate	103
5-50	ACP-Pre and mechanical model assembly	104
5-51	a) Boundary conditions and b) Burst pressure	104
5-52	Von-Misses stresses of pressure vessel	105

NOMENCLATURE

a	fin width (m)
A_p	droplet projected area (m^2)
A_t	total heat transfer area (m^2)
A_f	fin area (m^2)
$A_{required}$	required area (m^2)
b_1	width of top land (m)
b_2	width of the other land (m)
b_m	repulsion parameter
B	bore (m)
C_p	specific heat at constant pressure ($\frac{kJ}{kg.K}$)
C_v	specific heat at constant volume ($\frac{kJ}{kg.K}$)
CF	correction factor
CR	compression ratio
C_d	coefficient of drag
d_i	inside diameter of pin (m)
d_c	crank pin diameter (m)
d_s	diameter of the shaft (m)
d_o	outside diameter of a pin (m)
D_p	droplet diameter (m)
D_{Vmin}	minimum vessel diameter (m)
D_o	outer tube diameter (m)
D_{lo}	liquid outlet diameter (m)
D_{go}	gas outlet diameter (m)

E	young's modulus (Pa)
F_g	gravity force (N)
F_d	drag force (N)
FS	safety factor
F_b	bearing load (N)
F_g	load by compressed gas (N)
g	acceleration due to gravity ($\frac{m}{s^2}$)
$h_{convective}$	convective heat transfer coefficient ($\frac{W}{m^2.K}$)
H_1, H_2	reaction forces (N)
I_{xx}	moment of inertia of the about X-axis ($kg.m^2$)
I_{yy}	moment of inertia of the about Y-axis ($kg.m^2$)
k_{ij}	binary interaction parameter
k_{xx}	radius of gyration
k	thermal conductivity ($\frac{W}{m.K}$)
K_s	design parameter
l_1	length of the piston (m)
L_l	liquid space (m)
L_g	gas space (m)
L_C	length of the connecting rod (m)
L	length of the piston (m)
L_s	length of the piston skirt (m)
LHV_{CH_4}	lower heating value ($\frac{MJ}{kg}$)
m_a	mass fraction
m	total mass of mixture (kg)
m_i	mass of individual gas (kg)
M_i	molecular weight ($\frac{kg}{kmol}$)
\dot{m}	mass flow rate ($\frac{kg}{s}$)

m_p	mass of the pipe (kg)
m_f	mass of the fin (kg)
m_{he}	mass of heat exchanger (kg)
M_c	bending moment ($N.m$)
n_r	number of rings
P_d	discharge pressure (Pa)
P_w	gas pressure on cylinder walls (Pa)
P_b	bearing pressure (Pa)
P_{allow}	allowable pressure (Pa)
Pr	Prandtl number
ΔP	pressure drop (Pa)
P_l	pressure capability of liner (Pa)
P_{burst}	burst pressure (Pa)
P_w	working pressure (Pa)
P_c	composite design pressure (Pa)
Q_{dis}	heat dissipation (W)
r	radius (m)
R	ideal gas constant ($\frac{kJ}{kg.K}$)
R_0	universal gas constant ($\frac{kJ}{kmol.K}$)
Re	Reynolds number
S	stroke (m)
t_H	thickness of piston head (m)
t_1	radial thickness (m)
t_2	axial thickness (m)
t_3	piston barrel thickness at open end (m)
t_4	piston barrel thickness at other end (m)
t	crank web thickness (m)
t_v	vessel thickness (m)
t_l	liner thickness (m)

T_0	outlet temperature (K)
T_{inf}	convective fluid temperature (K)
U_∞	convective fluid velocity ($\frac{m}{s}$)
V	specific volume ($\frac{m^3}{kg}$)
V_{dot}	volumetric flow rate ($\frac{m^3}{s}$)
V_{gmax}	maximum gas velocity ($\frac{m}{s}$)
V_d	displacement volume (m^3)
V_p	volume of the spherical droplet (m^3)
V_{dotl}	liquid volumetric flow rate ($\frac{m^3}{s}$)
V_{dotg}	gas volumetric flow rate ($\frac{m^3}{s}$)
V_{l0}	liquid velocity ($\frac{m}{s}$)
V_{g0}	gas velocity ($\frac{m}{s}$)
V_{df}	design factor
W_{isen}	isentropic work (W)
W_r	required work (W)
W_B	buckling load (N)
W	pipe length (m)
W_{req}	length of the pipe required (m)
Z_{opt}	optimum spacing (m)

Greek symbols

γ	specific heat ratio
μ	dynamic viscosity ($\frac{kg}{m.s}$)
μ_o	reference viscosity at reference temperature ($\frac{kg}{m.s}$)
ρ	density ($\frac{kg}{m^3}$)

ω	acentric factor
σ_c	compressive yield strength (Pa)
σ_{yield}	yield strength (Pa)
η	efficiency
η_f	fin efficiency
η_o	overall surface efficiency
f	fanning friction factor
v_d	design velocity ($\frac{m}{s}$)
ν	kinematic viscosity ($\frac{m^2}{s}$)

1 INTRODUCTION

The population growth and fast urbanization increase the utilization of conventional energy sources based on oil, coal and natural gas, which results in an increase in energy demand as well as the environmental problems such as global warming and climate changes [1]. The energy resources of individual countries have a significant impact on its economy. The centralized energy resources in some countries raise the prices and taxes of conventional fuels. This increase in prices and taxes of conventional fuel affects the economies of developing and underdeveloped countries [2], which eventually forces to do more research on non-convectional energy sources like biomass, wind, solar, hydro and geothermal. The potential of non-conventional energy sources is enormous to support the world's energy demand. The transition of a conventional energy-based system to non-conventional energy-based system is necessary to protect the environment and stability of the economies of countries. The contribution of non-conventional sources in present world's energy demand is between 15 to 20 percent [3].

The developing countries of Africa, Asia, and South America are using most of the non-conventional energy supply from fuelwood for cooking and heating [4] [5]. The hydropower contributes nearly 20 percent of the global electrical power supply. The other renewable energy sources like solar energy, wind energy, bio-energy, geothermal energy, and small hydropower are contributing 2 percent of global energy demand. The present environmental policies and research studies show that the contribution of renewable sources is going to increase from 20 to 50 percent by the second half of the 21st century with the right policies in place [6]. The biomass energy is playing a key role in non-conventional energy supply. Biomass represents all the organic material (plants, trees, algae, etc.) which essentially collects and stores the sun's energy through photosynthesis. The conversion of biomass to useful forms of energy such as heat, electricity and liquid fuels is called bioenergy or biomass energy. Bioenergy was the first energy source in human civilization, firewood has been the primary fuel for centuries. From the industrial revolution, the efficient techniques were developed to extract and burn fossil fuels, then the biomass was replaced by fuels such as oil, coal, and natural gas. Although fossil fuels replaced biomass energy, developing countries still rely on it and it is the fourth

largest source of energy with an estimate of 10 to 14 percent. Where, oil (33 percent), coal (21 percent), and natural gas (19 percent) stand as the largest primary sources of energy [6]. The United Nations intergovernmental panel on climate change (IPCC) study has explained the 21st century's growing energy demand of the world for five scenarios. These five scenarios were developed for three different cases as follows, energy utilization of world, industrialized countries and the developing countries. Figure 1-1 depicts the dominance of biomass usage in all scenarios, the contribution of carbon-neutral biomass energy as a substitute for fossil fuel helps to meet the CO₂ targets. Biomass is not considered as a modern energy, but it has a potential to be modernized by converting solid biomass into clean and conventional energy forms such as gases, liquids, or electricity over a range of household and industrial scale.

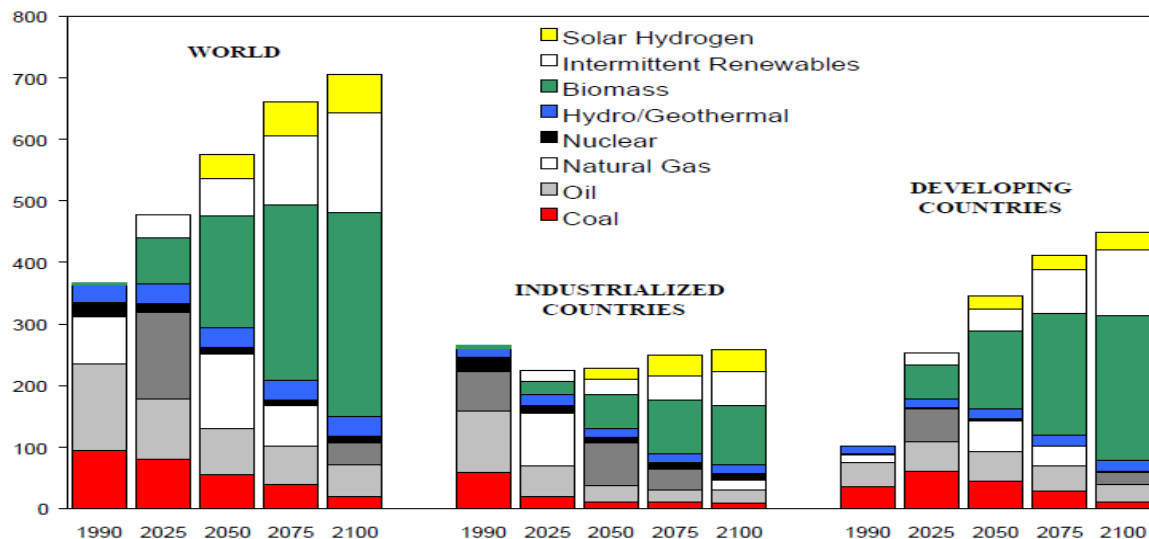


Figure 1-1 Commercial energy usage [6]

There are various methods available to convert biomass to useful conventional energy, some of those are direct combustion, gasification, liquid biofuels and anaerobic digestion of biomass. The Steam-Rankin technology uses the direct combustion of biomass to produce the electricity of capacity ranges 1-50 MW. However, the energy conversion efficiencies of direct biomass combustion process are low which is 10 to 15 percent. Gasification is a thermochemical process of producing combustible gas from biomass by burning it without sufficient air for full combustion, but with enough air to convert the solid biomass to gaseous fuel. The produced gaseous fuel consists of carbon monoxide, hydrogen,

carbon dioxide, nitrogen and it has a heating value of 4 to 6 MJ/Nm³, which is 10 to 15 percent of the heating value of natural gas. These gases can be used in modified internal combustion engines to produce 100-200 KW with efficiencies of 15 to 25 percent [6].

Liquid biofuels play a vital role in biomass utilization. These liquid biofuels have the potential to replace petroleum-based fuels which are widely used in the transportation sector. The “biodiesel” is an important liquid fuel produced from oil-producing plants such as soybeans, palm oil trees and oilseeds like rapeseed. The compounds of biodiesel are like hydrocarbon petroleum products and the lower heating value of biodiesel is in the same range of diesel. The other potential liquid biofuels alternative to petroleum-based fuels are ethanol, methanol, and hydrogen. These are produced from crops like corn, sugarcane and from lignocellulose biomass (such as wood, straw, and grass). Finally, anaerobic digestion is a process of converting organic waste into a combustible gas called biogas. Typically, biogas consists of 60 percent of methane and 40 percent of carbon dioxide with a heating value of about 55 percent of natural gas. When it’s purified, the heating value of 1 m³ purified biomethane is equal to the heating value of 0.97 m³ of natural gas [2]. It shows that the purified biogas is capable to replace natural gas. Natural gas is known to be an alternative non-renewable energy source. This feature of biogas increased the interest in research and development of biogas production and purification plants.

1.1 Biogas

Biogas is a key player in the renewable energy sector. Sun et al. show that by 2020 major part of the EU-27 renewable energy is dominated by bioenergy, mostly by biogas (at least 25% share). They also predicted that the global capacity of commercial biogas is going to rise from 14.5 Gigawatts (GW) in 2012 to 29.5 GW in 2022 [7]. Biogas is produced by the decomposition of organic material like manure, sewage sludge or crop fodders in an anaerobic digester [7]. The process of degradation of organic material in an anaerobic digester is called anaerobic (without air) digestion. There are four stages of anaerobic digestion those are hydrolysis, acidogenesis, acetogenesis, and methanogenesis [2]. Biomass is a combination of complex carbohydrates, fats, and proteins. In hydrolysis, these complex carbohydrates break down to simple sugars, amino acids and fatty acids with the help of microorganisms [2]. In the acidogenesis stage, fermentative bacteria transform simple sugars and

monomeric organic compounds into organic acids, alcohols, carbon dioxide (CO_2), hydrogen (H_2) and ammonia (NH_3). The third stage is the acetogenesis, acetogenic bacteria convert products from acidogenesis stage to hydrogen (H_2), carbon dioxide (CO_2) and acetic acid (CH_3COOH). Methanogenesis is the final stage of anaerobic digestion, methanogenic bacteria convert the products of acetogenesis stage to a mixture of methane (CH_4 , 50-75%), carbon dioxide (CO_2 , 50-75%), varying quantities of nitrogen, hydrogen sulfide, and other components. The final product of methanogenesis is called biogas [8].

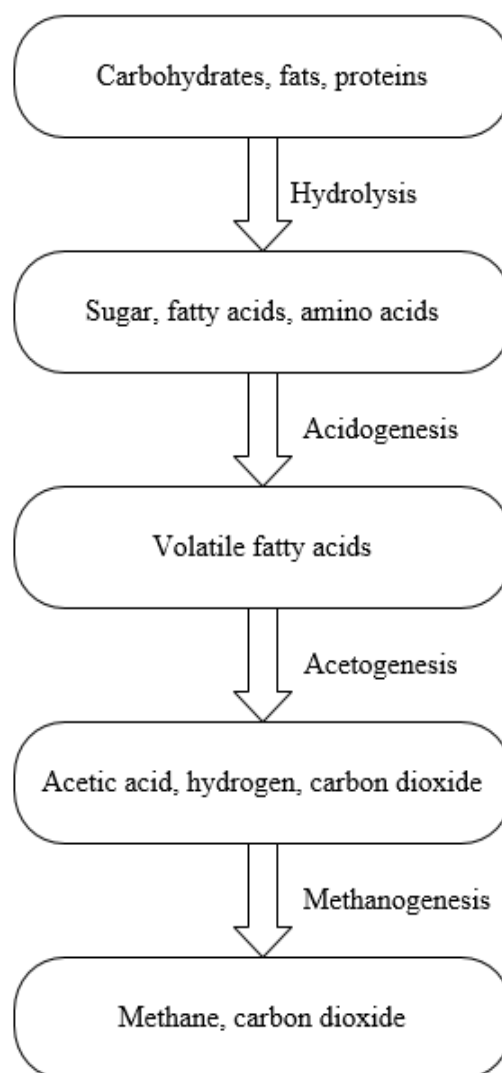


Figure 1-2 Anaerobic digestion process [9]

The anaerobic digestion takes place in distinct stages by various microorganisms. The favorable conditions of microorganism's growth improve the biogas production rate [2]. The various parameters which affect the biogas production rate are pH, temperature, mixing, C/N ratio, hydraulic retention time and substrate [2]. The favorable pH range for methanogens growth is 6.7-7.5. The growth of fermentative bacteria depends on the temperature conditions; mesophilic conditions favor the fermentative bacteria growth. Mixing is a fundamental parameter of biogas generation, excess mixing stresses the microorganisms and less mixing results foam forming. The increase and decrease of the carbon-nitrogen ratio affect biogas generation, it should be of the range 16:1 – 25:1. Hydraulic retention time (HRT) is the average time the feedstock stays in the digester to transform to biogas [9]. It should be as minimum as 10-15 days.

The substrate or feedstock is the major part of biogas production. Methane content in biogas depends upon feedstock. By theory, almost all organic materials are degradable to produce biogas of various compositions of methane [2]. The major feedstock's used in biogas production are cattle dung, pig manure, poultry waste, straw, grass silage, municipal solid waste, jatropha curcas seedcake, Pongamia pinnata seedcake, etc [10]. The biogas yield and methane content for various feedstock are shown in Table 1-1.

Table 1-1 Biogas yield and methane composition of various feedstock's [10]

Feedstock	Biogas yield (m ³ /kg)	Methane (%)
Cattle dung	0.297	55
Pig manure	0.40	65
Poultry waste	0.45	70
Straw	0.341	51
Grass silage	0.576	52
Municipal solid waste	0.308	60

1.2 Biogas production

The Global bioenergy statistics 2017 reported that the global biogas production as 58.7 billion Nm³. The top countries contributing biogas production are China (15.0 billion Nm³), USA (8.48 billion Nm³), Thailand (1.30 billion Nm³), India (0.81 billion Nm³), Canada (0.79 billion Nm³) and EU-28 (28.9 billion Nm³). EU-28 nations are dominating with the share of 49.8% whereas the production share from major continents Asia (31.9%), America (16.7%) and other continents 1.5% [11]. There are three types of biogas plants based on their sizes, those are Industrial/commercial plants, farm-scale/community plants, and household/domestic plants. The industrial/commercial biogas plants have typical capacities of >300 m³. These plants are mostly installed in EU – 28 nations. Farm-scale/community biogas plants have capacities of 100 – 250 m³, municipality waste is the major feedstock for these plants. These plants are dominated in Latin American nations [12]. Household/domestic biogas plants have typical sizes of 1-12 m³. These plants are installed in Asian countries. The main feedstock used in these digesters is household waste whereas the industrial and community biogas plants need a centralized system to collect the feedstock and maintain the plant.

1.3 Commercial biogas plants and purification systems

The European Biogas Association (EBA) reported that the EU nations have more than 15,000 industrial/community biogas plants producing 15.0 billion m³/year of biogas and more than 300 bio methane plants of production capacity 1.0 billion m³/year [13]. Bio methane is the purified form of biogas. It is produced by removing carbon dioxide, hydrogen sulfide and other gases by various commercial purification process. The purification of raw biogas increases the lower heating value, compression capabilities and decreases the transportation costs. The properties of bio methane are similar to natural gas. It can be distributed to natural gas grid, used as vehicle fuel and can be efficiently used to produce electricity.

Although the composition of biogas depends on the feedstock, it mainly consists of methane (CH₄), carbon dioxide (CO₂) and small quantities of ammonia (NH₃), hydrogen sulfide (H₂S), hydrogen (H₂), oxygen (O₂), nitrogen (N₂), carbon monoxide (CO). The comparison of raw biogas and natural gas properties are shown in Table 1-2.

Table 1-2 Biogas composition and properties [14]

Parameter	Raw biogas (vol%)	Natural gas (vol%)
Methane (CH ₄)	40 – 75 %	70 – 90 %
Hydrocarbons (C ₂ H ₆ , C ₃ H ₈ , C ₄ H ₁₀)	0 – 20 %
Carbon dioxide (CO ₂)	15 – 60 %	0 – 8 %
Hydrogen sulfide (H ₂ S)	0.005 – 2 %	0 – 5 %
Oxygen (O ₂)	0 – 1 %	0 – 0.2 %
Nitrogen (N ₂)	0 – 2 %	0 – 5 %
Carbon monoxide (CO)	< 0.6 %	0 – 4 %
Rare gases	0 – 2 %
Heating value (MJ/ N m ³)	20 – 24	34 – 39
Density (STP conditions)	1.15 kg/m ³	0.9 kg/m ³

The available commercial biogas purification methods are;

- Water/polyethylene glycol scrubbing
- Chemical absorption
- Pressure swing adsorption
- Membrane separation
- Cryogenic separation

1.3.1 Water/ polyethylene glycol scrubbing

Water/polyethylene glycol scrubbing is a physical process, this process is based on the solubility property of CO_2 and H_2S in water/polyethylene. These two gases are more soluble in water/polyethylene than methane. Figure 1-3 Shows the schematic of the process. It has two main vertical cylinders used for absorption and desorption. The absorption cylinder is fed with the pressurized biogas from the bottom and water from the top simultaneously. This process is operated counter currently [15].

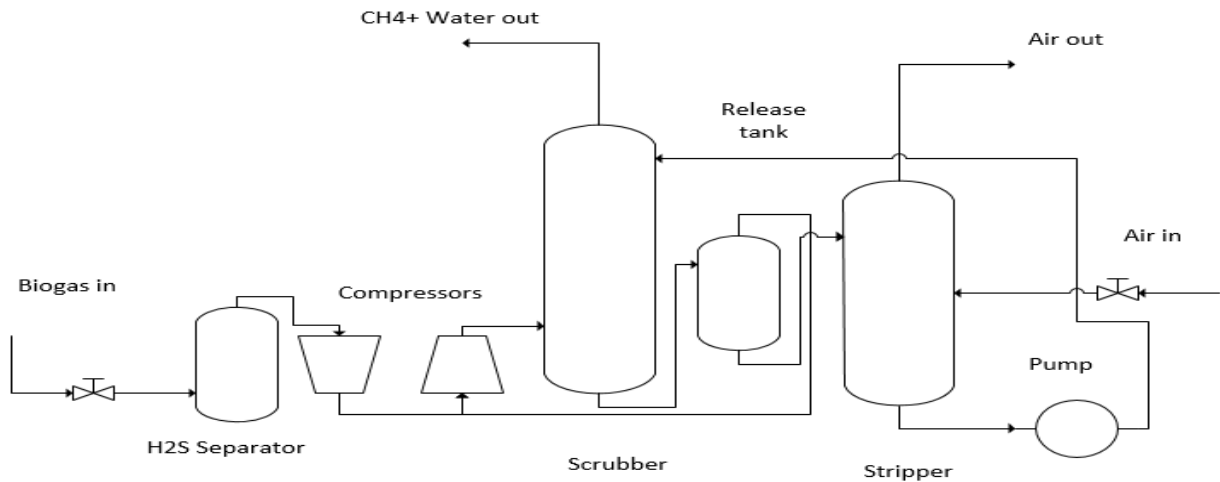


Figure 1-3 Water/Polyethylene scrubbing

The water which exits from the absorption cylinder is sent to the desorption/regeneration cylinder to remove CO_2 and H_2S . The removal of CO_2 and H_2S is accomplished by de-pressurizing or stripping with air. The advantages of water/polyethylene scrubbing are high efficiency ($>97\% \text{ CH}_4$), simultaneous removal of H_2S , capacity is adjustable by changing pressure or temperature and tolerant for impurities. The disadvantages are clogging due to bacterial growth, the possibility of foaming and low flexibility toward variation of input gas [16]. The cost of water scrubbing method is $\$0.16/\text{Nm}^3$ [15].

1.3.2 Chemical absorption/ amine scrubbing

The chemical absorption/ amine scrubbing depends on the development of reversible chemical bonds between solute and solvent in an absorption cylinder. The breakage of chemical bonds takes place in the regeneration cylinder to regenerate the solvent. The aqueous solutions of mono, di, or tri ethanolamine or the aqueous solution of sodium, potassium and calcium hydroxide are used as the solvents [15]. The advantages of chemical absorption are high efficiency ($>99\%$ CH_4), more CO_2 dissolved per unit of volume and regenerative. The main disadvantages are the expensive investments and additional chemicals required for regeneration [16]. This technique costs $\$0.21/\text{Nm}^3$ [15].

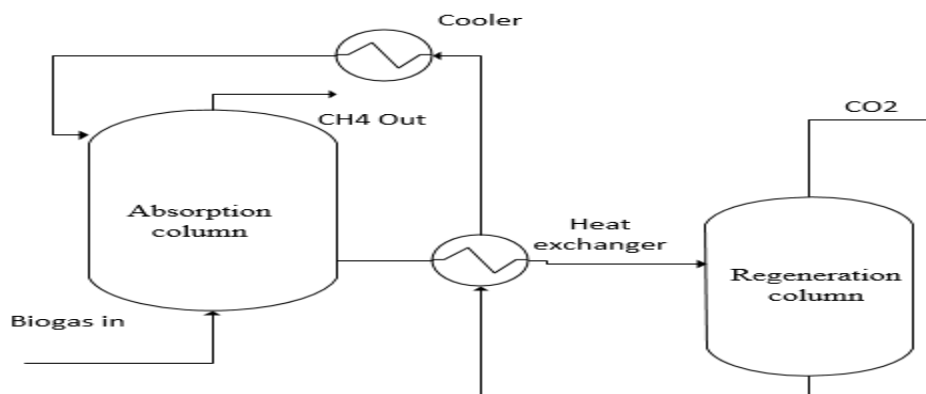


Figure 1-4 Amine scrubbing

1.3.3 Pressure swing adsorption

Pressure swing adsorption is based on the property of a material to adsorb CO_2 gas under pressure. The materials used in pressure swing adsorption are molecular sieves of zeolite and active carbon. This process needs pretreatment step to remove H_2S . After the pretreatment, the biogas is sent into the pressurized adsorption column for the extraction of CO_2 . Once the CO_2 is removed the methane-rich biogas is sent out of the column. The regeneration of molecular sieves is done by depressurizing the adsorption column for desorption. Figure 1-5 Shows the schematic of the typical pressure swing adsorption process. It has four vertical columns or cylinders to complete adsorption and desorption

stages concurrently. The typical pressure and temperature of adsorption column are 7 to 8 bar and 50 to 70 °C [15]. The advantages are efficient purification (95-98% CH₄), it can be used for small capacities and tolerant to impurities. The disadvantages are expensive investment and operation and it needs costly process control [16]. The typical cost of this process is \$0.49/N m³ [15].

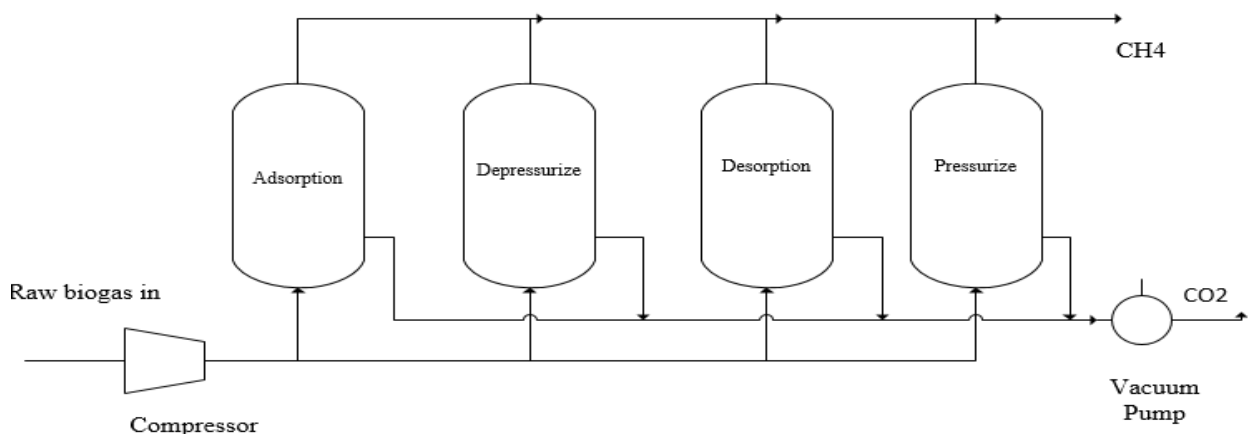


Figure 1-5 Pressure swing adsorption

1.3.4 Membrane separation

The Membrane separation depends on the permeability properties of membranes for different gases. There are two basic setups available in membrane systems, they are gas-gas, and gas-liquid separation system. In gas-gas separation system, pressurized biogas (ranges from 20 to 30 bar) is pre-treated to remove H₂S, as it damages the membrane material. The membrane is made of acetate – cellulose. This system upgrades 92% methane in one step. In the gas-liquid absorption system, gaseous stream and liquid stream flows counter-currently which is separated by a microporous hydrophobic membrane. The molecules from the gaseous stream are absorbed by the liquid stream based on the permeability of various gas molecules. Generally, amine solution is used in the liquid stream. This system can purify 96% methane in one step. It costs \$ 0.15/Nm³. The advantages of membrane system are a simple operation, high reliability and the capacity of small gas flow treatment. The major disadvantages are low membrane selectivity and multiple steps required to reach high purity[16].

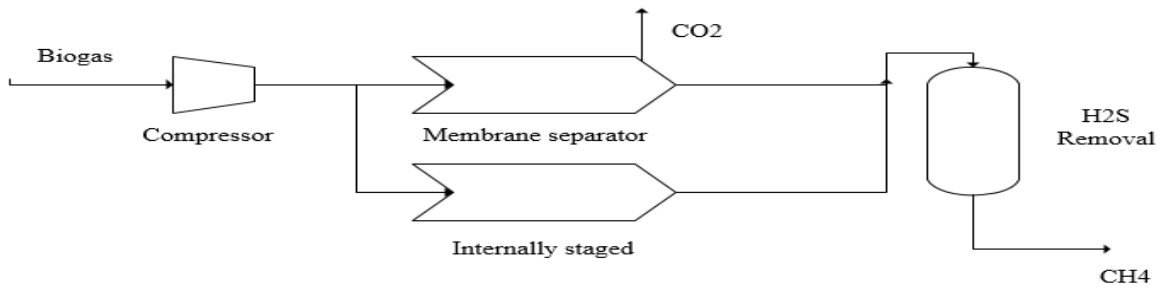


Figure 1-6 Membrane separation

1.3.5 Cryogenic separation

The Cryogenic separation is based on the phase change property of the matter. This process performs at high pressures (40 bars) and low temperatures (-100°C). A series of compressors and heat exchangers are used to maintain desublimation temperature of CO_2 . Once it reaches the required pressure and temperature the raw biogas is sent into the distillation column to separate CO_2 [15]. The main advantages of cryogenic separation are the high purity of biomethane (99% CH_4) and low energy required to get liquid biomethane (LBM). The disadvantages are the need of expensive investment and require high maintenance [16]. The typical cost of a cryogenic method to purify raw biogas is $\$0.54/\text{Nm}^3$.

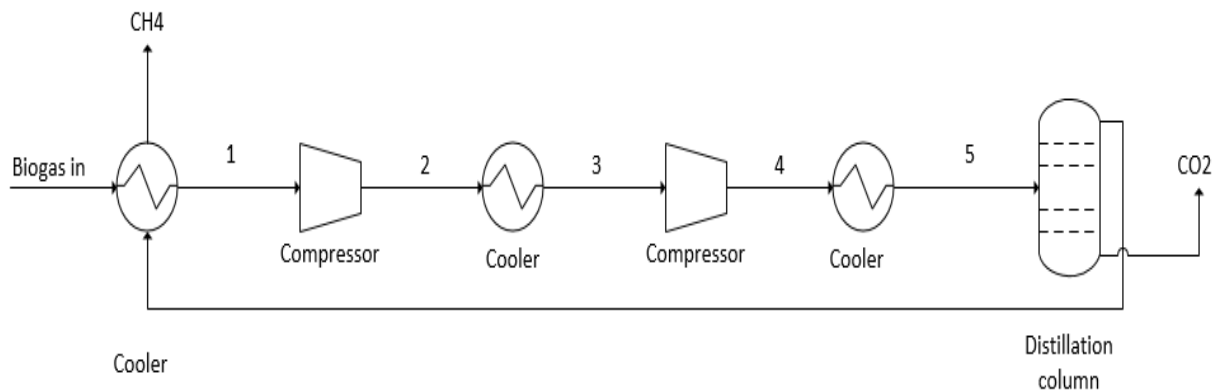


Figure 1-7 Cryogenic separation

The above discussed purification technologies are mostly used in industrial and farm-scale biogas plants. The selection of purification technology depends on energy demand (kWh/m³ biomethane), purification cost (\$/Nm³) and maintenance. Among all the purification technologies the water/polyethylene glycol scrubbing is widely used in commercial plants due to its less purification cost and maintenance.

1.4 Non-commercial/ household biogas plants

The typical capacity of household biogas plants is 1-12 m³, these are mostly installed in developing countries of Asia. The legislation of those countries supports the installation of household biogas plant by providing subsidies. China and India are dominant in house hold biogas production having nearly 80% of total biogas plants. There are currently 40 million plants installed in China, whereas India has 4.5 million plants [17]. China has plans to have 80 million biogas plants by 2020 [2]. India has begun its investments on renewable energy sector by providing subsidies and incentives. The number of household biogas plants in some of the major countries are shown in table 1-3

Table 1-3 Domestic biogas plants in major countries

No.	Country	No. of plants installed
1.	China	40 million
2.	India	4.5 million
3.	Nepal	225,000
4.	Vietnam	150,000
5.	Bangladesh	34,484
6.	Srilanka	6,000

There are currently more than 55 million small-scale household units operating throughout the world. The total biogas which is produced from these household units is exclusively used for cooking and lighting. At some instance, small combustion engines are used at the owner's or producer's house, due to the lack of commercial technology to store and transport excess biogas to the market. There is a need to develop a commercial purification and storage technology to address this problem. The successful development of portable commercial technology has a capacity to increase the economy of people who live in rural areas of developed, developing and underdeveloped countries. It can create self-employment and make people more energy independent by decentralized energy generation.

1.5 Thesis objective

The objective of this thesis is to identify, design, simulate the portable biogas purification and storage system to commercialize the small-scale biogas production. The proposed system is to design for the people who live in rural areas of underdeveloped and developing countries where no vehicle or other transportation is always available for use. The intended use of this system is for an operator to travel to biogas producers in very rural areas of a country and purchase it, then purify and store it in a tank at each biogas digester location. This imposes an important constraint on the system design that this system must be portable by one person, allowing him to travel. The weight should be the main criteria of the system design; all the components are designed in such way that the total weight of the system should not exceed 15 kg (approximate weight a normal person can carry in his/her backpack).

2 LITERATURE REVIEW

In the previous chapter, the importance of biogas in non-conventional energy resources, production, and commercial purification technologies are discussed. This chapter reviews some of the literature on portable/small biogas purification and storage system.

In 2006, Virendra K. Vijay et al., [18] developed a purification system to remove CO₂ from raw biogas of 40% CO₂ using water scrubbing method. This system comprises of single stage compressor, scrubbing column (150mm diameter and 3500mm length), water supply system, gas supply system, three-stage high-pressure compressor, and a storage cylinder. This experimental study is conducted on various flow rates of pressurized (at 1.0 MPa) water and gas ranges 1.8 – 2.0 m³/hr and 1.0 – 3.0 m³/hr respectively. This study concluded that the absorption of CO₂ in water depends on the flow rates of gas and water, the optimum 98.62 % removal of CO₂ was achieved at gas and water flow rates of 1.5 m³/hr and 1.8 m³/hr respectively.

In 2017, Aphichat Srichat et al., [19] designed a biogas purification system using chemical scrubbing method. Their focus was to study the influence of biogas flow rate, chemical solution flow rate, type of solutions and the concentration of various solutions on CH₄ enrichment. They used calcium hydroxide 0.1 mol, calcium hydroxide 0.2 mol, Mono Ethanol Amine (MEA) 0.1 mol and Mono Ethanol Amine (MEA) 0.2 mol. The biogas flow rates used in the experiment were 0.3 m³/hr, 0.6 m³/hr, and 0.9 m³/hr whereas the solution flow rates were 0.6 m³/hr, 1.2 m³/hr, 1.8 m³/hr. The test was conducted on the raw biogas of initial composition 51% methane and 39.36% carbon dioxide. The highest methane enrichment of 81.1% and 89.3% was observed with calcium hydroxide with a concentration of 0.1 and 0.2 mol at biogas and calcium hydroxide solutions flow rates of 0.3 m³/hr, 1.8 m³/hr respectively. From their experimental observations, they concluded that the greater degree of absorption is achieved with higher solution flow rate and lower biogas flow rates.

In 2017, E. Akila et al., [20] used the Pressure Swing Adsorption method for the enrichment of CH₄ in biogas. The main objective of this study is to evaluate the suitability of coconut shell derived granular activated carbon as an adsorbent to remove CO₂ at various inlet gas pressures (ranging from

0.1 to 0.8 MPa). They have used a lab scale Pressure Swing Adsorption column of 1 m height, 0.3 m diameter with a packing column space of height 0.6 m. Activated carbon layers are placed in packing column space at 0.1 m intervals. They observed that the reduction of CO₂ depends on inlet gas pressure, it increases as it reaches the optimum pressure, after that the CH₄ enrichment goes down. In this case, they have used raw biogas of 47% CO₂ and 51 % CH₄, the maximum 93.9% CH₄ content was observed at an optimum 8 bar pressure.

In 2017, Veronika Vrbova et al., [21] designed a system using a membrane separation method. This process depends on the permeability of gases in membrane materials. In this work, they used a polyimide fiber membrane, which has the permeability of 0.25, 10.7 of CH₄ and CO₂ respectively. The experiments were conducted for series and parallel connected membrane module of retentate flow 7 m³/hr. The authors concluded that the parallel connection was the most effective membrane module setup with >96% methane content whereas the series connection was around 94%.

In 2014, Abhulhassan Ali et al., [22] proposed a separation process to separate CO₂ from CH₄ using the cryogenic method. This system is based on the difference in freezing or desublimation properties of individual gases in the mixture. At an atmospheric pressure, CO₂ freezes at 194.5 K (-78.5 °C) whereas CH₄ freezes at 90.5 K (-182.5 °C). The authors designed countercurrent switched cryogenic packed beds to maintain the desublimation temperature of CO₂. The separation process involves in 3 stages, namely, packed bed surface cooling, CO₂ capture, and recovery. They studied the influence of various parameters like the flow configurations, flow rates, feed composition, cryogenic bed temperature distribution and bed saturation time on CO₂ separation. They concluded that the lower CO₂ concentration of the feed decreases the desublimation temperature, the desublimation temperature of CO₂ at 13% and 100% of constant feed flow rate of 0.3 m³/hr were identified as 169 K (-104 °C) and 190 K (-83 °C) respectively.

After detailed observation and analysis of literature on available purification technologies, it can be concluded that absorption purification methods (water/polyethylene glycol scrubbing and chemical absorption) need regeneration. The proposed system should be portable it can't afford regeneration. Pressure swing adsorption (PSA) needs high maintenance and it required a highly skilled operator.

The proposed system is to design for the people who live in rural areas with minimal or no skilled operator. Membrane system almost works at atmospheric pressure and fouling affects its robustness.

Cryogenic method meets some of the requirements of portable biogas purification system. This process doesn't need any regeneration because it doesn't involve in any scrubbing (physical or chemical). The only drawback of the system is the high energy consumption, because of its requirement to maintain desublimation temperature of CO₂ 194.5 K (-78.5 °C). This requirement forces to have efficient heat exchangers or condensers in the system, perhaps this increases the complexity of the system. The proposed system is decided to use the condensation of CO₂ instead of desublimation. The condensation of CO₂ depends on the critical point; it condenses under the critical conditions. The critical pressure and temperature of carbon dioxide and methane are 7.38 MPa (1071 psia), 304.25 K (31.1 °C), 4.59 MPa (667.029 psia), and 190.41K (-82.59 °C) respectively.

3 THERMOPHYSICAL PROPERTIES AND EQUATION OF STATE OF BIOGAS

As discussed in the previous chapter, the modified cryogenic method is decided to be used in the proposed Portable Biogas Purification Process. Thermophysical properties play a vital role in designing the cryogenic purification process as the process is based on the critical properties of gases.

Yaru S.S. et al ., [23] proposed a methodology to determine the properties of a gas mixture, as follows

The mass fraction is,

$$m_a = \frac{m_i}{m} \quad (3.1)$$

Specific gas constant of mixture can be estimated as,

$$R = \sum_{i=1}^n R_i = \sum_{i=1}^n \frac{m_i}{m} \frac{R_o}{M_i} \quad (3.2)$$

Specific heats at constant pressure (C_p), and constant volume (C_v) are [24],

$$C_p = \sum_{i=1}^n \frac{m_i}{m} C_{pi} \quad (3.3)$$

$$C_v = \sum_{i=1}^n \frac{m_i}{m} C_{vi} \quad (3.4)$$

Specific heat ratio (γ) can be written as

$$\gamma = \frac{C_p}{C_v} \quad (3.5)$$

Although, raw biogas has traces of other constituents like Hydrogen sulfide (H₂S), Oxygen (O₂), Nitrogen (N₂) and Carbon monoxide (CO), the focus is on main constituent's methane (CH₄) and Carbon dioxide (CO₂). The properties of pure gases are shown in Table 3-1.

Table 3-1 Properties of pure CO₂ and CH₄

Property	Methane (CH ₄)	Carbon dioxide (CO ₂)
Molecular weight (MW)	16 kg	44 kg
Density at STP (ρ)	$0.668 \frac{kg}{m^3}$	$1.842 \frac{kg}{m^3}$
Critical temperature (T _c)	190.41 K	304.25 K
Critical pressure (P _c)	4.599 MPa	7.384 MPa
Gas constant (R)	$0.518 \frac{kJ}{kg K}$	$0.188 \frac{kJ}{kg K}$

Specific heat at constant pressure and dynamic viscosity are the functions of temperature which can be calculated using empirical constants with less than 5% error. The temperature dependency of the specific heat at constant pressure is determined by,

$$C_p = A + BT + CT^2 + DT^3 \quad (3.6)$$

Where A, B, C, D are empirical constants which are shown in Table 3-2,

Table 3-2 Empirical constants of specific heat at constant pressure

Constant	Methane (CH ₄)	Carbon dioxide (CO ₂)
A	4.750	5.316
B	0.6666×10^{-2}	0.7361×10^{-2}
C	-0.09352×10^{-5}	-0.2581×10^{-5}
D	-0.4510×10^{-9}	0.3059×10^{-9}

The dynamic viscosity is also a function of temperature which is determined by using Sutherland's relation. This relation is based on kinetic theory of ideal gases and an idealized intermolecular-force potential [25]. The Sutherland equation is,

$$\mu = \mu_o \left(\frac{T}{T_o}\right)^{\frac{3}{2}} \frac{T_o + S}{T + S} \quad (3.7)$$

Where μ_o is the reference viscosity at the reference temperature

T_o is the reference temperature

S is the Sutherland temperature

The constants of methane (CH₄) and carbon dioxide (CO₂) are shown below.

Table 3-3 Empirical constants of dynamic viscosity

Constant	Methane (CH ₄)	Carbon dioxide (CO ₂)
μ_o (kg/(m * s))	12.01*10 ⁻⁶	13.70*10 ⁻⁶
T_o (K)	273.15	273.15
S (K)	197.8	222.2

The thermo-physical properties of raw biogas of 50% CO₂ and 50% CH₄ is computed from the individual gas properties are

Table 3-4 Properties of biogas

Property	Biogas (50% CO ₂ and 50% CH ₄)
Molecular weight	30 kg
Density at STP (ρ)	1.529 $\frac{kg}{m^3}$
Gas constant (R)	0.277 $\frac{kJ}{kg K}$

Figure 3-1 to Figure 3-3 shows the specific heat at constant pressure, constant volume and the dynamic viscosity of the biogas of 50% CO₂ and 50% CH₄.

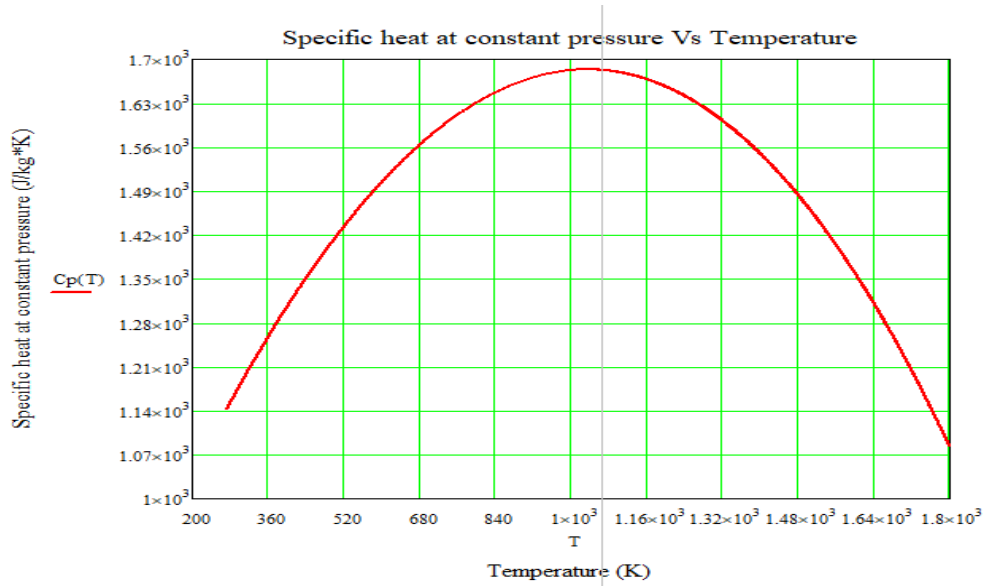


Figure 3-1 Specific heat at constant pressure (J/kg*K) vs temperature

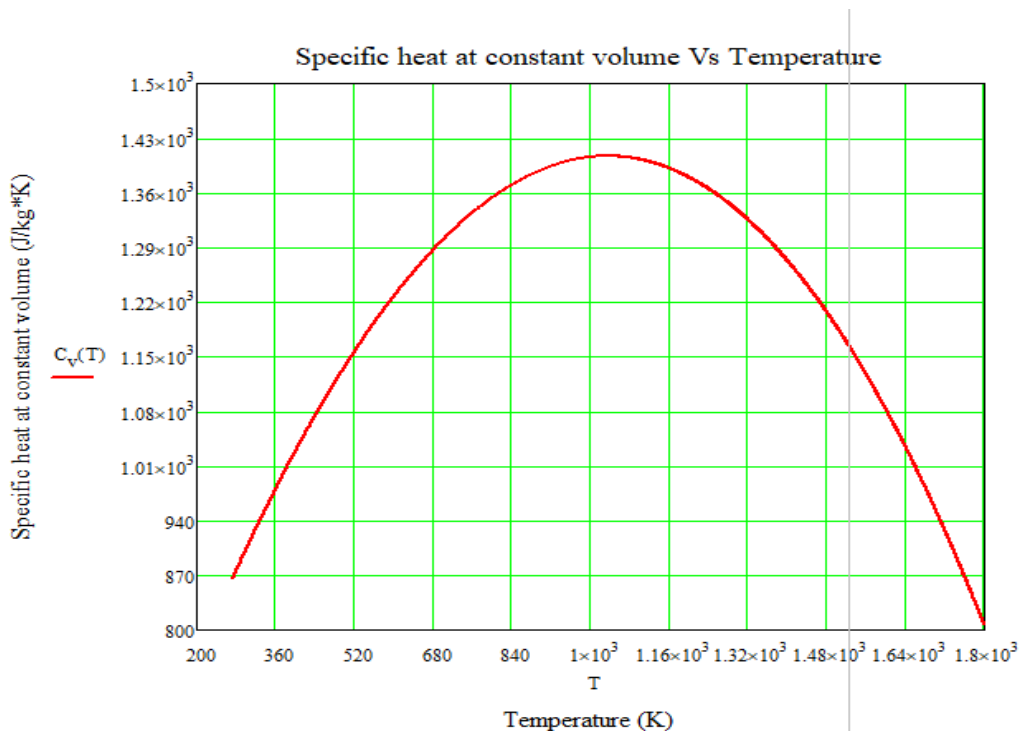


Figure 3-2 Specific heat at constant volume (J/kg*K) vs temperature

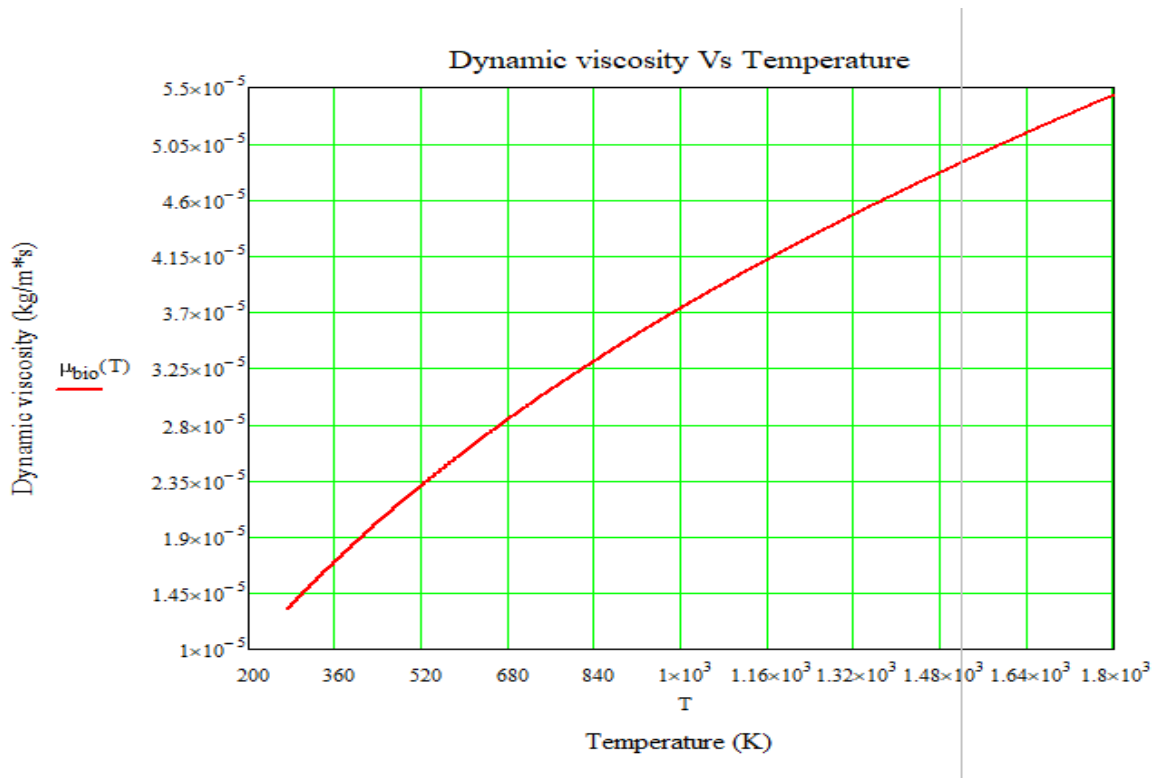


Figure 3-3 Dynamic viscosity (kg/m*s) vs temperature

3.1 Equation of state of biogas

Once the thermo-physical properties of a mixture are determined, the next step is to estimate the critical properties of the mixture. The prediction of Vapor-Liquid equilibrium (VLE) is important to define the critical properties of the proposed raw biogas. There are various Equation of state (EOS) models available for pure components to predict the VLE, some of those shown in Table 3-5.

Table 3-5 Various equation of state (EOS) models

S.No.	Name	Equation of state
1.	Van der Waals (1976)	$P = \frac{RT}{V - b} - \frac{a}{V^2}$
2.	Redlich – Kwong (1949)	$P = \frac{RT}{V - b} - \frac{a}{V(V + b)T^{0.5}}$

3.	Soave – Redlich – Kwong (1972)	$P = \frac{RT}{V - b} - \frac{a(T)}{V(V + b)}$
4.	Peng – Robinson (1976)	$P = \frac{RT}{V - b} - \frac{a(T)}{V(V + b) + b(V - b)}$
5.	Stryjek – Vera – Peng – Robinson (1986)	$P = \frac{RT}{V - b} - \frac{a(\theta, T)}{V(V + b) + b(V - b)}$
6.	Patel – Teja (1982)	$P = \frac{RT}{V - b} - \frac{a(T)}{V(V + b) + c(V - b)}$

It can be observed that a typical equation of state has two terms. The first term represents the intermolecular interactions of repulsive force and the second term represents the attraction force. The equation of state depends on the critical properties of a pure substance and empirical constants.

The Van der Waals equation of state is the simplest and oldest among all the equation of states, this equation relates the pressure (P), temperature (T), specific volume (V) and ideal gas constants (R) by the empirical constants a, b, and m. These constants can be calculated by using critical pressure (P_c), critical temperature (T_c), acentric factor (ω) and an ideal gas constant (R). In 1949, Redlich-Kwong identified that the Van der Waals Equation is rarely accurate to predict the vapor-liquid equilibrium, they modified the Van der Waals equation by making the attraction term temperature dependent. Later, in 1972 Soave replaced the temperature dependent term with a more general temperature dependent term $a(T)$, where,

$$a(T) = 0.4274 \left(\frac{R^2 T_c^2}{P_c} \right) \left(1 + m \left(1 - \left(\frac{T}{T_c} \right)^{0.5} \right) \right)^2$$

$$m = 0.480 + 1.57 \omega - 0.176 \omega^2$$

$$b = 0.08664 \frac{RT_c}{P_c}$$

In 1976, Peng-Robinson redefined the constant $a(T)$ from Soave – Redlich – Kwong equation. The Peng – Robinson equation of state is the most popular and widely used in predicting the vapor-liquid equilibrium [26]. The Peng – Robinson (1976) equation of pure substance can be written as,

$$P = \frac{RT}{V - b} - \frac{a(T)}{V(V + b) + b(V - b)} \quad (3.8)$$

Where,

$$a(T) = 0.45724 \frac{R^2 T_c^2}{P_c} \left(1 + k \left(1 - \left(\frac{T}{T_c}\right)^{0.5}\right)^2\right)$$

$$k = 0.37464 + 1.5422 \omega - 0.26922 \omega^2$$

$$b = 0.07780 \frac{RT_c}{P_c}$$

Figures 3-4 & 3-5 shows the P-V diagram of Pure CO₂ and CH₄ from the Peng-Robinson equation of state. An isotherm of various temperatures is plotted on a P-V diagram to study the phase transformation of the substances. The Figures 3-4 & 3-5 illustrates at the critical pressure the slope of isotherm is zero, the temperature and specific volume at the critical pressure are called as the critical temperature and the critical specific volume. The point is called the critical point, this point distinguishes the phases. At the critical point, the liquid and vapor phases co-exist in equilibrium. The co-existence of vapor-liquid equilibrium is represented by the spinodal curve. The spinodal curve provides the information of fluid at its saturation liquid state (left part of the curve) and at its saturated vapor state (right part of the curve). The critical point makes the boundary between saturated liquid and vapor phase. The region at top right of the spinodal curve is distinguished as the super-heated vapor region, left side as the compressed liquid region, and the region under the spinodal curve is saturated vapor-liquid region. The critical point obtained from the Peng – Robinson equation of state is in good agreement with the tabulated critical point by less than 1% error.

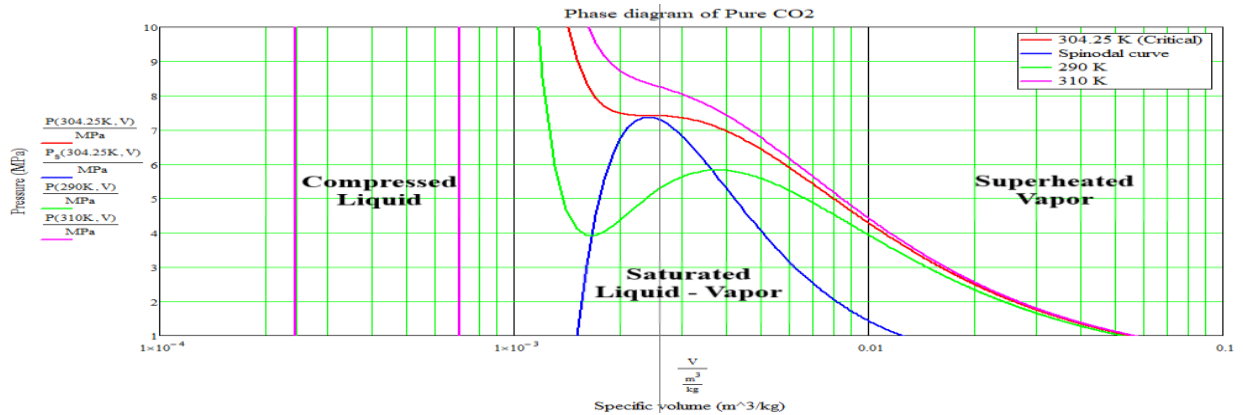


Figure 3-4 P-V diagram of pure CO₂

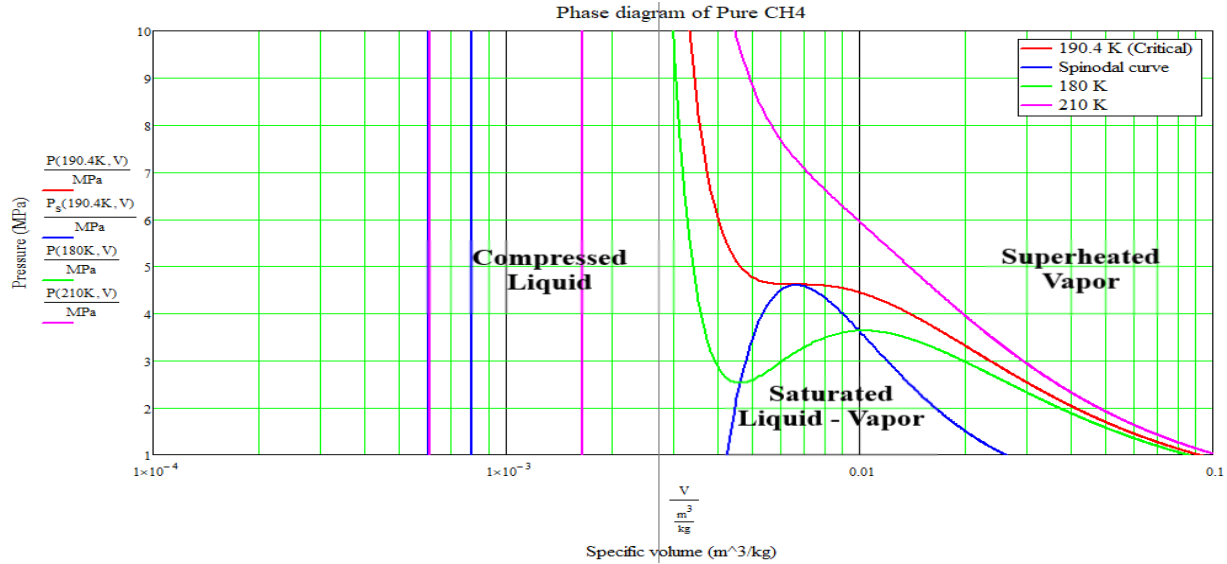


Figure 3-5 P-V diagram of pure CH₄

The information extracted from the above P-V diagrams is useful for the proposed cryogenic purification system, but it doesn't provide enough information to define the thermodynamic states of system as the proposed system involves CO₂ – CH₄ mixture. Gang Xu et al. [27] studied the effect of various critical states of pure gases on its mixture critical point. They concluded that lower critical state of substances lowers the critical state of higher critical state substances. For the proposed system the lower critical state substance is CH₄ at 190.41 K (-82.8 °C) of the critical temperature and 4.599 MPa (665 psia) of the critical pressure. This lower critical state of CH₄ influences the CO₂ critical state from 304.25 K (31.25 °C), 7.384 MPa (1071 psi) to some other point.

An equation of state is developed from the available resources to quantify the influence of CH₄ composition in the critical state of CO₂ – CH₄ binary mixture. Peng – Robinson equation of state of a pure substance can be extended to the binary mixture by selecting the proper mixing rule. Among all the mixing rules, Van der Waals mixing rules are widely used in process simulation. Seif – Eddeen K. Fatten et. al. [26] proposed a methodology to apply Van der Waals mixing rules to Peng-Robinson equation of state. In their work, they proposed a Semi-empirical correlation for binary interaction parameters of CH₄ – CO₂ mixture to minimize the deviation of vapor-liquid equilibrium (VLE) prediction from the experimental predictions. The equations used to develop an equation of state of carbon dioxide in a CO₂-CH₄ binary mixture is as follows.

The Peng – Robinson equation of state of mixture can be written as,

$$P = \frac{R T}{(V - b_m)} - \frac{a_m(T)}{V(V + b_m) + b(V - b_m)} \quad (3.9)$$

The attraction parameter $a_m(T)$ can be expressed as,

$$a_m(T) = \sum_{i=1}^2 \sum_{j=1}^2 x_i x_j (1 - k_{ij}) \sqrt{a_i a_j}$$

The repulsion parameter b_m as,

$$b_m = \sum_{i=1}^2 x_i b_i$$

Binary interaction parameter k_{ij} can be written as,

$$k_{ij} = \frac{1}{2} \frac{b_j}{b_i} \sqrt{\frac{a_i}{a_j}} - \frac{1}{2} \frac{b_i}{b_j} \sqrt{\frac{a_j}{a_i}} + \frac{1}{2} \frac{b_j R T}{\sqrt{a_i a_j}} \frac{\theta_1}{(\frac{T}{T_{c,i}})^{\theta_2}}$$

Where,

x is a mole fraction.

a, and b are the attraction and repulsion terms of pure components.

$\theta_1 = 2.5522$, and $\theta_2 = 0.80726$ are the empirical constantans of the methane/carbon dioxide mixture[26].

Figure 3-6 shows the P -V diagram of 50% CO₂ – 50% CH₄ binary mixture from the modified Peng – Robinson equation of state. It illustrates that the critical state of CO₂ – CH₄ mixture is at 255 K (-18 °C), 4.82 MPa (699.08 psia), and 0.0045 m³/kg. This explains that for a given mixture the vapor-liquid equilibrium of CO₂ co-exists at the critical point.

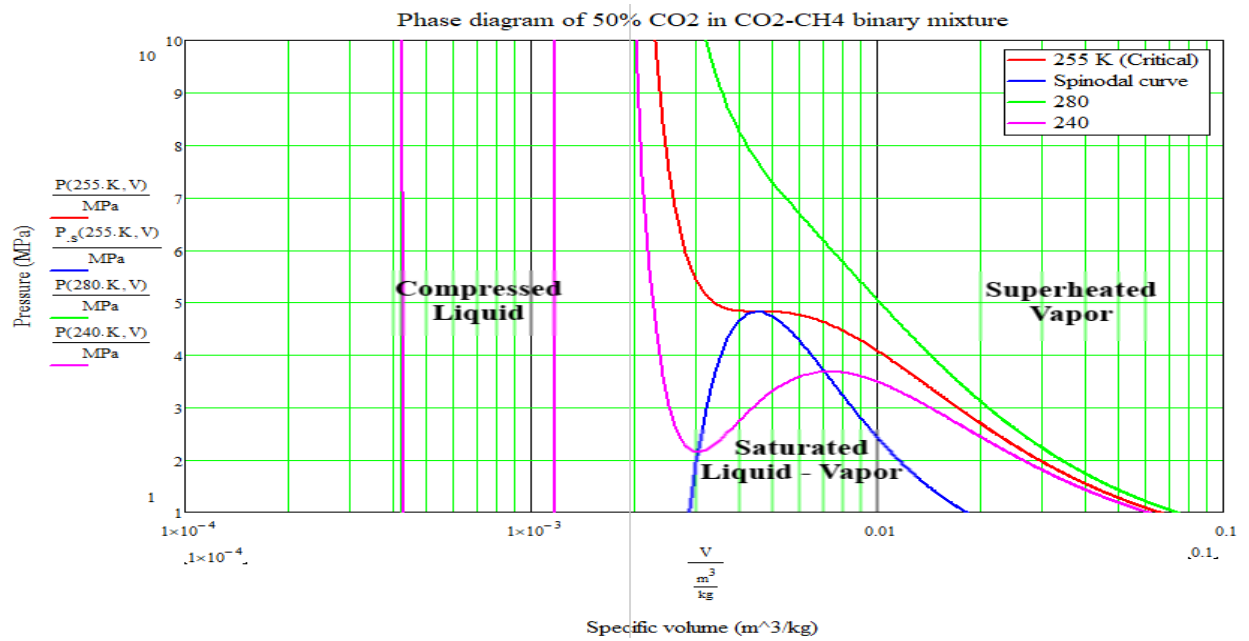


Figure 3-6 P – V diagram of 50% methane and 50% carbon dioxide mixture

It can also be concluded that the composition of CH₄ – CO₂ binary mixture and respective critical states are important for the design. Figures 3-7, 3-8 & 3-9 show the critical temperature, pressure, and specific volume as a function of CO₂ composition extracted from the equation of state of CO₂ – CH₄ binary mixture.

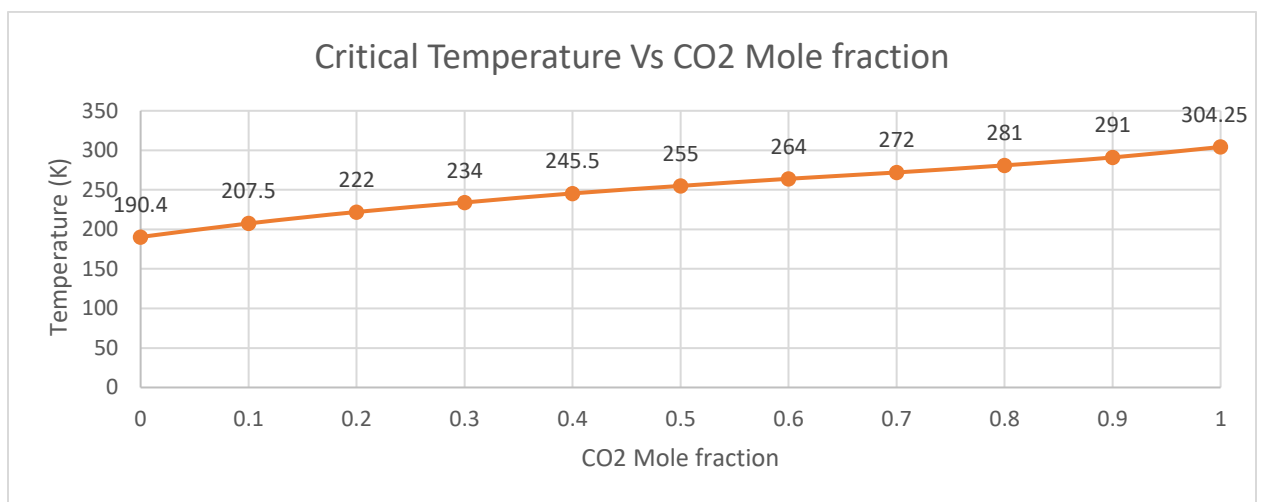


Figure 3-7 Critical temperature vs CO₂ mole fraction

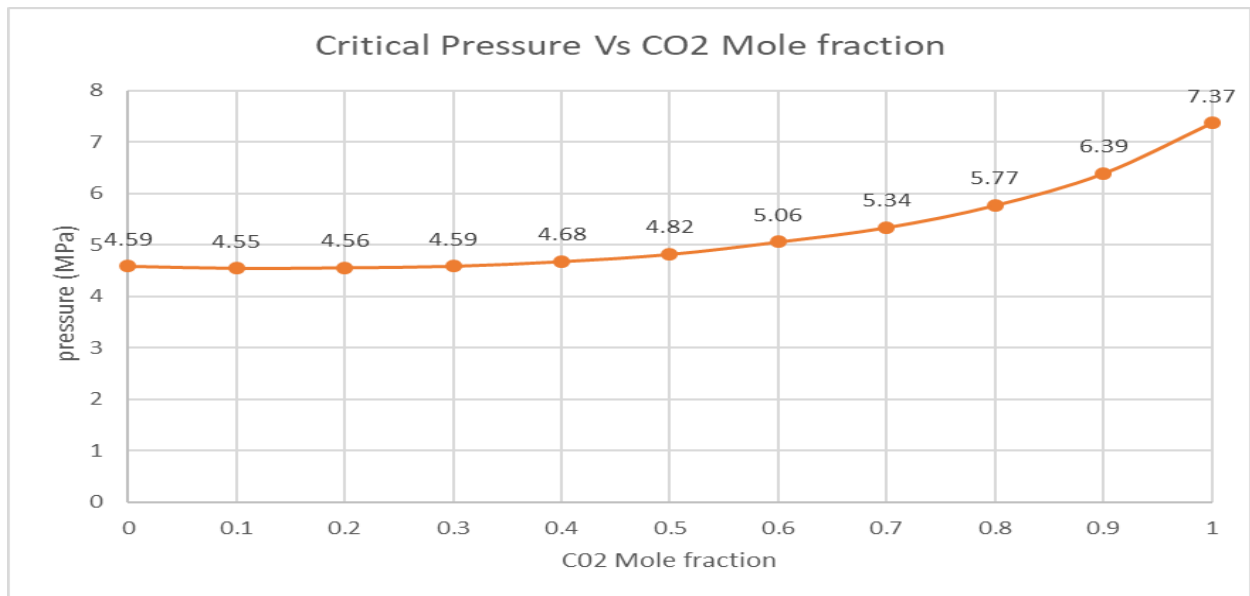


Figure 3-8 Critical pressure vs CO₂ mole fraction

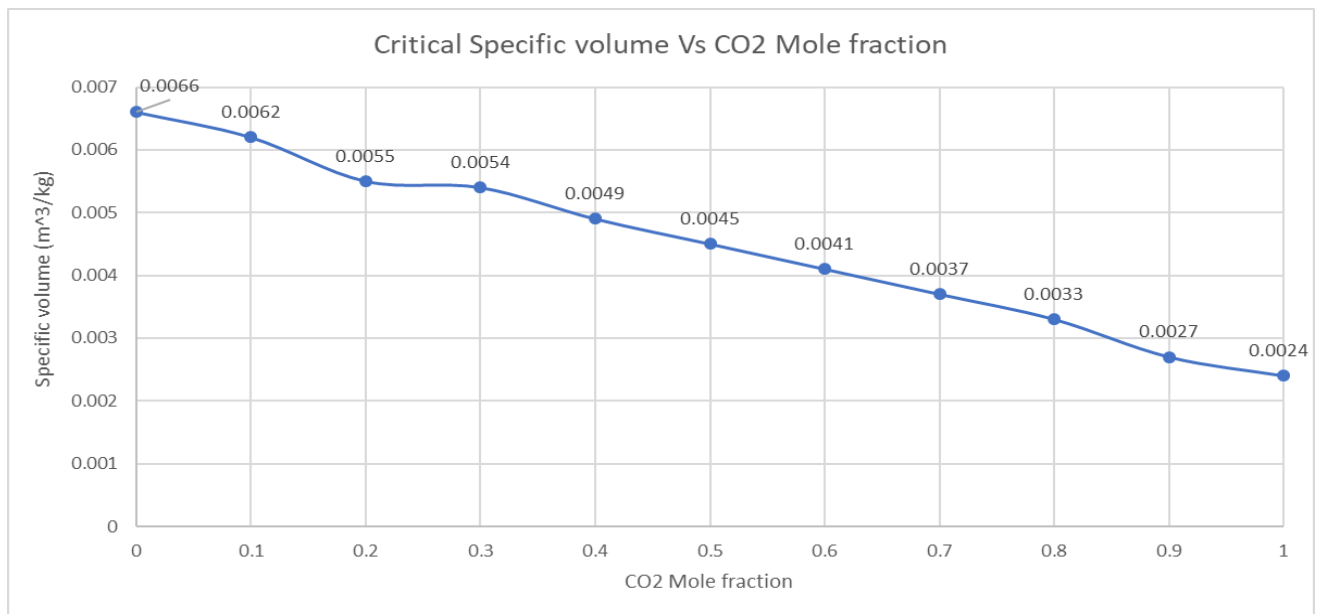


Figure 3-9 Critical specific volume vs CO₂ mole fraction

4 EXPERIMENTAL VALIDATION OF EQUATION OF STATE OF BIOGAS

4.1 Experiment setup

The proposed equation of state successfully quantifies the critical states for variable compositions of $\text{CO}_2 - \text{CH}_4$ binary mixture. An experiment is necessary to validate the equation of state of $\text{CO}_2 - \text{CH}_4$ mixture to use it in proposed purification process design. The typical equation of state defines the relation between the state variables pressure (P), temperature (T), and specific volume (v). These state variables are dependent on each other, for a closed system the variation of pressure and temperature is independent of the specific volume, this simplifies the variables as pressure and temperature. The experiment is designed as a closed system to record the pressure and temperature at constant specific volume. This pressure and temperature data can be used to validate the proposed equation of state by comparing the theoretical and experimental pressure and temperature data. A layout schematic of the experimental setup is shown in Figure 4-1, with a detailed explanation of each component in the following sections.

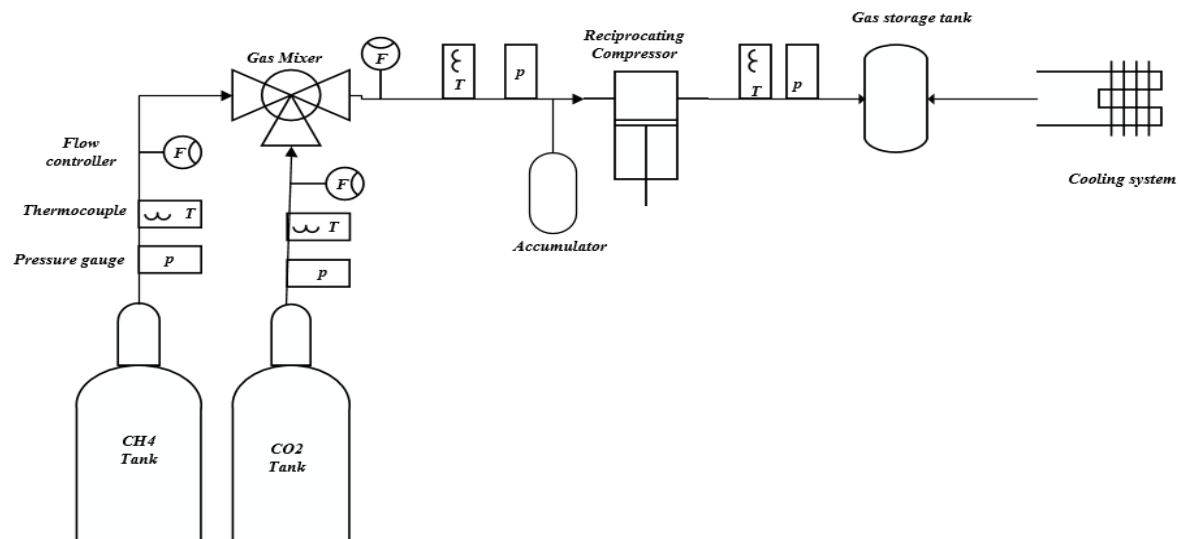


Figure 4-1 Layout schematic of the experiment setup

4.1.1 Gas mixing equipment

The Gas mixing equipment is the primary component of the system it prepares the CO₂-CH₄ binary mixture of specified compositions. It comprises of volumetric flow controllers, pressure gauges, thermocouples, and a gas mixer as shown in figure 4-2. The volumetric flow controllers are used to prepare variable compositions of homogeneous CO₂ – CH₄ binary mixture by controlling the volumetric flow of individual gases based on the given volume fractions. Omega FL4217 – V Acrylic rotameters of maximum flow capacity of 100 SCFH (2.832 m³/hr) is used as a flow controller. The operation of rotameter is based on the variable area principle in which the fluid flow raises a float in a tapered tube. The higher the flow, greater the float height is observed. The flow rate is directly proportional to the height of the float. These are typically designed for air but these can also use for other fluids by using the correction factor. The correction factor is shown below.

$$CF = \sqrt{\frac{(SG)(T_o)(14.7)}{(1.0)(P_o)(530)}} \quad (4.1)$$

Where, SG is the specific gravity of the gas, T_o , P_o are the operating pressure and temperatures then the volumetric and mass flow rate of the incoming gas is calculated from the measured flow rate as.

$$Vdot = Vdot_{measured} CF \quad \quad \quad m\dot{d}ot = \frac{P_o V\dot{d}ot}{R T_o} \quad (4.2)$$



Figure 4-2 Gas mixing equipment

- 1) CH₄ flow controller, 2) CO₂ flow controller, 3) Mixture flow controller, 4) Thermocouple,
- 5) Pressure gauge, 6) Gas mixer.

4.1.2 Accumulator

An accumulator is a flow storage device used to store the potential energy through the compression of the gas. It is placed after the mixing equipment, the objective of this accumulator is to hold/control the gas mixture flow to prevent load on the compressor. Figure 4-3 shows the accumulator used in this system, accumulator outlet is connected to a needle valve (to control/stop the flow) and a gas filter (filter unwanted dust particles).



Figure 4-3 Accumulator

1) Mixture Inlet, 2) Accumulator, 3) Needle valve, 4) Gas filter, 5) Mixture Outlet.

4.1.3 Reciprocating compressor

The reciprocating compressor is an important component of the system. The specifications of this component greatly influence the experiment procedure. Figure 4-4 shows the two-stage reciprocating compressor used in the experiment. This multi-stage compressor takes the gas in and compresses it to the desired outlet set pressure. The pressure regulator is used to set/adjust the discharge pressure. This compressor is also equipped with water cooling for stage two to maintain relatively low outlet temperature.

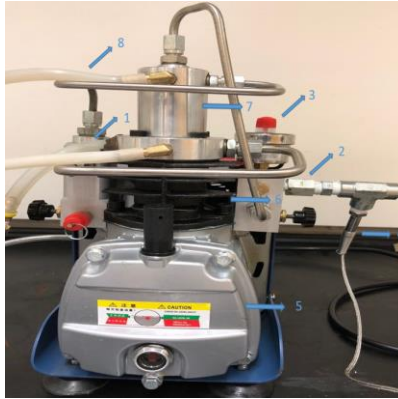


Figure 4-4 Multi-stage reciprocating compressor

- 1) Gas inlet, 2) Gas outlet, 3) Pressure Regulator, 4) Thermocouple, 5) Crankcase, 6) Stage 1 compression chamber, 7) Stage 2 compression chamber, 8) water cooling lines.

The specifications of the compressor are,

Table 4-1 Specifications of commercial compressor

Manufacturer	Young Heng
Working pressure	30 MPa
Voltage	110 V
Motor power	1.8 kW
Net weight	16.2 kg
Maximum flow capacity	50 L/min (3 m ³ /hr)

4.1.4 Liquid – Gas Separator

The objective of Liquid – Gas separator is to separate the liquid from the gas. In this experiment, it is used to store the pressurized gas mixture to record pressure and temperature at constant volume. Figure 4-5 shows the liquid-gas separator used in this experiment, both the liquid and gas outlets were closed

by ball valves to make it a closed system. It also shows the location of pressure gauge and thermocouples.



Figure 4-5 Liquid – Gas Separator

- 1) Mixture inlet, 2) Thermocouple, 3) Pressure gauge, 4) Gas outlet valve, 5) Liquid – Gas separator
6) Liquid outlet valve.

The specifications of Liquid-Gas separator are,

Table 4-2 Specifications of Liquid-Gas separator

Manufacturer	Didion Separator Company
Diameter	3.2 in (0.081 m)
Height	11.5 in (0.292 mm)
Volume	1.516 L ($1.516 \times 10^{-3} \text{ m}^3$)
Tare weight	1.316 kg
Operating pressure	12.4 MPa

4.1.5 Cooling system

The cooling system is the most important and complicated component in the entire experimental setup. The proposed equation of state indicates very low critical temperatures to transform gaseous CO₂ into

liquid CO₂. Figure 3 – 7 shows the influence of CH₄ composition on critical temperature of CO₂. For 50 % methane and 50% carbon dioxide the critical pressure and temperatures are at 4.82 MPa (699.08 psia), 255 K (-18 °C) respectively. The cooling system needs to maintain this low temperature to condensate CO₂. Typical commercial heat exchangers are not adequate to provide such a low temperature. Dry ice was decided to use in the system to provide the required cooling.

4.1.6 Data acquisition system

As discussed in previous sections the experiment is aimed to record the pressure and temperature at constant specific volume. The digital pressure gauge is used to record the pressure variation in the liquid-gas separator. This pressure gauge can measure up to 34.47 MPa with +/- 1 % accuracy. Figure 4-6 (a) shows the digital pressure gauge used in the experiment. Omega TC-K-NPT-G-72 Thermocouples are used to measure the temperature at different locations of the experiment. A thermocouple is a device which produces a temperature – dependent voltage as a result of temperature difference at the junction. The voltage signals are transmitted to the DAQ system, which is then transferred to LabVIEW VI to convert the analog signal to digital code. Figure 4-6 (b) shows the thermocouples used in the experiment. The specific volume of the fluid is the volume occupied by one kilogram of fluid, which can be determined by measuring the total mass of the fluid in the tank. Adam CBK 35a-USB Bench-Scale was used to measure the fluid mass in the tank, this can measure up to 16 kg with 0.5 g readability.



Figure 4-6 Data acquisition equipment

4.2 Experimental procedure

Before starting the system, it is important to close all the valves. Initially, valves of pure gas tanks (CH_4 and CO_2) are opened to reach the proper pressure and flow rate throughout the gas mixing system. Once the pure gases are released into the gas mixing system, the flow meters are manually adjusted to specified flow rates based on the required volume fractions of the binary mixture. The binary mixture from the gas mixing system is then sent to an accumulator to build the inlet pressure for the compressor. This accumulator is operated with the needle valve to control the flow of mixture.

The compressor is set to an operating pressure of the Liquid-Gas separator to store the gas mixture. The compressor is then turned on and left for 4 to 5 seconds to build the suction pressure in the compressor. The valve of an accumulator is opened to allow the gas mixture to the compressor inlet. Once the liquid-gas separator reaches the adjusted pressure, the compressor automatically shuts off. The variation of pressure and temperatures at various locations are recorded. The experiment was performed for Pure CO_2 , 80% CO_2 – 20 % CH_4 mixture, and 50% CO_2 – 50% CH_4 . The inputs required for the gas mixing equipment is shown below.

Table 4-3 Inputs of the experiment

S.no.	X_{CO_2}	X_{CH_4}	$V_{\text{dotCO}_2} (\frac{m^3}{hr})$	$V_{\text{dotCH}_4} (\frac{m^3}{hr})$	$V_{\text{dotmixture}} (\frac{m^3}{hr})$
1.	1	0	1.98	0	1.98
2.	0.8	0.2	1.58	0.39	1.98
3.	0.5	0.5	0.99	0.99	1.98

4.3 Validation of equation of state of CO_2 – CH_4 binary mixture

The validation of the equation of state of CO_2 – CH_4 binary mixture is achieved by comparing the theoretical and experimental saturated vapor pressure and temperature at constant specific volume. As

discussed in the experimental procedure, all mixtures are compressed to 12.4 MPa (operating pressure of liquid –gas separator tank) and then cooled to saturated vapor temperature (obtained from the equation of state of binary mixture) to determine the saturated vapor pressure at constant volume experimentally.

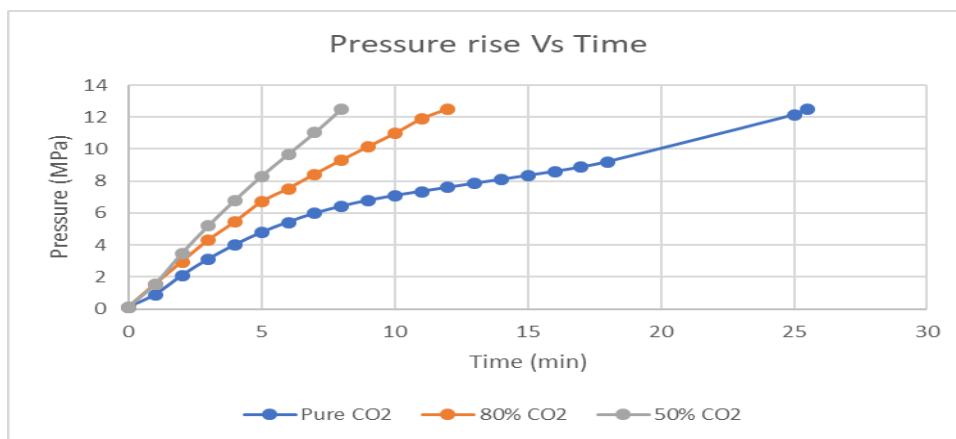


Figure 4-7 Pressure rise vs time

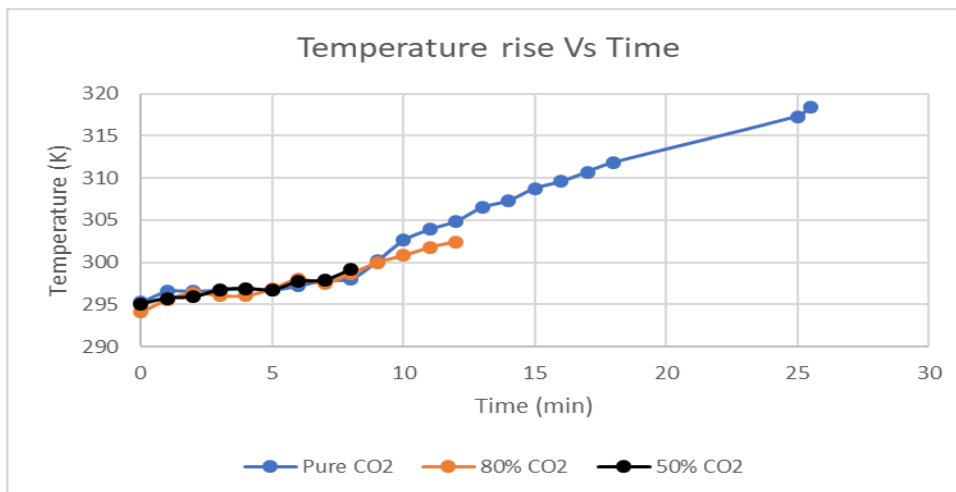


Figure 4-8 Temperature rise vs time

Figures 4-7 & 4-8 show the pressure and temperature rise of various binary mixtures due to the compression. It illustrates that the pressure and temperature are interdependent variables when

pressure increases the temperature also increases, and vice versa. It can be observed that the compression time of the gases varies based on the gas composition, the compression time of pure CO₂, 80% CO₂, and 50% CO₂ are 25.5 min, 12 min, and 8 min, respectively. This compression time indicates that the heavier molecules require more energy for compression. Although all mixtures are stored in the same tank at the same pressure. The mass of fluid stored in the tank varies from mixture to mixture because of the dissimilar molecular weight of the mixture. Once the compression is completed, all the valves of Liquid – Gas Separator tank are closed to make it a closed system. The properties of the fluid mixture after the compression are shown in Table 4-3.

Table 4-4 Properties of fluid after compression

Mixture	m _{mixture} (kg)	m _{CO2} (kg)	m _{ch4} (kg)	$v_{mixture} (\frac{m^3}{kg})$	P (MPa)	T (K)
Pure CO ₂	-----	0.532	-----	2.846×10^{-3}	12.49	318.41
80% CO ₂	0.280	0.257	0.023	5.403×10^{-3}	12.50	302.43
50% CO ₂	0.173	0.127	0.046	8.761×10^{-3}	12.51	299.17

The saturated vapor properties of the mixtures at specified specific volume is obtained from the equation of state of binary mixture is shown in table 4-4.

Table 4-5 Saturated vapor properties of the mixtures at specified specific volume

Mixture	Saturated vapor temperature (K)	Saturated vapor pressure of CO ₂ (MPa)
Pure CO ₂	301	6.91
80% CO ₂	261	3.96
50% CO ₂	224	2.83

Once the saturated vapor temperatures are identified, the next step is to maintain the saturated vapor temperature to record the saturated vapor pressure of mixture experimentally. The experimental saturated vapor pressure is compared to the theoretical saturated vapor pressure to validate the equation of state of binary mixture. The required saturated temperature of pure CO₂ is 301 K; this temperature is greater than the ambient air temperature (295 K). So, the natural convection of ambient air is enough

to dissipate heat from the storage tank. On the other hand, the mixture saturated vapor temperature is less than the ambient temperature, the natural convection alone cannot achieve the required temperature drop therefore an external cooling (provided by dry ice) is used to attain the required low saturated vapor temperatures. Dry ice is the solid form of CO_2 , it sublimates at 194.65 K (-78.5 °C), at atmospheric pressure. When the tank is covered with dry ice the sublimation process cools the tank up to 218 K (-55°C) which essentially cools the gas mixture to required temperature.

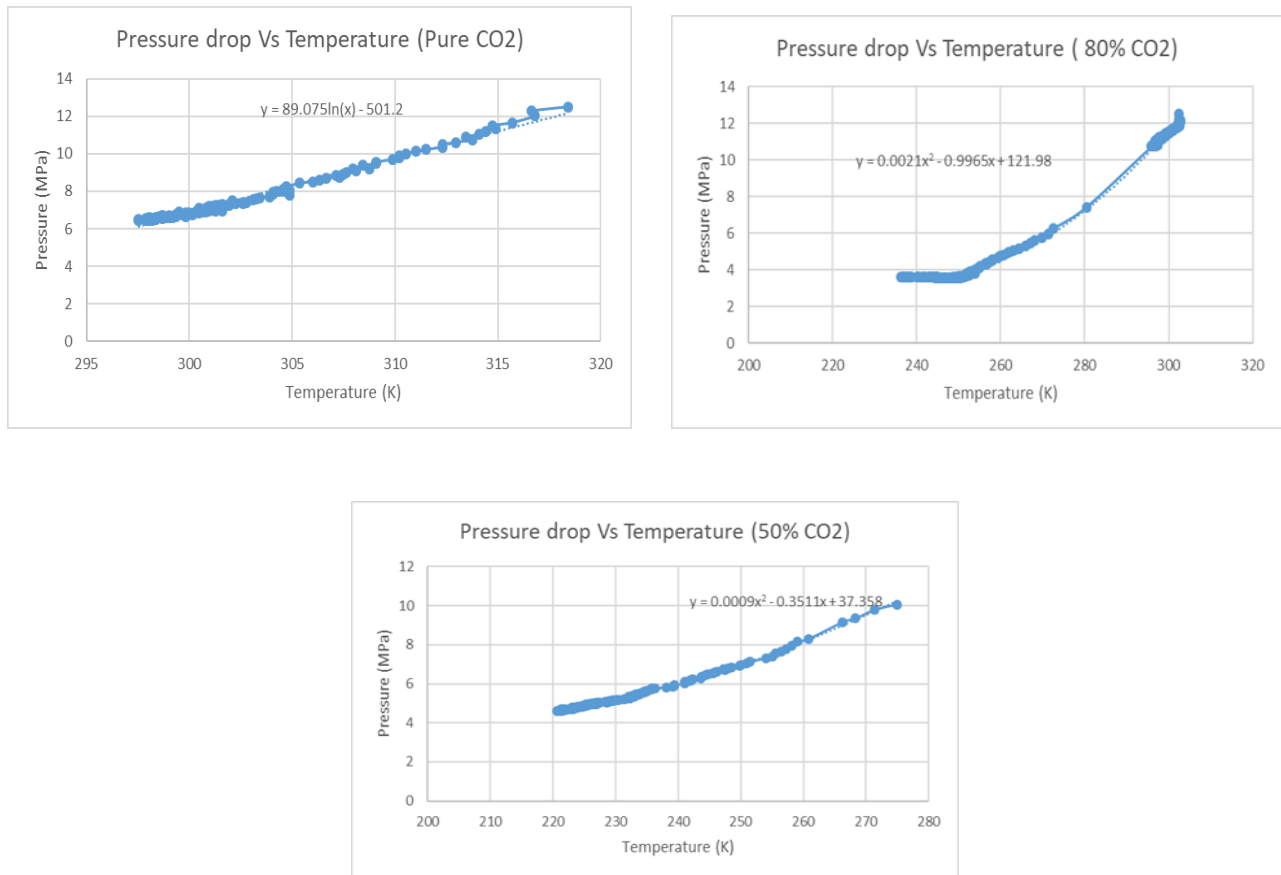


Figure 4-9 Experimental pressure drop vs temperature.

Figure 4-9 shows the pressure drop with respect to the temperature, pressure of a mixture at saturated vapor temperature is compared to theoretical saturated vapor pressure to validate the proposed equation of state. The error percentage of the validation is calculated as.

$$Error \% = \left| \frac{P_{exp} - P_{the}}{P_{exp}} * 100 \right| \quad (4.3)$$

Table 4-5 shows the comparison of experimental saturated vapor pressure with the theoretical vapor pressure at saturated vapor temperature and specific volume.

Table 4-6 Comparison of theoretical and experimental saturated pressures

Mixture	T _{saturated}	P _{saturated} (theoretical)	P _{saturated} (Experimental)	Error %
Pure CO ₂	301	6.91	7.16	3.49
80% CO ₂	261	3.96	4.94	19.83
50% CO ₂	224	2.83	3.87	26.63

The experimental saturated pressure of pure CO₂ at the saturated temperature and specific volume is in good agreement with the theoretical saturated pressure. The error percentage is calculated as 3.49%. The error percentage of 80% CO₂ and 50% CO₂ is determined as 19.83%, 26.63% respectively. This higher error percentage in mixtures is caused mainly due to the lower saturated temperature and the cooling system used for it. As discussed earlier, dry ice was used to maintain the lower temperatures. This dry ice rapidly cools the liquid-gas storage tank to temperatures up to 218 K. This rapid cooling causes errors in data acquisition, which essentially lead to a higher error percentage. Although the higher error percentage is observed, this error is consistent with the saturated temperature. This error can be corrected by incorporating a better cooling system.

5 PURIFICATION PROCESS AND COMPONENTS DESIGN

5.1 Purification process design

The operating principle for the proposed system is to compress and cool the biogas until the carbon dioxide changes its phase from gas to liquid. The liquid CO₂ and the gaseous methane will then be separated and stored in their respective tanks. For the preliminary design, the composition of raw biogas is assumed to be comprised of 50% methane (CH₄), and 50% carbon dioxide (CO₂). From the Figure 5-1, a condensation point is chosen in the liquid region of 50% CO₂ – 50% CH₄ mixture. The temperature and pressure of chosen condensation point are 206 K (-67 °C), 5.65 MPa (819.46 psi) respectively. The chosen point is in the liquid region for all the compositions of CO₂ – CH₄ binary mixture.

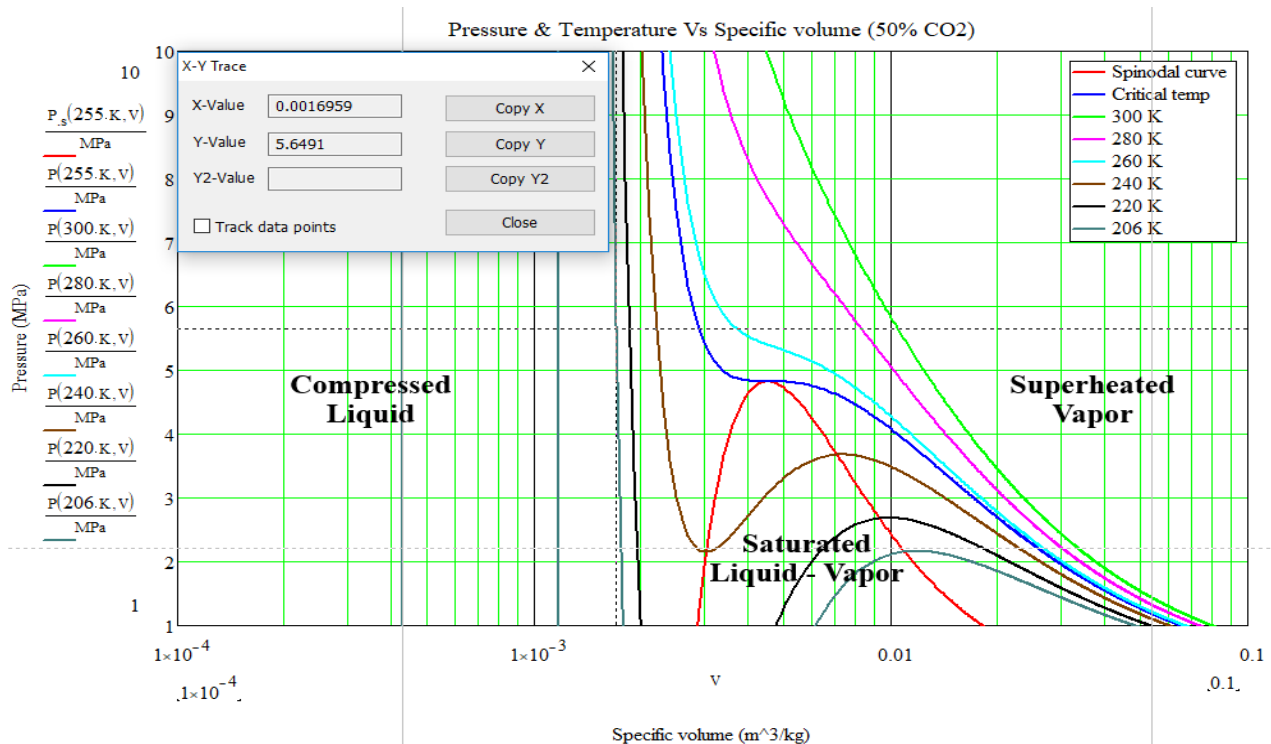


Figure 5-1 Equation of state of CO₂ of CO₂ – CH₄ binary mixture

For this portable purification system, size and weight are of highest priority. The important design parameter which decides the weight of the system is the mass flow rate. All the components have been designed to meet the goal of 4 kg methane processed in about 1 hour which leads to the total mass flow rate of raw biogas to be 15 kilograms per hour. 4 kg of methane is chosen based on the availability and usage of a small propane tank, currently in the market. The identification of the thermodynamic states of the system plays a crucial role in component design. The thermodynamic processes of the proposed system are shown in Figure 5-2.

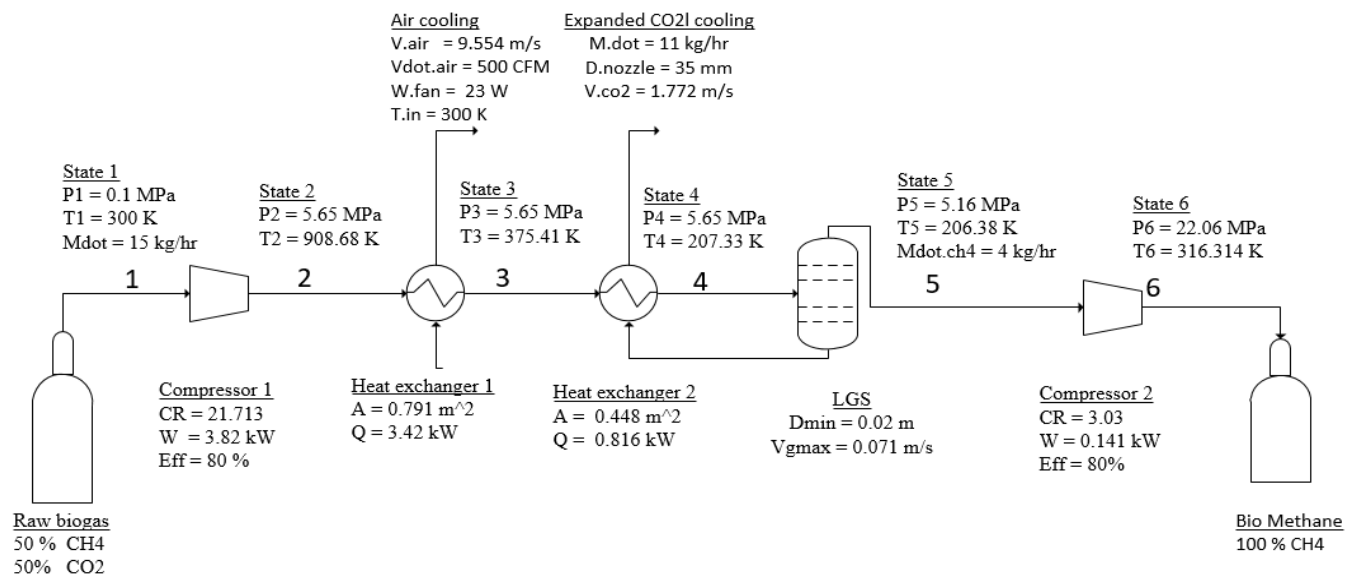


Figure 5-2 Portable biogas purification system design

The Ideal thermodynamic processes required for the purification process are

1- 2 Compression process

2-4 Isobaric Heat rejection process (by air and liquid CO₂ expansion)

4-5 Liquid – Gas separation process (by gravity separation)

5-6 Compression process

5.1.1 Process 1-2 compression

In this process, raw biogas (50% CH₄ and 50% CO₂) of 15 kg/hr enters into the compression system at ambient conditions (0.1 MPa, 300 K), which is then compressed around the liquefaction pressure (5.65 MPa). The following isentropic relations are used to calculate the required compression ratio, power and outlet temperature.

$$\frac{V_1}{V_2} = \left(\frac{P_2}{P_1} \right)^{\frac{1}{\gamma}} \quad (5.1)$$

$$\frac{T_2}{T_1} = \left(\frac{P_2}{P_1} \right)^{\frac{\gamma-1}{\gamma}} \quad (5.2)$$

$$W_{isen} = \frac{\dot{m} \gamma R_{bio} (T_2 - T_1)}{1 - \gamma} \quad (5.3)$$

$$W_{req} = \frac{W_{isen}}{\eta} \quad (5.4)$$

Where γ is the specific heat ratio, which depends on the temperature. All these isentropic values are corrected by applying the compressor efficiency coefficient of 80%. The corrected pressure, temperature and required power of the biogas exit from the compressor are 5.65 MPa (820 psia), 908.68 K (635.68 °C) and 3.82 kW respectively.

5.1.2 Process 2-4 isobaric heat rejection

The objective of this system is to cool the compressed biogas from 908.68 K to liquefaction temperature (206 K). The overall heat dissipation required for this temperature drop is 4.43 kW. Single heat exchanger alone cannot achieve this temperature drop using ambient air as a convective fluid. So, the heat rejection system is retrofitted by an extra heat exchanger. This extra heat exchanger is proposed to use the liquid CO₂ coming out from the liquid-gas separator by expanding it from

liquefaction pressure (5.65) to ambient pressure (1 bar). This expansion leads to the temperature drop from critical temperature (216 K) to 156.91 K, this can be calculated using isentropic relation. In order to define heat dissipation required from the first heat exchanger which is dependent on expanded liquid CO₂ outlet temperature, an iterative program is developed to study and calculate the impact of expanded liquid CO₂ temperature on biogas outlet temperature from heat exchanger 1. After some iterations, the outlet biogas temperature of the heat exchanger 1 is determined as 375.41 K by maintaining the inlet air coolant temperature at 300 K, inlet expanded CO₂ coolant temperature at 156.91 K and the outlet biogas temperature from heat exchanger 2 at 207.33 K (Critical temperature). The major thermodynamic equations used to develop the iterative program are explained below

The required heat dissipation equation from the first law of thermodynamics by neglecting kinetic energy, potential energy, and work done on the system.

$$Q_{dis} = \dot{m} C_p \Delta T_{bio} \quad (5.5)$$

The required heat transfer surface area is calculated by replacing the required heat dissipation by Newton's law of cooling.

$$h_{coolent} A_{required} \Delta T_{coolent} = \dot{m} C_p \Delta T_{bio} \quad (5.6)$$

$$A_{required} = \frac{\dot{m} C_p \Delta T_{bio}}{h_{coolent} \Delta T_{coolent}} \quad (5.7)$$

5.1.3 Process 4-5 liquid – gas separation

After the heat – rejection system, the biogas reaches under the critical properties of carbon dioxide (5.16 MPa, 216 K). At this state, the entire gaseous CO₂ converts to liquid based on the proposed biogas equation of state. The process uses gravity separation method to separate liquid CO₂ from gaseous CH₄. There are two approaches to sizing the gravity separation system which is as follows, The Sounders – Brown approach and the droplet settling theory. Sounders – Brown approach

determines the maximum gas velocity by balancing the forces on liquid droplet (drag force in upward direction exerted by gas and gravitation pull exerted by liquid droplet in the downward direction). The required minimum diameter is calculated based on the maximum gas velocity. The equations are as follow

$$V_{gmax} = \sqrt{\frac{4gD_p}{3C_d} \frac{(\rho_l - \rho_g)}{\rho_g}} \quad (5.8)$$

$$D_{Vmin} = \sqrt{\frac{4 \dot{V}_g}{\pi V_g}} \quad (5.9)$$

The separation process is assumed to be an isothermal and isobaric process. The selection of separator geometry is important for the system. The vessel has a liquid and gas outlet. For an ideal separation, the mass flow rate of the liquid CO₂ which exits from the liquid outlet is 11 kg/hr whereas the mass flow rate of the gaseous methane which exits from the gas outlet is 4 kg/hr. The liquid CO₂ is directed towards the expansion valve to expand it from 5.16 MPa (750 psia) to 0.1 MPa (14.50 psia). This expansion leads the temperature drop from 216 K (57 °C) to 156.91 K (116.09 °C). Which is then used as a coolant for the heat exchanger 2.

5.1.4 Process 5-6 isentropic compression process

The pure methane which exits from the gas outlet is sent to further compression, to store it in CNG quality. Typically, in United States CNG (Compressed natural gas) is stored approximately around 20 MPa pressure. The pure methane is compressed from 5.16 MPa to 22.06 MPa. The final properties of biomethane stored in storage cylinder are 22.06 MPa (3200 psia) and 316.3 K (43.31 °C).

5.1.5 Efficiency of the purification system

The ratio of actual work required for the entire system to lower heating value of biomethane determines the efficiency of the system. Figure 5-2 identifies the required components of the purification system,

those are compressor 1, heat exchanger 1, heat exchanger 2, liquid-gas separator, compressor 2 and light-weight storage tank. The power required by the work consuming devices are 3.82 kW (Compressor 1), 0.141 kW (Compressor 2) and 23 W (Fan). The lower heating value of the biomethane is assumed to be equal to pure methane which is 50×10^6 J/kg. The efficiency of the system is calculated by,

$$\eta = \frac{W_{required\ per\ kg}}{LHV_{CH_4}} 100 \quad (5.10)$$

It can be concluded that the 7% of pure methane's energy is consumed to purify the biogas of 15 kg/hr of 50% methane and 50% carbon dioxide.

The major components of the proposed system are identified as Compressors, Heat Exchangers, Liquid – Gas Separator and Gas Storage Cylinder. The following sections discuss the Selection, Design and Numerical Analysis of individual components based on process requirements.

5.2 Compressor design and finite element analysis

The goal of this section is to design the compressor for the proposed system. The proposed purification system requires two compressors to maintain the required pressure. From figure 3-9, it can be observed that the compressor 1 needs to compress the biogas from ambient pressure (0.101 MPa) to critical pressure of CO₂ (5.16 MPa) whereas, the compressor 2 is used to compress the biomethane (4 kg/hr) from critical pressure of CO₂ to CNG quality (22 MPa). The required compression ratios of compressor 1 and 2 are 21.713, 3.03 respectively. The compressor inlet parameters are shown in Table 5-1.

Table 5-1 Input parameters of compressors

Property	Compressor 1	Compressor 2
Mass flow rate (\dot{m}_{dot})	15 kg/hr (Biogas)	4 kg/hr (Biomethane)
Suction pressure (P_s)	0.101 MPa (ambient)	5.16 MPa
Suction temperature (T_s)	300 K	206.38 K

Required compression ratio (CR)	21.71	3.03
Required discharge pressure (P_d)	5.65 MPa	22.06 MPa
Isentropic discharge temperature (T_d)	908.68 K	316.31 K
Required power (W_{req})	3.82 kW	0.141 kW

An appropriate selection of compressor type is important for the system. An ideal compressor is to flexible to change the inlet gas flow rate (if required), light-weight, cost-effective, and robust. Figure 5-3 summarizes the available compressor types. Although various kinds of compressors are available, each one of it has its own advantages and disadvantages. The thermal compressor is a type of ejector, that uses a high-pressure gas jet to pressurize the incoming gas by mixing. These type of compressors has no moving parts. But, the gas mixing leads to low operating pressure ranges. Dynamic compressors use the centrifugal or axial force to increase the velocity of the fluid and then converts the velocity to pressure by restricting the flow. These compressors are further divided into centrifugal (uses Centrifugal force) and axial (uses axial force) compressors. They can provide continuous flow but, it can only be applicable for low-pressure differences.

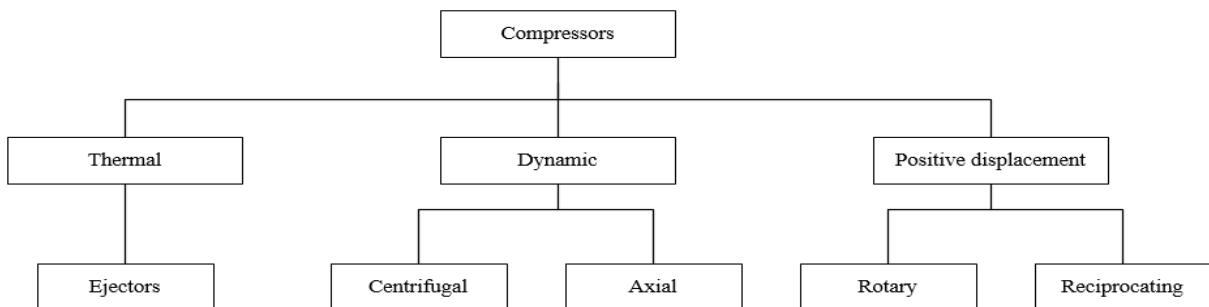


Figure 5-3 Types of compressors

The positive displacement compressors increase the incoming gas pressure by reducing the volume. The two main types of positive displacement compressors are rotary and reciprocating. The rotary compressor uses a set of screws, lobes, or vanes to increase the gas pressure by rotating it [28]. They are simple and inexpensive but are only applicable to low compression ratios. Reciprocating compressors use the reciprocating motion of the piston to compress the gas. These compressors have a wide range of applications in the gas processing industry and can operate at high compression ratios

for lower flow rates. Among all, reciprocating compressor satisfies the requirements (high compression ratio, size, weight, cost) of the proposed system.

In the reciprocating compressor, the rotary motion of the compressor shaft provided by the electric motor is converted to reciprocating motion of the piston by connecting the crankshaft, connecting rod and piston pin to it. The suction and discharge valves are located at the top of the cylinder. Typically, reed valves are used. Figure 5-4 shows the major components of the typical reciprocating compressor, which are identified as Piston, Connecting rod, Crankshaft, Cylinder, Valve plate, Crankcase, and an electric motor.

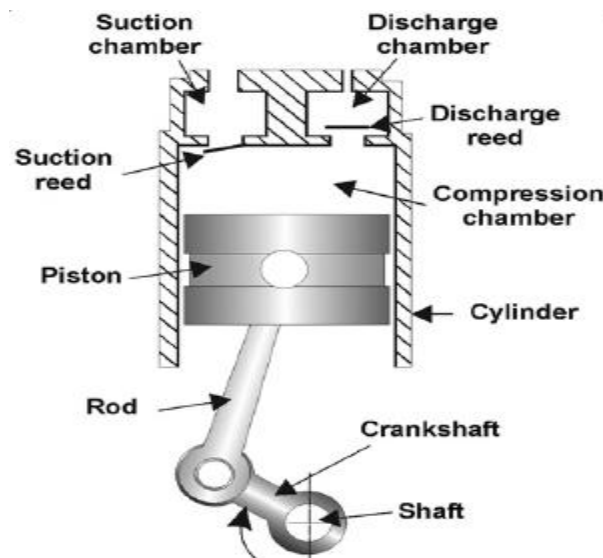


Figure 5-4 Parts of compressor [29]

5.2.1 Design

Figure 5-5 shows a P-V diagram of the reciprocating compressor. At state 4, movement of the piston towards the outer dead center creates a vacuum inside the cylinder. The pressure difference between cylinder and suction chamber opens the suction valve which allows gas flow inside the cylinder. Once it reaches the bottom dead center (state 1), the compression begins as the piston moves towards the

top dead center which closes the suction valve. When the cylinder pressure reaches discharge pressure, the discharge valve opens to eject compressed air at state 2. At state 3, the piston reaches top dead center which closes the discharge valve then, the clearance gas expands as it moves towards the bottom dead center.

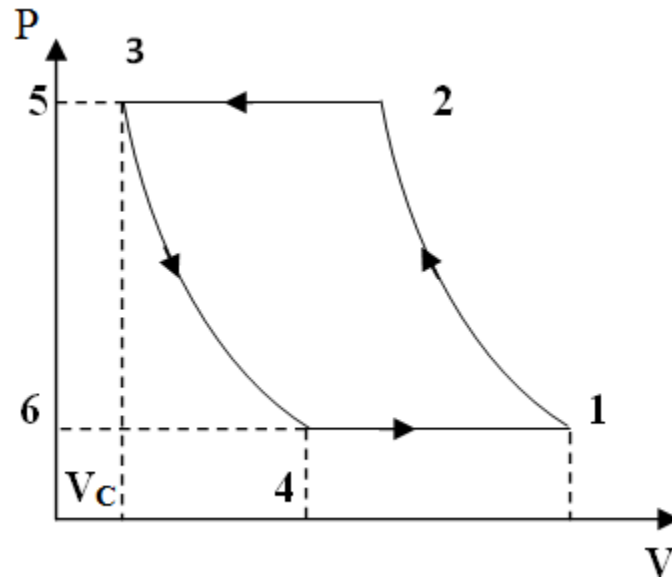


Figure 5-5 Thermodynamic compression cycle

The process of the ideal thermodynamic compression cycle is identified as

Process 4-1: Isobaric gas induction

Process 1-2: Isentropic compression

Process 2-3: Isobaric gas delivery

Process 3-4: Isentropic expansion

The primary step in the design process is to identify the volume at each state of the compression process. This can be achieved by determining the mass of gas per cycle, which is the ratio of the mass flow rate (\dot{m}) to rotations per second (rps).

$$m_{cyc} = \frac{m_{dot}}{rps} \quad (5.11)$$

The volume at state 1 is the total volume required for the mass per cycle at suction pressure and temperature, which can be calculated using the ideal gas equation as

$$V_1 = \frac{R T_s}{P_s} m_{cyc} \quad (5.12)$$

The volume at state 2 is the volume required for the mass per cycle at discharge pressure and temperature which is

$$V_2 = \frac{R T_d}{P_d} m_{cyc} \quad (5.13)$$

The volume at state 3 is called the clearance volume (V_c). Heinz P. Bloch et al., [30] suggested the minimum clearance ratio of a typical reciprocating compressor as 4% to 16 %. The proposed system assumes 4.7% and 16% clearance ratio for compressor 1 and 2 to satisfy the design requirements. The clearance volume is calculated as

$$V_c = V_3 = 0.04 V_1 \text{ or } 0.16 V_1 \quad (5.14)$$

The volume at state 4 is the swept volume (V_s) required for the piston, which can be calculated from total volume (V_1) and volume at state 2 (V_2) as

$$V_s = V_1 - V_2 \quad (5.15)$$

The compression ratio is determined from the swept and clearance volume. This value should be equal to the required compression ratio to validate the clearance ratio assumption

$$CR = \frac{V_s + V_c}{V_c} \quad (5.16)$$

Once the swept volume is determined, the next step is to calculate the bore and stroke required for the compressor. Stroke (S) to Bore (B) ratio plays a vital role in the design. Dennis N. Assanis et al.,[31] recommended the 1.3 Stroke/Bore ratio from their simulation results. The bore is calculated using the cylindrical geometric relationship as

$$B = \sqrt[2]{\frac{4 V_d}{\pi S}} \quad (5.17)$$

The design parameters of the compressors are shown in Table 5-2.

Table 5-2 Design parameters of the compressors

Parameter	Compressor 1	Compressor 2
Angular velocity (ω)	3600 RPM (Assumption)	60 RPM (Assumption)
Mass per cycle (m_{cyc})	$6.94 \times 10^{-5} kg$	$1.11 \times 10^{-3} kg$
Volume at state 1 (V_1)	0.057 L	0.011 L
Volume at state 2 (V_2)	0.003 L	0.0044 L
Volume at state 3 (V_c)	0.0026 L	0.0019 L
Volume at state 4 (V_d)	0.054 L	0.0079 L
Compression ratio (CR)	21.12 (Satisfied)	5 (Satisfied)
Bore (B)	37.48 mm	19.06 mm
Stroke (S)	48.73 mm	24.78 mm

The design methodology of major components (Piston, connecting rod, Crankshaft) is briefly discussed.

5.2.1.1 Piston

The Piston is a reciprocating part of the compressor which compresses the gas by its reciprocating motion. The typical materials used are Cast Iron, Aluminum Alloy, and Cast Steel. Figure 5-6 shows the important parameters required for the piston design.

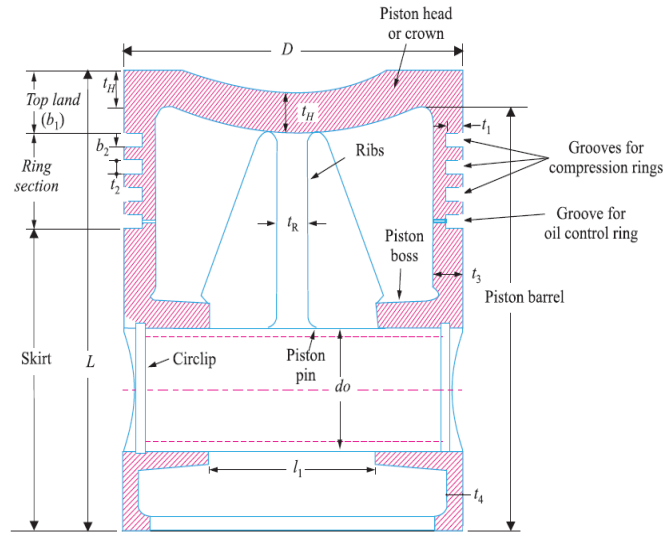


Figure 5-6 Piston parameters [32]

The thickness of the piston head (t_H) is calculated using Grashoff's formula based on discharge pressure (P_d) and permissible yield strength of the material (σ_t) as

$$t_H = B \sqrt{\frac{3 P_d B^2}{16 \sigma_t}} \quad (5.18)$$

The piston rings are used to maintain the seal between piston and cylinder bore. There are two types of piston rings such as compression (or pressure rings) and oil rings. The compression ring prevents the fluid leakage to the crankcase whereas, the oil ring prevents oil leakage to the cylinder. Three piston rings are chosen for the proposed design. The radial thickness (t_1) of a piston is mainly depending on the gas pressure on cylinder walls (P_w) which are typically assumed as 0.025 MPa to 0.042 MPa.

$$t_1 = B \sqrt{\frac{3 P_w}{\sigma_t}} \quad (5.19)$$

The minimal axial thickness is calculated, based on the number of rings (n_r)

$$t_2 = \frac{B}{10 n_r} \quad (5.20)$$

The width of top land (b_1) from piston head thickness is calculated as

$$b_1 = 1.2 t_H \quad (5.21)$$

The width of other land (b_2) is determined from the axial thickness as

$$b_2 = 0.75 t_2 \quad (5.22)$$

The piston barrel is a cylindrical portion of the piston. The minimum piston barrel thickness at an open end (t_3) determined from the relation [32].

$$t_3 = 0.03 B + t_H \quad (5.23)$$

The minimum piston barrel thickness (t_4) at the open end is

$$t_4 = 0.35 t_3 \quad (5.24)$$

The section of the piston under the grooves is called as piston skirt, length of the piston skirt (L_s) is

$$L_s = 0.65 B \quad (5.25)$$

The total length of the piston (L) is

$$L = L_s + 2 b_2 + 3 t_2 + b_1 \quad (5.26)$$

Once the important design parameters of the piston are determined, the next step is to design piston pin or gudgeon pin. It is a hollow cylinder (tapered inside), which is used to connect the piston to connecting rod. The piston pin is to be designed for maximum load exerted by compressed gas which is

$$F_g = \frac{\pi}{4} B^2 P_d \quad (5.27)$$

The load due to bearing pressure is

$$F_b = P_b d_o l_1 \quad (5.28)$$

The outside diameter (d_o) of the pin is determined by equating the load due to bearing pressure and the load due to maximum gas pressure as

$$d_o = \frac{F_g}{P_b l_1} \quad (5.29)$$

The inside diameter of the pin (d_i) from the outside diameter is

$$d_i = 0.6 d_o \quad (5.30)$$

The center of the piston pin should be from 0.02 B to 0.04 B above the center of the skirt. The length of the piston pin (l_1) in the connecting rod bush is taken as 0.45 B.

The inputs required for the piston 1 and piston 2 design are tabulated in Table 5-3.

Table 5-3 Input parameters for piston design

Input parameter	Piston1	Piston 2
Material	Aluminum alloy	Steel alloy

Factor of safety	2.25	2.25
Tensile yield strength	275 MPa	620 MPa
Gas pressure on cylinder wall	0.042 MPa (Assumption)	0.042 MPa (Assumption)
Bearing material	Bronze	Steel
Allowing Bearing pressure	50 MPa	100 MPa

The final design dimensions of the pistons are obtained and are tabulated in Table 5-4.

Table 5-4 Final dimensions for the piston design

Final design Parameter	Piston 1	Piston 2
Piston head thickness (t_H)	3.49 mm	2.33 mm
Radial thickness (t_1)	1.2 mm	0.40 mm
Number of rings	3	3
Axial thickness (t_2)	1.25 mm	0.63 mm
Width of the top land (b_1)	4.19 mm	2.80 mm
Width of other ring lands (b_2)	0.937 mm	0.47 mm
Top end piston barrel thickness (t_3)	4.616 mm	2.90 mm
Open end piston barrel thickness (t_4)	1.616 mm	1.01 mm
Piston skirt length (L_s)	24.368 mm	12.39 mm
Total length of the piston (L_p)	34.181 mm	18.056 mm
Outside diameter of the piston pin (d_o)	7.39 mm	7.342 mm
Inside diameter of the piston pin (d_i)	4.43 mm	4.40 mm
Length of the piston pin in the bush (l_1)	16.87 mm	8.58 mm
Weight (kg)	0.046	0.015

CAD modelling of piston 1 and 2 in shown in figure 5-7 and 5-8.

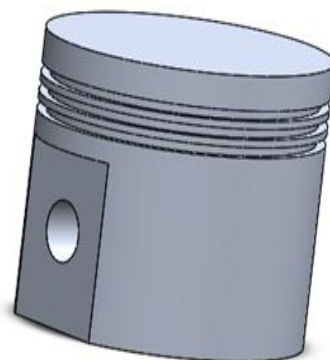
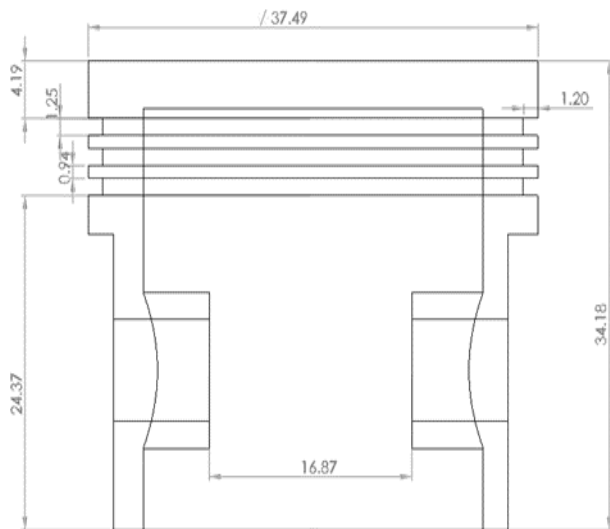


Figure 5-7 Piston-1 2D and 3D models.

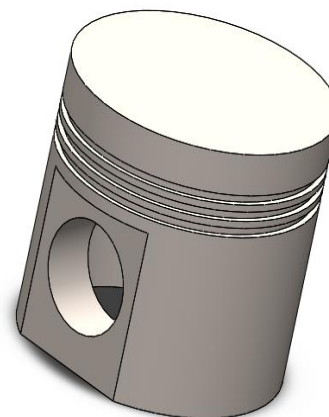
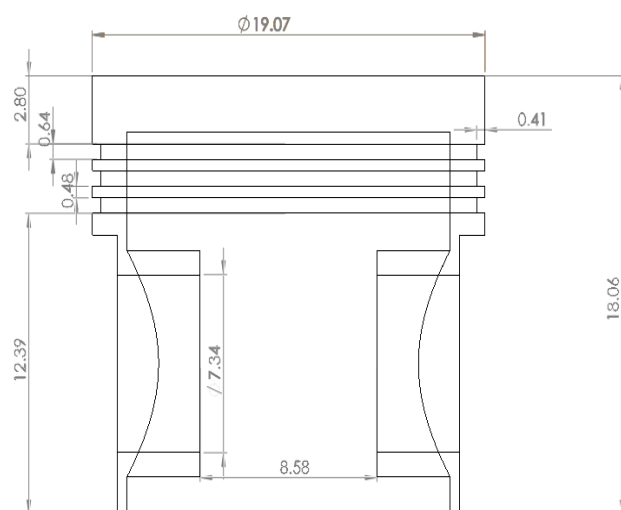


Figure 5-8 Piston-2 2D and 3D models.

5.2.1.2 Connecting rod

The connecting rod connects the piston to the crankshaft by piston pin (or gudgeon pin) and crank pin. This transmits the rotary motion of crankshaft to reciprocating motion of a piston. It is a long shank connected between a small end to the big end. The typical cross-section used in the reciprocating compressor is the I-section. Figure 5-9 shows the cross-section of the connecting rod.

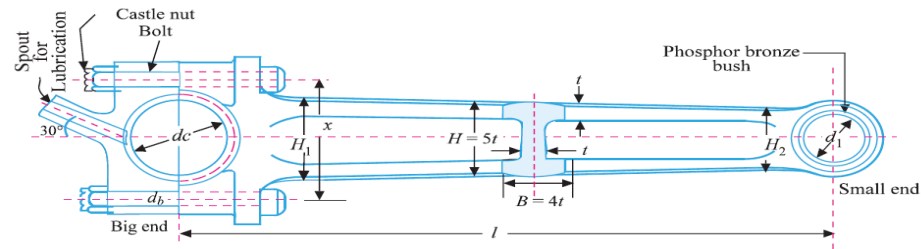


Figure 5-9 Cross- section of a connecting rod [32]

The alternating direct compressive and tensile forces act on the connecting rod. Leela Krishna et al., [33] identified that the connecting rod should be four times stronger in buckling about y-axis than about x-axis, as the compressive force dominates tensile force. The I-section chosen for the design is as follows.

The thickness of the web and flange section is 't'

Width (B) of the section

$$B = 4 t$$

Height (H) of the section

$$H = 5 t$$

Area of the cross-section

$$A = 11 t^2$$

Moment of inertia of the section about X-axis

$$I_{xx} = \frac{419}{12} t^4$$

Moment of inertia of the section about Y-axis

$$I_{yy} = \frac{131}{12} t^4$$

The ratio of x-moment of inertia to y-moment of inertia is 3.2, which is less than suggested moment ratio 4. So, the cross-section selection is valid.

The length of connecting rod (L_c) is calculated from stroke (S) as

$$L_c = 2 S \quad (5.31)$$

The connecting rod is to be designed to withstand the maximum buckling load caused by discharge pressure. Which is calculated from discharge pressure with a safety factor (FS),

$$W_B = \frac{\pi B^2 P_d}{4} FS \quad (5.32)$$

The buckling load can also be expressed using Rankin's formula,

$$W_B = \frac{\sigma_c A}{1 + a \left(\frac{L_c}{k_{xx}}\right)^2} \quad (5.33)$$

Where,

σ_c is compressive yield strength.

A is cross-section area of the section which is $11 t^2$.

L_c is the length of the connecting rod.

'a' is material constant which can be expressed by compressive yield strength and Young's modulus (E) as $\frac{\sigma_c}{\pi^2 E}$.

k_{xx} is the radius of gyration expressed from x-moment of inertia and area of section as $\sqrt{\frac{I_{xx}}{A}}$

The thickness of the section is determined by equating above buckling load equations based on which the other dimensions are calculated. The height of the shank at the small and big end is 0.85 and 1.2 respectively. The inner diameter of the small end should be equal to the outer diameter of the piston pin. The outer diameter of the small end is the sum of inner diameter, bush thickness, and marginal thickness.

The inner diameter of the big end is calculated from crank pin geometry. Crank pin connects the connecting rod to the crankshaft. The design of crank pin is explained later. The inputs required for the connecting rod design are tabulated in Table 5-5.

Table 5-5 Input parameters required for connecting rod design

Input parameters	Connecting rod 1	Connecting rod 2
Material	Aluminum alloy	Steel alloy
Compressive yield strength (σ_c)	275 MPa	723 MPa
Safety factor (SF)	6	6
Modulus of Elasticity (E)	65 GPa	210 GPa
Bush material	Bronze	Steel
Allowable bearing pressure	12.5 MPa	25 MPa
Marginal thickness	2 mm	2 mm

The final design parameters of the connecting rod are tabulated in Table 5-6.

Table 5-6 Final design parameters of connecting rods

Final design parameters	Connecting rod 1	Connecting rod 2
Length of the connecting rod (L)	97.47 mm	49.57 mm
Thickness of the section (t)	3.68 mm	2.23 mm
Height of the section at big end (H_1)	22.08 mm	13.42 mm
Height of the section at small end (H_2)	15.64 mm	9.511 mm

Inner diameter of the small end (d_{si})	7.39 mm	7.34 mm
Outer diameter of the small end (d_{so})	15.39 mm	9.34 mm
Inner diameter of the big end (d_{bi})	19.59 mm	13.92 mm
Outer diameter of the big end (d_{bo})	29.60 mm	15.99 mm
Weight (kg)	0.062	0.022

CAD modelling of connecting rods 1 and 2 shown in figure 5-10

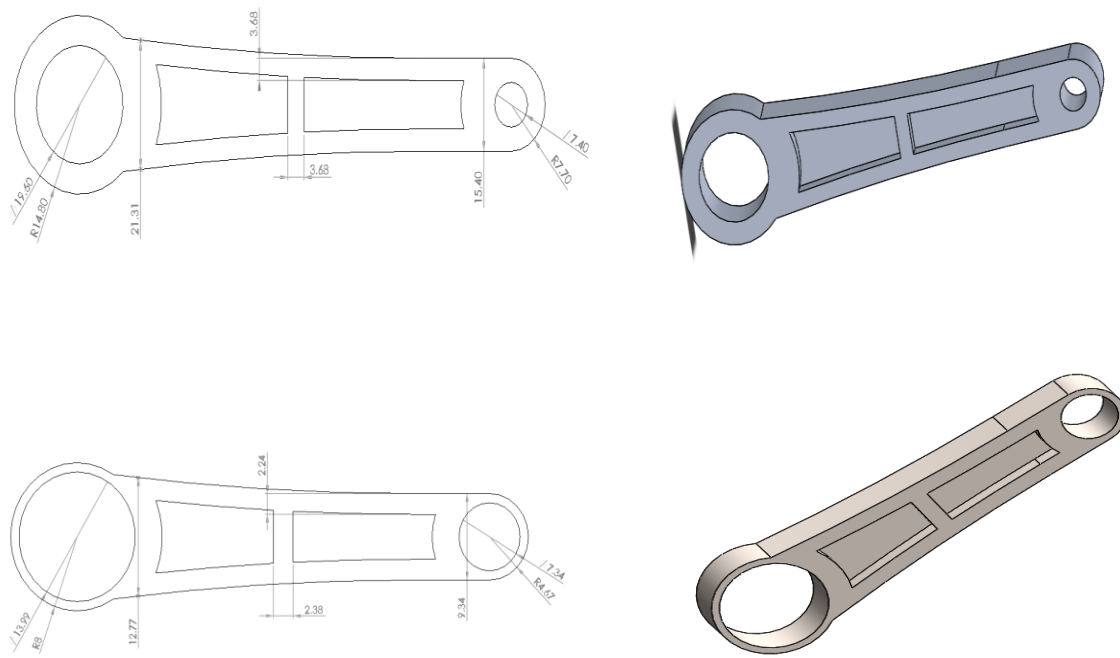


Figure 5-10 2D and 3D models of the connecting rod 1 and 2

5.2.1.3 Crankshaft

Crankshaft converts the rotary motion of an electric motor to reciprocating motion of the piston, by means of connecting rod. It comprises shafts, bearings, crank webs (or arms), and crankpin. There are two types of crankshaft geometries based on the crank pin position. When crankpin is in the center it is called Centre Crankshaft and as Side crankshaft, if it's at the side. The Centre Crankshaft geometry

is used in the proposed design for its stability and proved utilization in small reciprocating compressors.

There are two forces acting on the crankshaft depends on crank position. When the crank is at dead center, piston transmits the maximum force on to crankpin which causes maximum bending stress on the crankshaft. When the crank is at an angle, the twisting stress dominates bending stress. The crankshaft design is based on either condition of the crank. The proposed crankshaft is designed at the crank which is at dead center. Figure 5-11 shows typical crankshaft and forces associated with it.

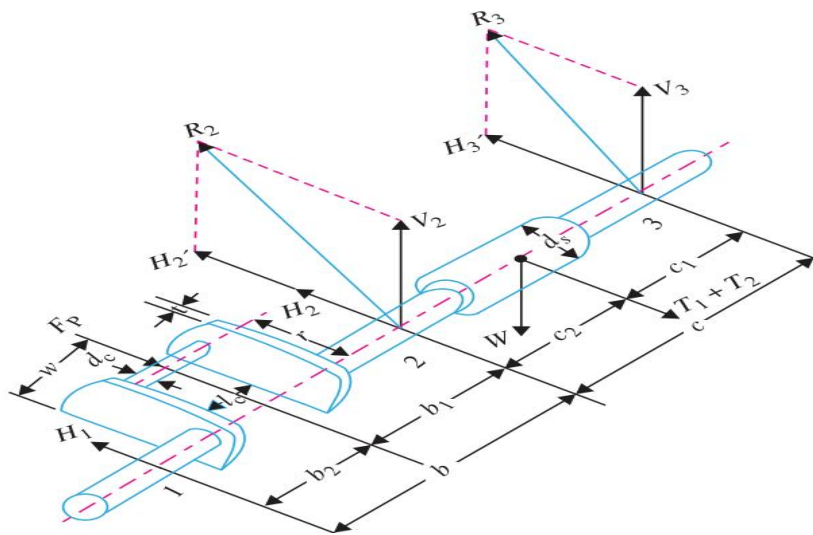


Figure 5-11 crankshaft

The maximum load on piston due to discharged gas pressure is calculated from equation 5.27. When piston load acts on a crank pin in the normal direction, it exerts two horizontal reaction forces on shaft 1 and 2. The load is assumed to be distributed equally along the shaft. The reaction forces can be expressed by the maximum gas load (F_g) and the distance between shaft centers (b).

$$H_1 = \frac{F_g b_1}{b} \quad H_2 = \frac{F_g b_2}{b} \quad (5.34)$$

The crankpin is designed by assuming maximum bending moment at the center of pin, which can be determined by horizontal reaction force (H_1) as,

$$M_c = H_1 b_2 \quad (5.35)$$

The bending moment can also be calculated from maximum allowable bending stress (σ_b),

$$M_c = \frac{\pi}{32} (d_c)^3 \sigma_b \quad (5.36)$$

The required crank diameter is determined by equating (5.35) & (5.36) equations. The crank pin length is obtained by assuming allowable bearing pressure (P_b) as

$$l_c = \frac{F_g}{d_c P_b} \quad (5.37)$$

Crank web thickness (t) and crank web width (w), are calculated using the empirical relations based on bore diameter (B) and crank pin diameter (d_c),

$$\begin{aligned} t &= 0.32 B \\ W &= 1.12 d_c + 12.7 \text{ mm} \end{aligned} \quad (5.38)$$

The required shaft diameter is calculated using the relation based on crank web thickness (t),

$$d_s = \frac{t}{0.6} \quad (5.39)$$

The final dimensions of the crankshafts are tabulated below in Table 5-7.

Table 5-7 Final design of crankshafts

Dimension	Crankshaft 1	Crankshaft 2
Crank pin diameter (d_c)	19.59 mm	13.92 mm
Length of the crank pin (L)	25.47 mm	18.09 mm
Thickness of the crank web (t)	11.99 mm	6.1 mm
Width of the crank web (W)	22.04 mm	15.66 mm
Diameter of the shaft (d_s)	19.99 mm	10.16 mm
Weight (kg)	0.145	0.098

CAD modeling of crankshaft1 and 2 are shown in Figure 5-12.

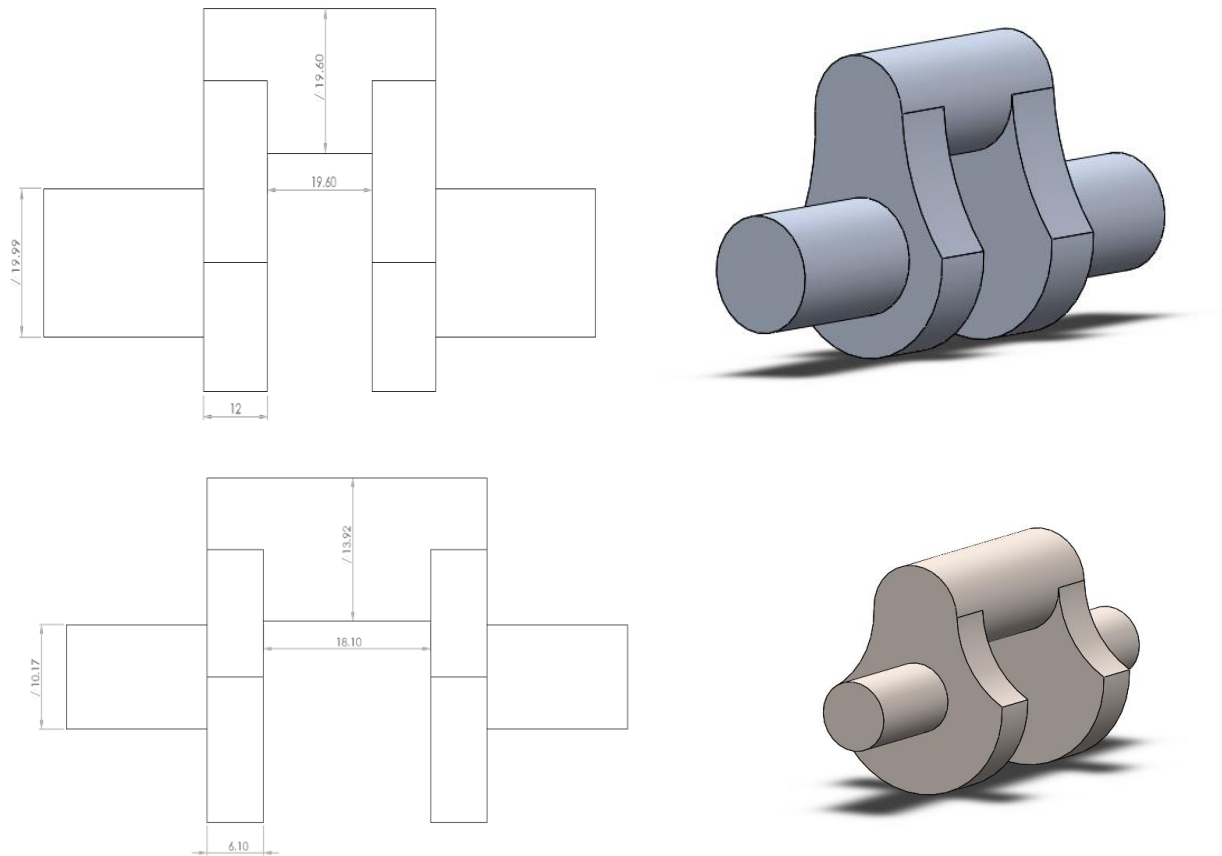


Figure 5-12 2D and 3D models of the crankshaft 1 and 2

5.2.2 FEA structural analysis

The Structural integrity of the design is validated using FEA Structural analysis of the major parts of the compressor assembly.

CAD modeling of compressor 1 and 2 assemblies.

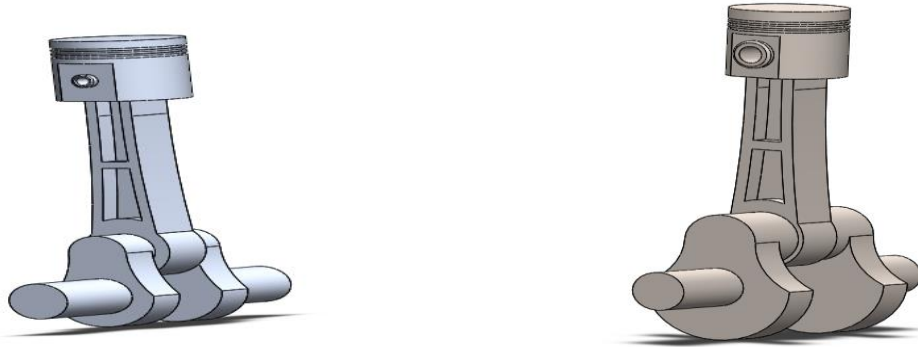


Figure 5-13 Compressor 1 and 2 assemblies

The Solidworks simulation is used for the analysis. The initial step in the simulation is to assign material to the components. The next step is to define connecting rod connection in crankpin and piston pin. Later, the assembly is fixed at the shaft position. Once the material, connections and fixture geometry is assigned, the next step is to apply maximum compressor pressure on piston surface.

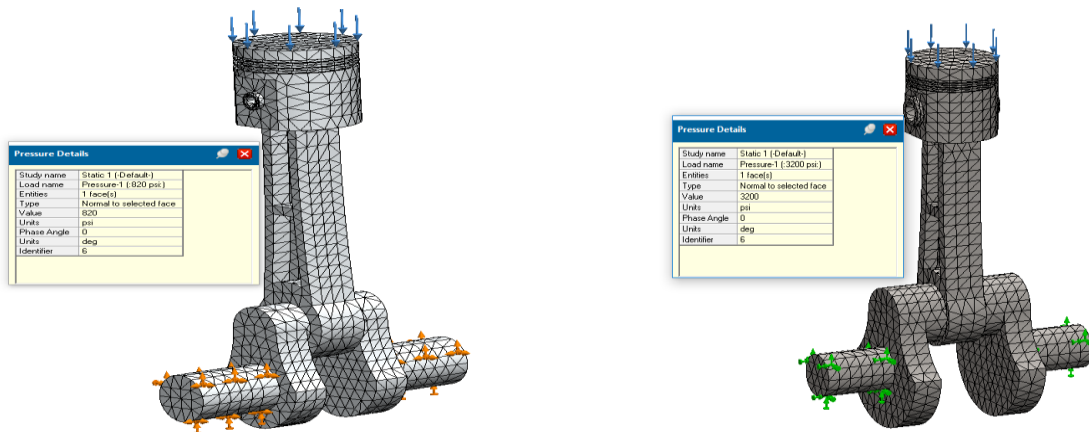


Figure 5-14 Meshing and boundary conditions (pressures and fixtures applied) assemblies

The design is validated by obtaining the von Mises stress and Factor of safety of the assembly. It can be observed from Figure 5-15 & 5-16, the von Mises stress is lower than the yield strength of materials and the factor of safety is observed to be 3.7 and 2 for compressor 1 and 2 respectively. Hence, the design is valid.

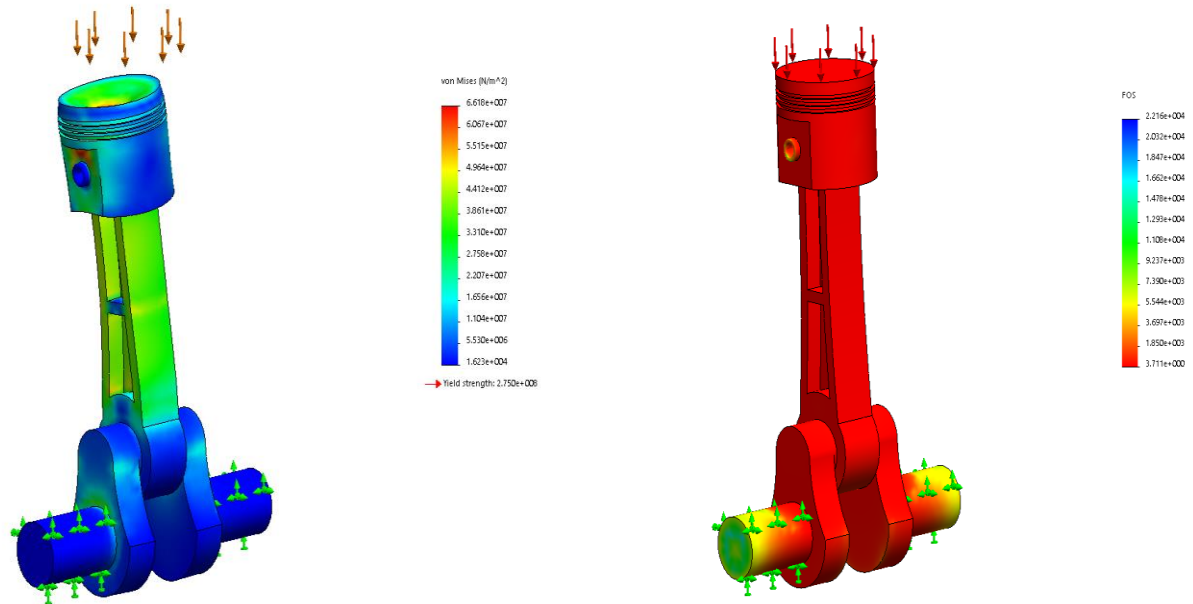


Figure 5-15 Von-Misses stresses of compressor assembly

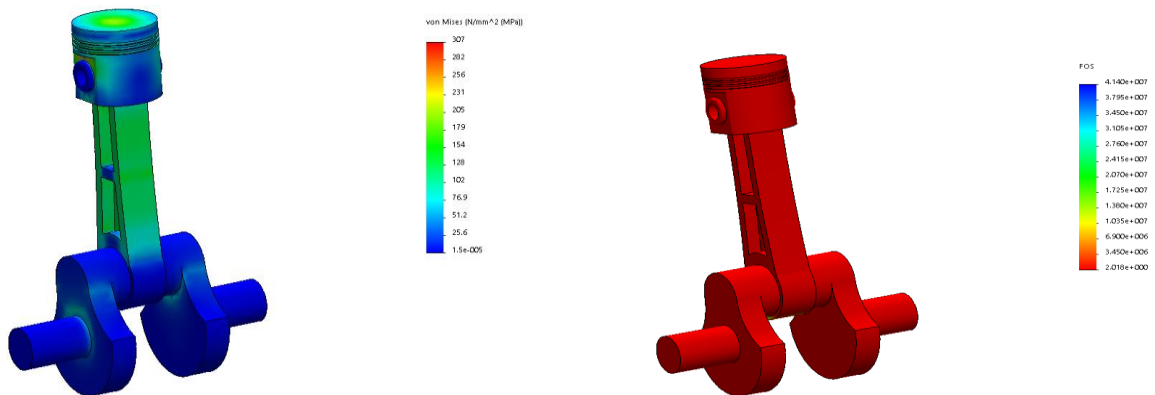


Figure 5-16 Factor of safety for compressor 1 and 2

The other parts of the compressor not included in the design due to time constraint are crankcase, valves and an electric motor. The crankcase is responsible to provide lubrication by holding all the components together. There are two types of lubrication systems available in typical reciprocating compressors such as Cylinder lubrication and Crankcase lubrication. The Cylinder lubrication provides lubrication to the piston, piston rings, cylinder liners, cylinder packing, and valve. Whereas, Crankcase lubrication provides lubrication to main bearings, crank pins, piston pins, and crosshead bearing [34]. The lubricated compressor requires both the cylinder and crankcase lubrication system. But, non-lubricated compressor requires only crankcase lubrication which is suggested to use in the proposed system to eliminate oil leakage to compression chamber and valve chambers. Figure 5-17 shows the assembly of compressor 1 and 2 including crankcase (designed based on major parts).

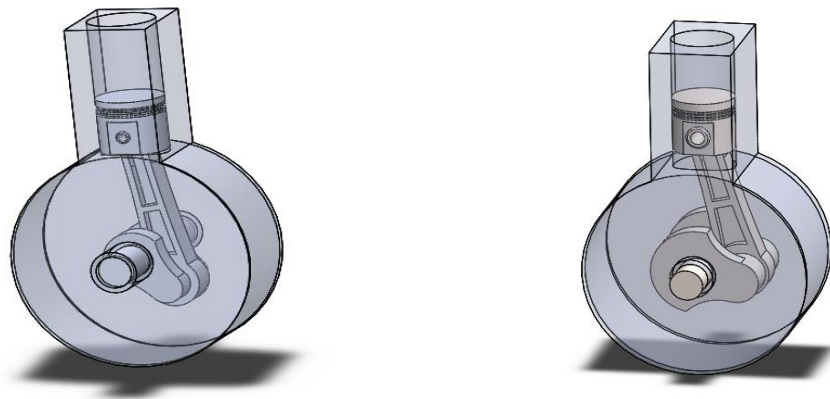


Figure 5-17 Final assemblies of compressors 1 and 2

Compressor valves are the devices placed above the cylinder which regulates the cycle of operations in a cylinder. These valves act as a check valve (one-way valve) which solely opened by the pressure difference across the valve. The selection of the compressor valves depends on the Valve seat geometry, sealing element and the nature of damping used to control the motion. The typical valves based on valve seat geometry are Rectangular valves, Concentric ring valves, Ported Plate valves, and Disc (Poppet) valves. The Rectangular valves are further divided into feather valves, channel valves, and reed valves. The reed valve is recommended to be the best fit the proposed system for its operational capabilities of high-pressure applications and ease of operation. Figure 5-18 shows typical reed valve geometry.

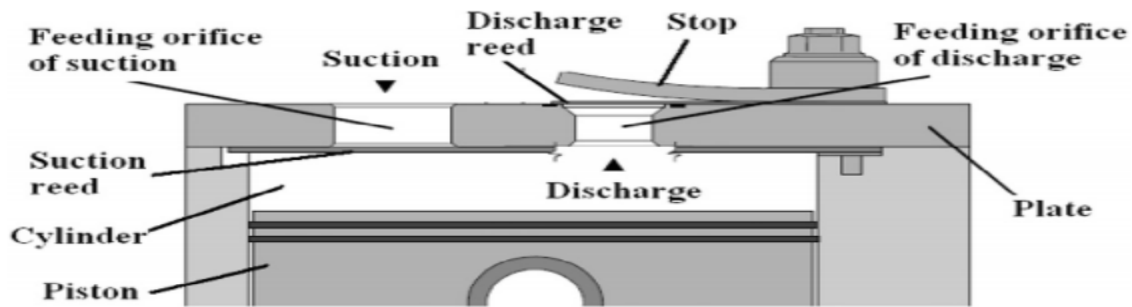


Figure 5-18 Typical reed valve geometry

The electric motor provides the rotary motion to the crankshaft. The drone motors are the perfect fit for the proposed compressors because these are very compact and powerful. The operation of these motors is different from the typical motors used in the compressor, the case surrounding the motor rotates and the inside of the motor is stationary. Brushless out runner DC electric motors are suggested to use in the compressors. The specifications of the electric motors are shown below

Table 5-8 Specifications of commercial electric motor.

Specifications	Electric motor 1	Electric motor 2
Manufacturer	E-flite (Horizon Hobby)	E-flite (Horizon Hobby)
Power	Up to 6000 watts	Up to 275 watts
Cells	12S Li-Po	3S Li-Po
Shaft diameter	10 mm	4 mm
Weight	1.240 kg	0.087 kg

The total weight of the compressor 1 and 2 are estimated from the design (including crankcase, valves and electric motor) are 3.5 kg and 2 kg respectively.

5.3 Heat exchanger design and conjugate heat transfer analysis

The objective of this section is to design heat exchangers to cool the biogas from 908.68 K to liquefaction temperature (216 K). As discussed in process design section, the proposed system requires two heat exchangers to achieve the required heat dissipation. The design requirements of heat exchangers are shown in table 5-9.

Table 5-9 design requirements of heat exchangers

Design requirements	Heat exchanger 1	Heat exchanger 2
Inlet temperature	908.68 K	374.33 K
Required outlet temperature	374.33 K	206.38 K
Required heat dissipation	3.42 kW	0.822 W

The key constraints for the heat exchanger design are weight, size, cost, and the convective fluid. Figure 5-19 shows the broad classification of heat exchangers based on their construction. The typical heat exchangers used in the gas processing industry are Double pipe heat exchanger, Shell and tube heat exchanger, Plate and frame heat exchangers, tube-fin heat exchangers, Spiral heat exchangers, etc. Among all, forced convective tube-fin heat exchanger is chosen for its Proven cooling abilities of pressurized gases and freedom to select convective fluid [35].

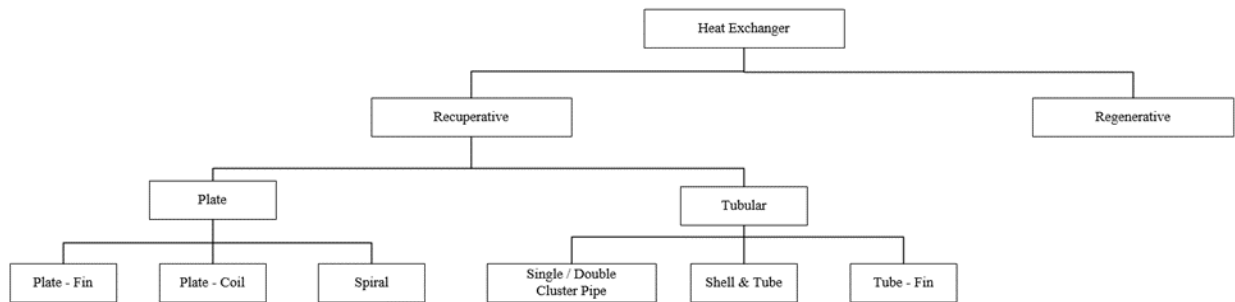


Figure 5-19 Classification of heat exchangers based on their construction

5.3.1 The optimum design of tube-fin heat exchanger

In the tube-fin heat exchanger, the hot fluid flows inside the tube and the convective or cold fluid flows across the tube to dissipate heat from hot fluid to cold fluid. The heat dissipation is increased by either increasing thermal conductivity or total heat transfer area of the fins or by increasing the heat transfer coefficient of convective fluid. Figure 5-20 shows terminology of tube-fin heat exchanger used in the design where 't' is thickness of the fin, 'z' is fin spacing, 'w' is length of the pipe, 'r₁' is inner diameter of the tube, 'a' is fin width, 'T_∞' is coolant temperature, and 'U_∞' is convective fluid velocity.

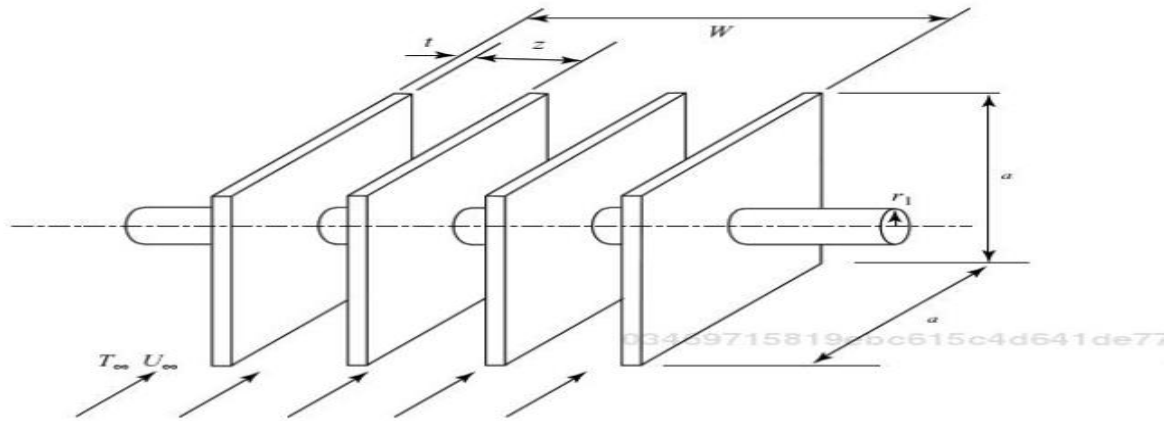


Figure 5-20 Tube-fin heat exchanger

The initial step is, to find the properties of each fluid at film temperature (average of initial inlet and desired outlet temperature). The required heat dissipation is calculated using the first law of thermodynamics neglecting kinetic, potential and network done on the system.

$$Q_{dis} = \dot{m} C_p \Delta T \quad (5.40)$$

Later, a suitable tube is found to meet the design pressure and temperature with the factor of safety. This is completed using the Boardman formula (ASTM B210) as a function of outer tube diameter (D₀), thickness (t) and yield strength (σ_{yield}) of the material.

$$P_{allow} = \frac{2 \sigma_{yield} t}{D_o SF - 0.8 t} \quad (5.41)$$

The optimum tube-fin design equations proposed by Dr. Lee (Wiley, 2011) are,

The Reynolds number as a function of fin width (a), convective fluid velocity (U_∞) and kinematic viscosity (ν)

$$Re = \frac{U_\infty a}{\nu} \quad (5.42)$$

The optimum fin spacing as a function of Convective Reynolds number (Re) and Prandtl number (Pr)

$$z_{opt} = a 3.24 Re^{\frac{-1}{2}} Pr^{\frac{-1}{4}} \quad (5.43)$$

The average Heat transfer coefficient as a function of thermal conductivity (k), Reynolds number (Re) and Prandtl number (Pr)

$$h = \frac{k}{a} 0.664 Re^{\frac{1}{2}} Pr^{\frac{-1}{4}} \quad (5.44)$$

The fin efficiency is calculated from the Bessel's relation as

$$\eta_f = C_1 \frac{K_1(mr_1)I_1(mr_2) - I_1(mr_1)K_1(mr_2)}{I_0(mr_1)K_1(mr_2) + K_0(mr_1)I_1(mr_2)} \quad (5.45)$$

Where, $C_1 = \frac{2 r_1/m}{r_2^2 - r_1^2}$, $m = (\frac{2h}{kt})^{\frac{1}{2}}$, $r_1 = \frac{d_i}{2}$, $r_2 = \frac{a}{\pi}$.

The total number of fins as a function of pipe length (W), optimum spacing (z) and thickness (t)

$$n_f = \frac{W}{z + t} \quad (5.46)$$

The single fin area (A_f) is determined by radii and thickness as

$$A_f = 2\pi(r_2^2 - r_1^2) + 2\pi r_2 t \quad (5.47)$$

The total heat transfer area (A_t) is

$$A_t = n_f (A_f + 2\pi r_1 z_{opt}) \quad (5.48)$$

The overall surface efficiency (η_o) is obtained as

$$\eta_o = 1 - n_f \frac{A_f}{A_t} (1 - \eta_f) \quad (5.49)$$

The outlet temperature (T_o) is

$$T_o = \frac{Q_{dis}}{\eta_o h A} + T_{inf} \quad (5.50)$$

Length of the pipe (W_{req}) required

$$W_{req} = (z_{opt} + t) n_f \quad (5.51)$$

Mass of the pipe (m_p) required

$$m_p = \rho_{pipe} \pi W \left(\left(\frac{D_o}{2} \right)^2 - r_1^2 \right) \quad (5.52)$$

Mass of the fin (m_f)

$$m_f = \rho_{pipe} \pi t (r_2^2 - r_1^2) n_f \quad (5.53)$$

Total mass of the heat exchanger (m_{he})

$$m_{he} = m_p + m_f \quad (5.54)$$

The biogas pressure drop is calculated using,

$$\Delta P = 2 f \left(\frac{W}{d_i} \right) (\rho_{bio} V_{bio}^2) \quad (5.55)$$

Where ‘ f ’ is the fanning friction factor taken as 0.2 from the moody chart based on biogas Reynolds number.

‘ V_{bio} ’ is the velocity of biogas inside the pipe which is calculated by $V_{bio} = \frac{m_{dot}}{\rho_{bio} \frac{\pi d_i^2}{4}}$

The Reynolds number of biogas flowing inside the pipe is $Re_{bio} = \frac{4 m_{dot}}{\pi d_i \mu}$

An iterative Mathcad program is developed using the optimum tube – fin design equations as a function of thickness (t), Pipe length (W), Fin width (a) and coolant velocity (U_∞). Figure 5-21 shows the process flow of the optimal tube – fin design Mathcad program.

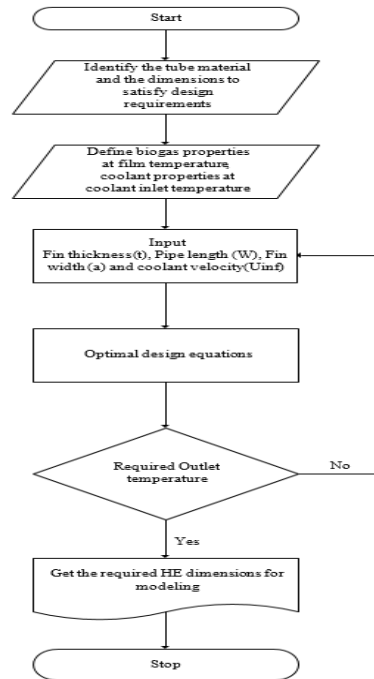


Figure 5-21 Process flow of the optimal tube – fin design

Standard 1/8'' schedule 10 bare aluminum 6061 – T6 pipe satisfies the design requirements with safety factor 3. The properties of biogas at film temperatures of heat exchanger1 and 2 are shown below in Table 5-10.

Table 5-10 Properties of biogas at film temperatures

Property	Biogas (641.50 K)	Biogas (290.89 K)
Specific heat at constant pressure (C_p)	$1.53 \frac{kJ}{kg K}$	$1.16 \frac{kJ}{kg K}$
Dynamic viscosity (μ)	$2.72 \times 10^{-5} \frac{kg}{m s}$	$1.40 \times 10^{-5} \frac{kg}{m s}$
Kinematic viscosity (ν)	$8.54 \times 10^{-7} \frac{m^2}{s}$	$4.41 \times 10^{-7} \frac{m^2}{s}$
Thermal conductivity (k)	$0.043 \frac{W}{m K}$	$0.021 \frac{W}{m K}$
Density (ρ)	$31.48 \frac{kg}{m^3}$	$54.41 \frac{kg}{m^3}$

As discussed in section 5.1.2., the ambient air is used as a convective fluid for heat exchanger 1 whereas, expanded liquid CO₂ is used for heat exchanger 2. The properties of convective fluids at inlet temperature are shown below in Table 5-11.

Table 5-11 Properties of convective fluids at inlet temperatures

Property	Ambient air (300 K)	Expanded CO ₂ (156.91 K)
Specific heat at constant pressure (C_p)	$1.00 \frac{kJ}{kg K}$	$0.838 \frac{kJ}{kg K}$
Dynamic viscosity (μ)	$1.84 \times 10^{-5} \frac{kg}{m s}$	$1.45 \times 10^{-5} \frac{kg}{m s}$
Kinematic viscosity (ν)	$1.56 \times 10^{-5} \frac{m^2}{s}$	$7.88 \times 10^{-6} \frac{m^2}{s}$

Thermal conductivity (k)	$0.026 \frac{W}{m K}$	$0.034 \frac{W}{m K}$
Density (ρ)	$1.17 \frac{kg}{m^3}$	$1.84 \frac{kg}{m^3}$

After numerous iterations, the final input properties of heat exchangers are shown in Table 5-12.

Table 5-12 Final input properties of heat exchangers

Property	Heat exchanger 1	Heat exchanger 2
Fin thickness (t)	1.2 mm	1.2 mm
Pipe length (W)	1.5 mm	1.2 mm
Fin width (a)	40 mm	40 mm
Convective fluid velocity (U_{∞})	9.55 m/s	1.72 m/s

The final output properties of the heat exchangers are tabulated in Table 5-13.

Table 5-13 Output properties of the heat exchangers

Property	Heat exchanger 1	Heat exchanger 2
Outlet temperature (T_0)	375.41 K	207.33 K
Optimum fin spacing (z_{opt})	0.904 mm	1.792 mm
Average heat transfer coefficient of Convective fluid (h)	60.15 W/m ² *K	37.475 W/m ² *K
Average heat transfer coefficient of biogas (h_{bio})	4.82 W/m ² *K	6.03 W/m ² *K
Number of radial fins (n_f)	713	402
Total heat transfer area (A_t)	0.791 m ²	0.448 m ²
Overall surface efficiency (η_o)	95 %	97 %
Mass of heat exchanger (m_{he})	1.204 kg	0.688 kg

Pressure drop (ΔP)	2.69 bar	2.15 bar
------------------------------	----------	----------

From the table, it can be observed that the ambient air velocity is not enough to achieve the required heat dissipation of heat exchanger 1. So, forced convection is needed to provide the required air velocity. Forced convection is achieved by attaching a fan to heat exchanger. A commercial round axial fan of 10'' inch (254 mm) diameter is chosen for its high volumetric flow capacity (500 CFM). The pipe is turned 180 degrees to provide constant air velocity throughout the effective heat transfer area. The heat exchanger 1 is enclosed in a box ($250 \times 240 \times 40$ mm), this constraint makes the 1.5 m single pipe to 6 pipes of dimension 250 mm each. These pipes are joined by pipe bends of radius 40 mm (which is the fin width). Heat exchanger 2 uses liquid CO₂ as a convective fluid by expanding it from liquefaction pressure to ambient pressure (0.101 MPa). This expansion requires an expansion valve to control the velocity of the expanded CO₂ gas. The box ($240 \times 200 \times 40$ mm) is chosen based on heat exchanger 2 dimensions. The final dimensions of the heat exchangers are shown below in Table 5-14.

Table 5-14 Final dimensions of the heat exchangers

Final design	Heat exchangers 1	Heat exchanger 2
Size (W \times H \times D)	$250 \times 240 \times 40$	$240 \times 200 \times 40$
Inside diameter of the pipe	2.98 mm	2.98 mm
Outside diameter of the pipe	4.76 mm	4.76 mm
Number of rectangular fins	119	81
Fin spacing	0.904	1.792 mm
Fin thickness	1.2 mm	1.2 mm
Mass	1.204	0.688 kg
Mass of fan	0.500 kg

CAD modeling of heat exchanger 1 and 2 shown in Figure 5-22.

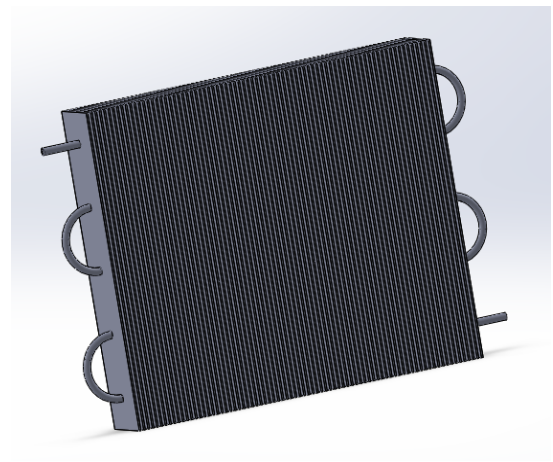
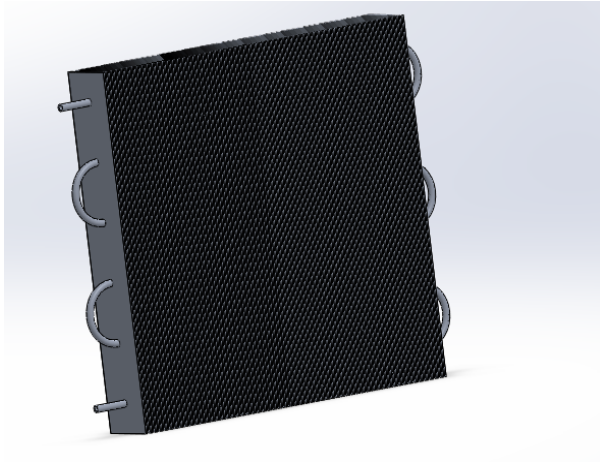


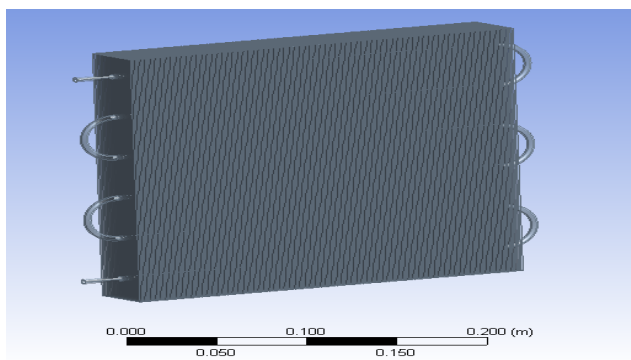
Figure 5-22 3D models of heat exchanger 1 and 2

5.3.2 CFD Conjugate heat transfer analysis

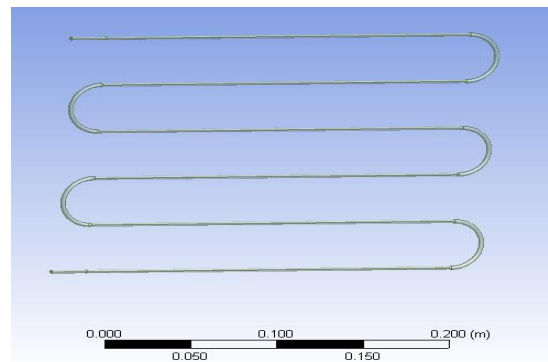
Conjugate heat transfer analysis is performed to verify the heat exchanger design using ANSYS - CFX. The analysis involves the following steps.

Step 1- Import Geometry to ANSYS design modular.

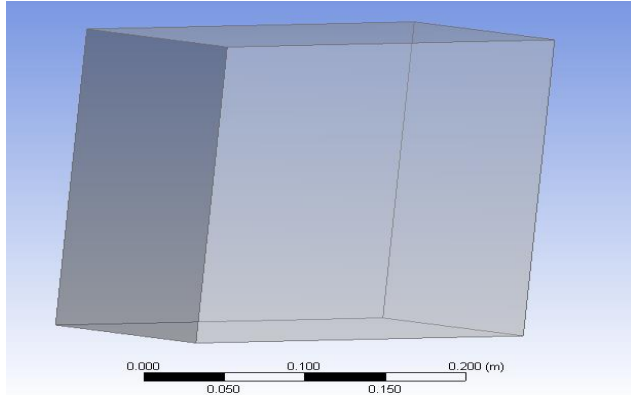
The imported geometry is shown in Figure 5-23.



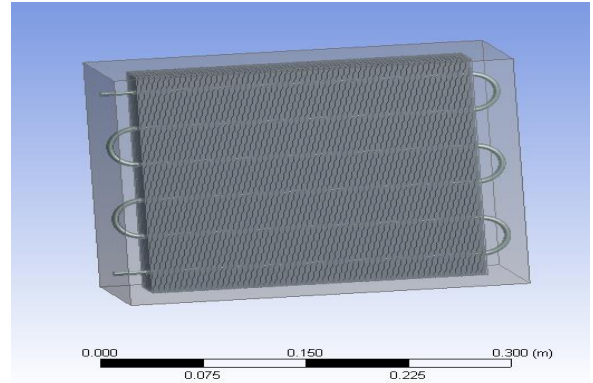
a) Heat exchanger body.



b) Biogas body.



c) Convective fluid body.

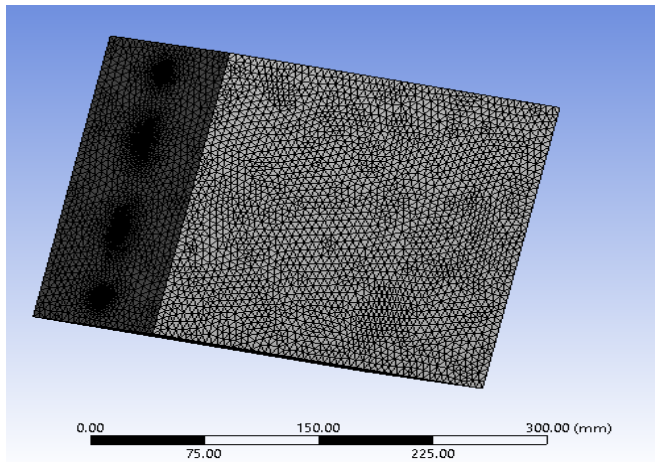


d) HE Assembly.

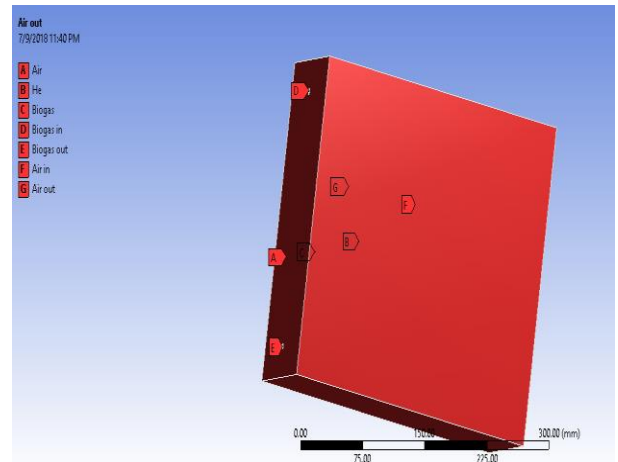
Figure 5-23 Heat exchanger geometry

Step 2 -Meshing in ANSYS - Mesh

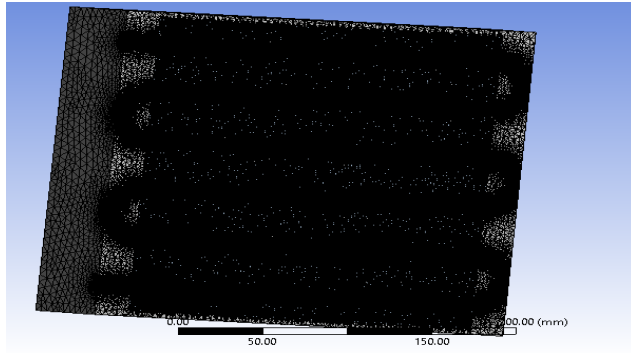
Meshing plays an important role in accurately solving the model as all the governing equations are solved in discretized nodes. ANSYS Default mesh is used in the present analysis.



a) Fine mesh of the assembly



b) Named selections of the mesh.



c) Cross section of mesh



Details of "Mesh"	
Display	Body Color
Defaults	
Physics Preference	CFD
Solver Preference	CFX
Relevance	0
Element Order	Linear
Sizing	
Quality	
Inflation	
Advanced	
Statistics	
Nodes	1499414
Elements	7642690

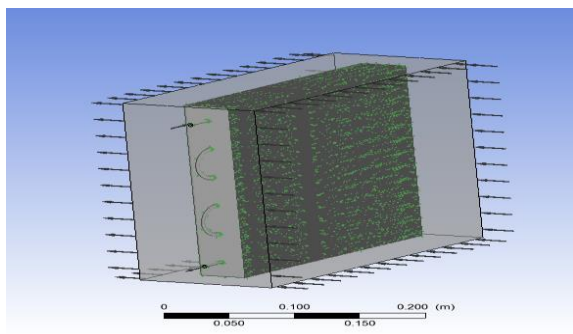
d) Statistics of the mesh.

Figure 5-24 Heat exchanger meshing

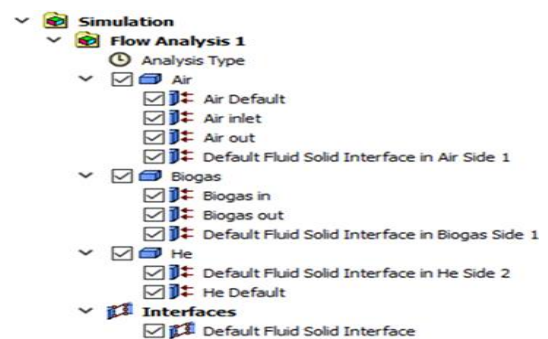
Figure 5-24 (b) Highlights the named selections of the mesh, where A, B, C represents the domains of convective fluid (this case air), heat exchanger and biogas respectively. D, E, F, G represents the boundaries of biogas in, biogas out, convective fluid in and convective fluid out.

Step 3- Problem Setup in ANSYS – CFX (pre)

In Figure 5-25 (a), the arrow symbols denote the boundary conditions of the domains. b) shows the problem setup tree, where  symbol denotes the domain type and  symbol donates the boundary conditions



(a) HE surrounded by convective fluid.



b) Problem setup tree Figure.

Figure 5-25 Problem setup

The problem setup in steady state conjugate heat transfer analysis is divided into three parts such as

1. Domain type and model setup is completed by assigning the material and the model for each domain as shown in Table 5-15.

Table 5-15 Domain setup

Input	Biogas domain	Air domain	CO ₂ domain	He domain
Domain type	Fluid	Fluid	Fluid	Solid
Material	Biogas	Air ideal gas	Carbon dioxide	Aluminum
Morphology	Continuous fluid	Continuous fluid	Continuous fluid	Continuous solid
Reference pressure	Critical pressure	1 bar	1 bar	-----
Heat transfer model	Thermal energy	Thermal energy	Thermal energy	Thermal energy
Turbulence model	k-Epsilon	k-Epsilon	k-Epsilon	-----
Heat flux	-----	-----	-----	4.3 kW/m ² (He 1) 1.8 kW/m ² (He 2)

2. Boundary conditions are defined for each fluid domain as shown in Table 5-16.

Table 5-16 Boundary conditions

Input	Biogas in	Biogas out	Air in	Air out	CO ₂ in	CO ₂ out
Flow regime	Subsonic	Subsonic	Subsonic	Subsonic	Subsonic	Subsonic
Normal fluid velocity in	-----	-----	9.55 m/s	-----	1.77 m/s	-----
Mass flow rate in	15 kg/hr	-----	-----	-----	-----	-----
Inlet temperature of He1	908.68 K	-----	300 K	-----	-----	-----
Inlet temperature of He2	375.414 K	-----	-----	-----	156.91 K	-----
Outlet relative pressure	-----	0	-----	0	-----	0

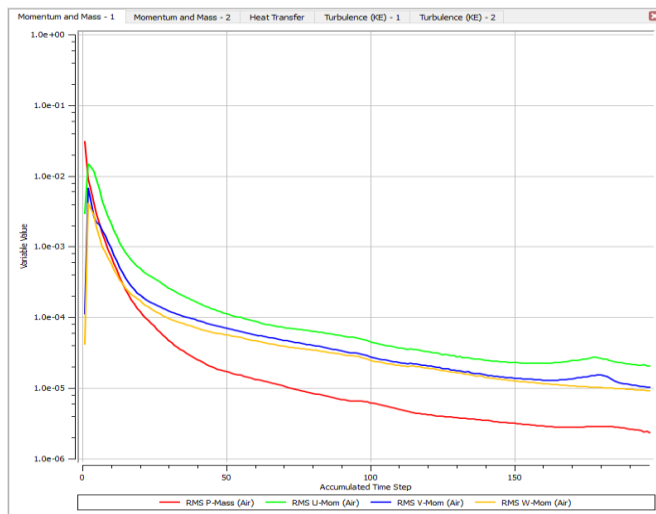
3. Fluid solid interface is defined as shown in Table 5-17.

Table 5-17 Fluid solid interface

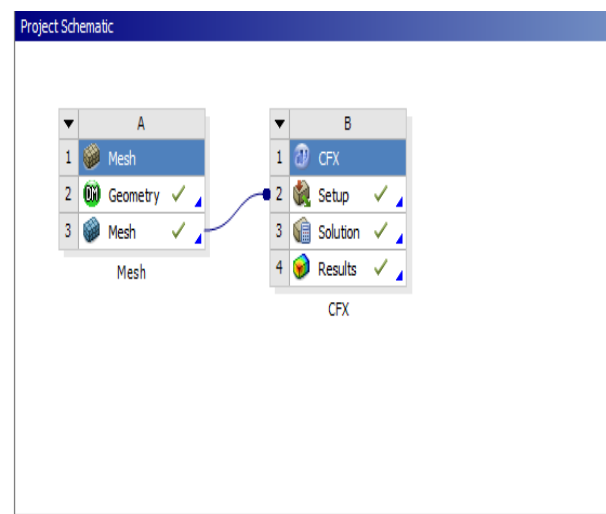
Input at interface	Biogas to He 1	Biogas to He 2	Air to He 1	CO ₂ to He 2
Average heat – transfer Coefficient	4.82 W/m ² *K	6.03 W/m ² *K	60.15 W/m ² *K	37.47 W/m ² *K
Average fluid temperature	641.50 K	290.89 K	320 K	180 K

Step 4 - Numerical solution in CFX-solver manager

An iterative solution is obtained by solving mass, moment, energy and turbulent equations for both the fluids using the finite volume method. The solution converges at around 220 iterations which took about 9 hours to complete the solution. Figure 5-26 (a) shows the convergence of mass and momentum equations of convective fluid, it can be stated that similar convergence is achieved for the rest of the equations.



a) Convergence



b) ANSYS – CFX workflow

Figure 5-26 Convergence criteria and workflow

Step 5- Results in CFD -Post-processing

Figure 5-27 & 5-28 shows the contours of biogas temperature in HE1 and HE2, it can be observed that the average outlet temperatures of HE1 and HE2 are 383.5 K, 195.5 K respectively.

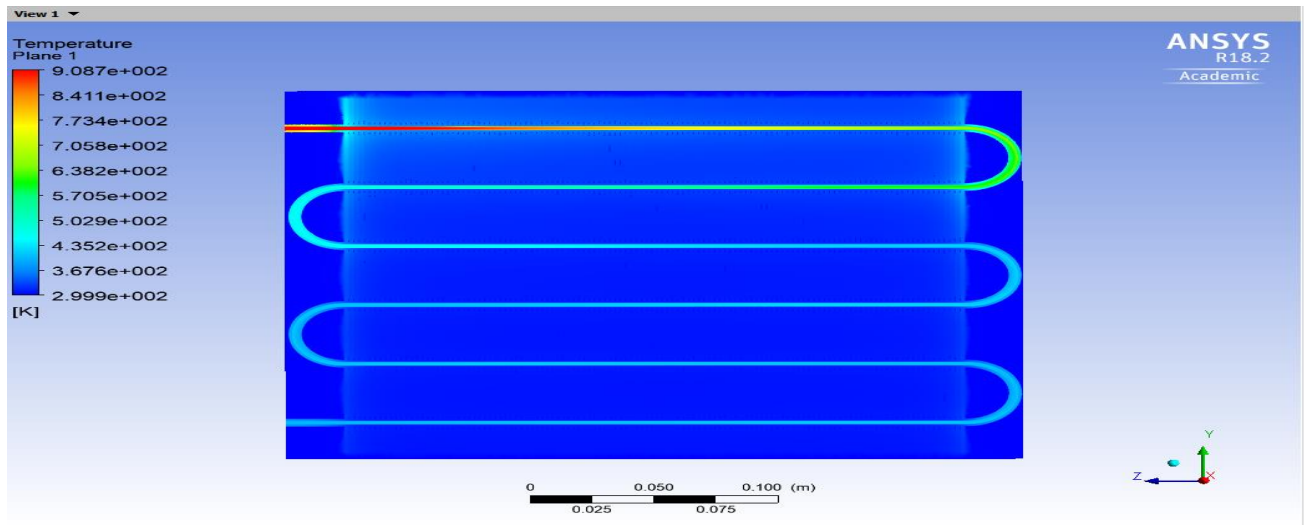


Figure 5-27 Contours of biogas temperature in HE1

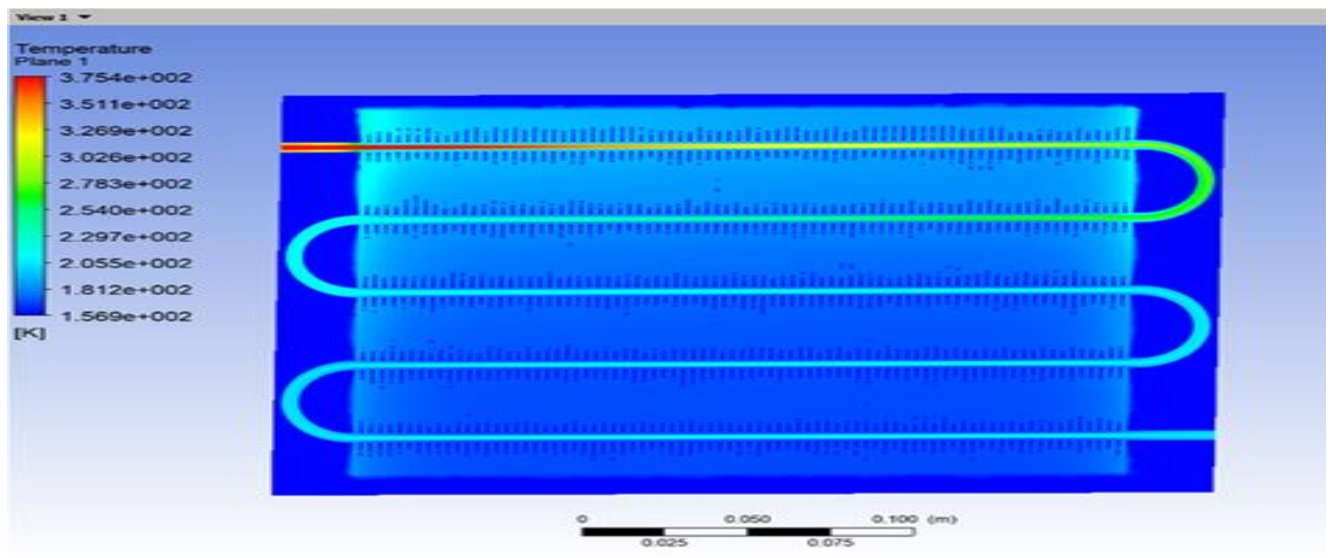


Figure 5-28 Contours of biogas temperature in HE2

Figure 5-29 & 5-30 depicts the temperature contours of convective fluid at fluid outlet. The maximum temperature is observed at biogas inlet location which is 329 K for convective fluid 1 and 171 K for convective fluid 2.

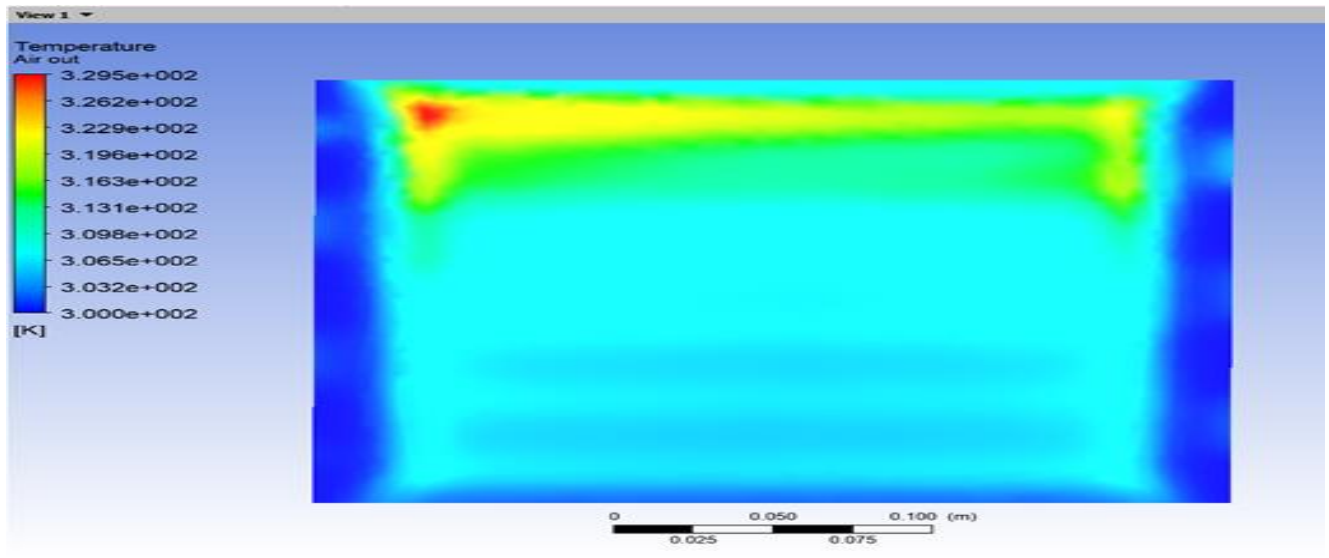


Figure 5-29 Temperature contours of convective fluid 1 (air) at the outlet

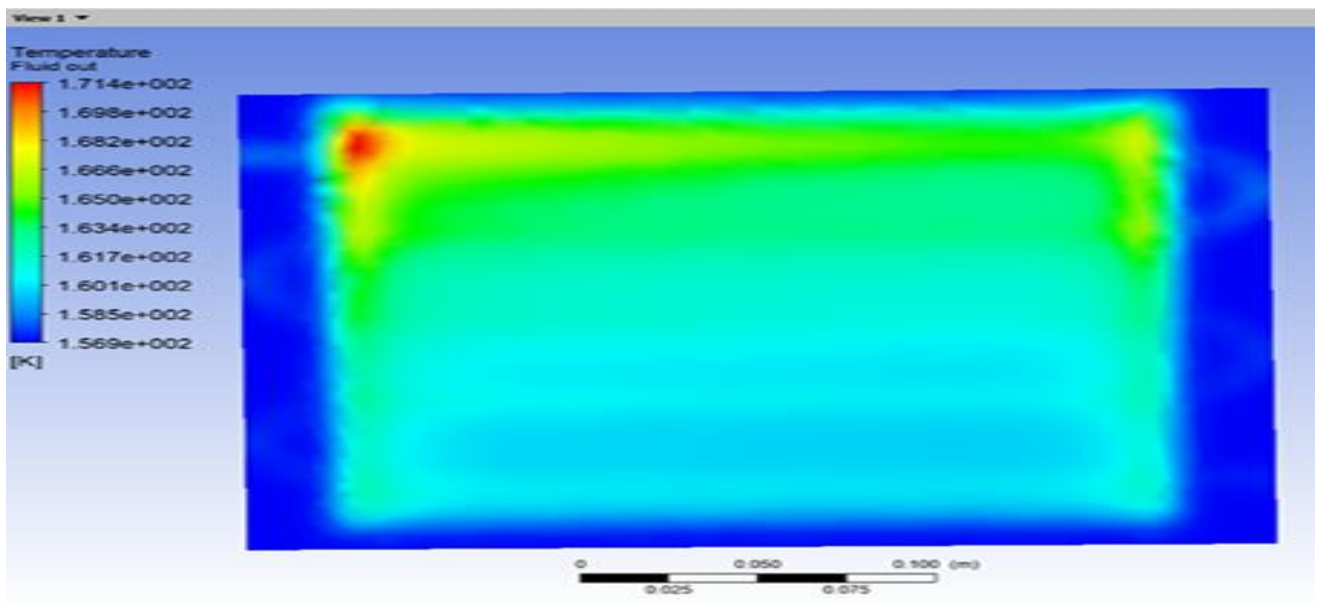


Figure 5-30 Contours of convective fluid 2 (expanded liquid CO₂) temperature at the outlet

Figure 5-31 & 5-32 shows the velocity vectors of convective fluid 1 and convective fluid 2. The maximum velocity is observed at the fin spacing which is 38 m/s for convective fluid 1 and 13 m/s for convective fluid 2.

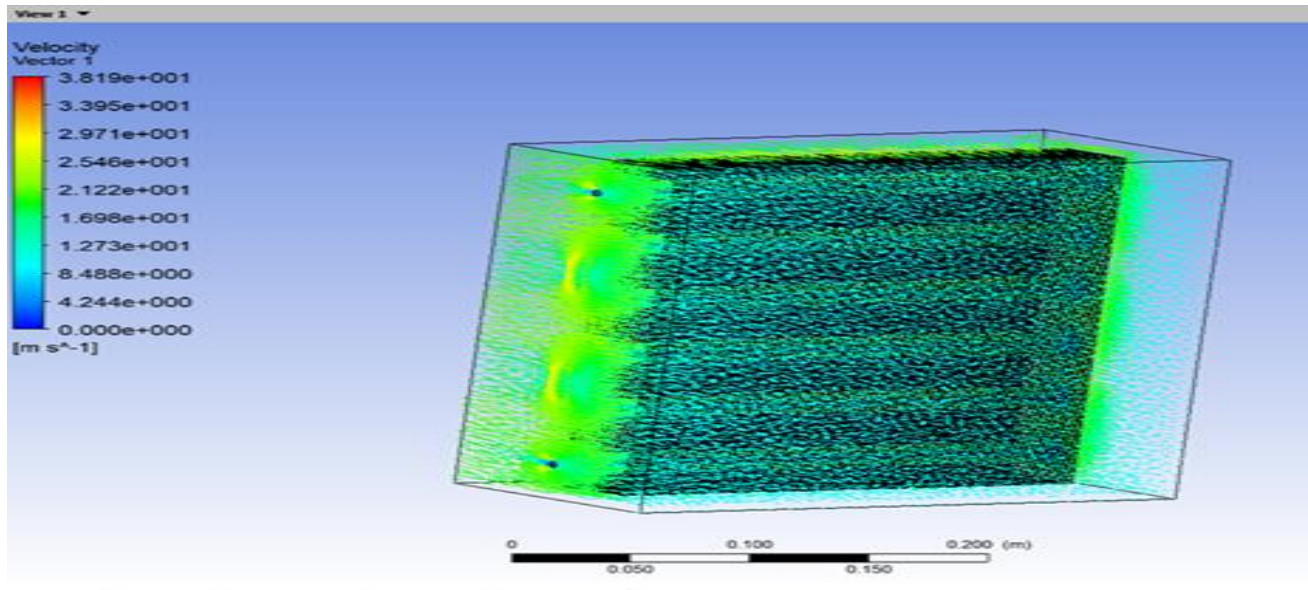


Figure 5-31 Velocity vectors of convective fluid 1

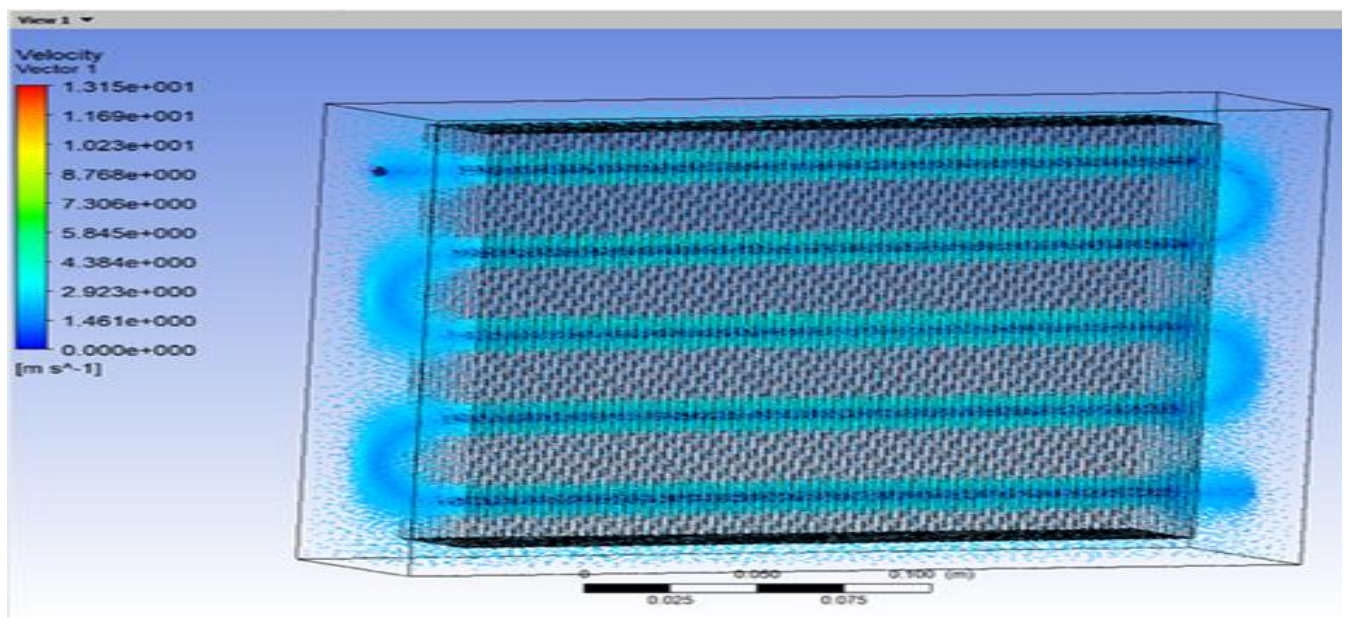


Figure 5-32 Velocity vectors of convective fluid 2

Table 5-18 compares the ANSYS - CFX simulation results with Mathcad design. It can be seen that the ANSYS – CFX simulations successfully validate the Mathcad design with less than 5 % error. Hence, the design is valid.

Table 5-18 Validation of ANSYS - CFX simulation results with Mathcad design

Parameter	Heat exchanger 1 (Mathcad)	Heat exchanger 1 (ANSYS –CFX)	Heat exchanger 2 (Math cad)	Heat exchanger 2 (ANSYS – CFX)
Outlet biogas temperature	375.41 K	383.5 K	207. 33 K	195.5 K

5.4 Liquid-Gas separator design and multi-phase analysis

Based on biogas phase diagram (shown in figure 3-6), CO_2 is expected to transform phase from gas to liquid at heat exchanger 2 outlet. This two-phase mixture is sent to phase separator typically called Liquid Gas Separator (LGS). The goal of LGS is to separate the dispersed fluid (CO_2 liquid) from continuous fluid (CH_4 gas). The separator selection is mainly based on flow regime, separation methodology, and separator geometry. The flow regime depends on the interface between continuous and dispersed fluids. The typical flow regimes are Droplet flow, Plug flow, Stratified flow, Wavy flow, Slug flow, and Annular flow. The inlet flow is assumed to be the droplet flow, as the CO_2 droplets are dispersed through CH_4 gas. Figure 5-33, shows the typical liquid-gas separators used in the gas processing industry [36].

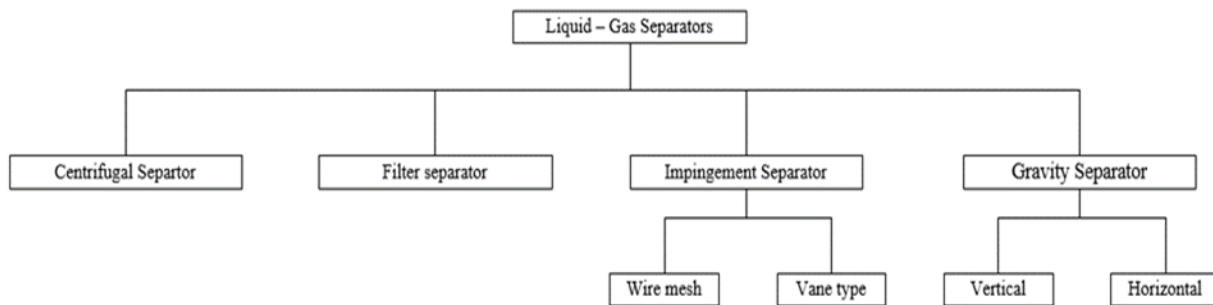


Figure 5-33 Types of Liquid-Gas Separators

Centrifugal separation occurs when the centrifugal force of dispersed fluid exceeds drag force by flowing gas. An external source is used to increase the centrifugal force. The filter separator creates a torturous path/obstacle to the liquid droplet, this decreases the velocity of liquid droplets and it eventually falls down to the bottom of the vessel. The Impingement separator uses mist pads to separate liquid droplets by crafting the inertial impaction. The final separator type is the gravity separator which occurs when the gravitation force on liquid droplets exceeds drag force of the gas molecule [37]. This is simple and efficient to separate high gas-liquid ratios. These are oriented either vertically or horizontally. The proposed system is decided to use gravity separation mechanism of vertical orientation.

5.4.1 Design

The gravity liquid-gas separator (LGS) is divided into four sections as shown in figure 5-34. The first section is the inlet device, which reduces the momentum of the inlet stream to impinge liquid droplets on the inlet device then it drops by gravity. The various types of inlet devices commonly used are no inlet device, diverter plate, half-pipe, vane-type and cyclonic. The next section is the gas gravity separation section; it uses the force of gravity to separate the entrained liquid droplet from the gas phase. The third section is liquid gravity separation section, which acts as a reservoir for the removed liquid. The final section is the mist extraction section which utilizes the mist extractor consists of a knitted wire mesh pad, a series of vanes, or cyclone tube [38].

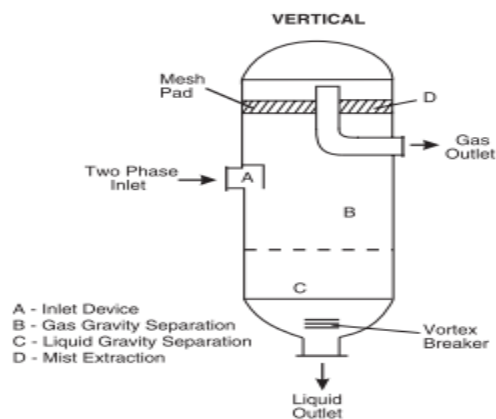


Figure 5-34 Gravity Liquid-Gas Separator [38]

The first step in the design process is to identify the inlet device, no inlet device is chosen to minimize the design complexity. The next step is to determine the required disengagement space for gas gravity separation section. This can be achieved by determining the allowable maximum gas velocity. There are two methods to achieve this object, those are The Sounders – Brown approach (K_s Method) and Droplet settling theory. The Sounders – Brown approach determines allowable maximum gas velocity by balancing forces on liquid droplet whereas, the droplet settling theory determines droplet settling or terminal velocity by following similar force balance. The typical forces acting on liquid droplet are gravity and drag forces. The net force causes the momentum in the same direction. The forces acting on the spherical liquid droplet of diameter ' D_p ' are

Drag force (F_d) by the momentum of a gas molecule is

$$F_d = \frac{C_d A_p \rho_{co2} v_{ch4}}{2} \quad (5.56)$$

Where, A_p is the droplet projected area, defined by $A_p = \frac{\pi}{4} D_p^2$

Gravity force (F_g) by the weight of liquid droplet is

$$F_g = (\rho_{co2} - \rho_{ch4}) V_p g \quad (5.57)$$

Where V_p is the volume of spherical droplet calculated by $V_p = \frac{\pi}{6} D_p^3$

At an equilibrium, the gravity force is equal to drag force, solving equation (5.56) & (5.57) for the maximum gas velocity (v_{max}) gives

$$V_{gmax} = \sqrt{\left(\frac{4 g D_p}{3 C_D}\right) \left(\frac{\rho_{co2} - \rho_{ch4}}{\rho_{ch4}}\right)} \quad (5.58)$$

The first term in equation (5.58) is replaced by K_s , then the equation is called Sounders-brown's equation, the equation becomes

$$V_{gmax} = K_S \sqrt{\frac{\rho_{co2} - \rho_{ch4}}{\rho_{ch4}}} \quad (5.59)$$

K_S is referred as design parameter which can be estimated using the empirical relation, this relation is based on operating pressure (P) and droplet size.

$$K_S = a + b P + c P^2 + d P^3 \quad (5.60)$$

The minimum droplet size is assumed as 100 μm , and the empirical constants for this droplet size are as follows

$$a = 0.044882$$

$$b = 7.24\text{E} - 5$$

$$c = -5.5\text{E} - 08$$

$$d = 1.58\text{E}-11$$

Once the maximum gas velocity is obtained, the next step is to calculate design velocity (v_d) by multiplying selected design factor (percent from 0 to 100 %) to maximum gas velocity.

$$v_d = V_{gmax} V_{df} \quad (5.61)$$

The required vessel diameter is determined from design velocity (v_d) and volumetric gas flow rate (V_{dotg}) as

$$D_v = \sqrt{\frac{4 V_{dotg}}{\pi v_d}} \quad (5.62)$$

The gas space is assumed to be equal to vessel diameter as per ANSI/API Standard 521. It can be written as

$$L_g = D_v \quad (5.63)$$

Later, the liquid gravity separation section is designed by assuming the residence time (t_r) of liquid on the vessel.

The GPSA Data book [38] suggested the typical residence time for a Natural gas - condensate separation should be within 2 to 5 minutes. The liquid space (L_l) from liquid volumetric flow rate (V_{dotl}) and density (ρ_l) as

$$L_l = \frac{4 V_{dotl}}{\pi D_v^2} t_r \quad (5.64)$$

The liquid outlet diameter is calculated from outlet liquid velocity (V_{lo}) as

$$D_{lo} = \sqrt{\frac{4 V_{dotl}}{\pi V_{lo}}} \quad (5.65)$$

The gas outlet diameter from outlet gas velocity (V_{go}) as

$$D_{go} = \sqrt{\frac{4 V_{dotg}}{\pi V_{go}}} \quad (5.66)$$

The selection of mist extractor is based on the gas-liquid ratio in the inlet stream. Tamagna et al., [39] suggested that no mist extractor is required for an inlet stream of high gas-liquid ratio. So, the proposed liquid-gas separator is designed with no mist extractor. The final step in LGS design is to determine the required vessel thickness (t_v) to hold the pressure which is calculated using ASME Section VIII Division 1 code based on material yield strength (σ_{yeild}), inner vessel radius (r_i), Design pressure (P_d) and joint efficiency (E) as

$$t_v = \frac{P_d r_i}{\sigma_{yeild} E - 0.6 P_d} \quad (5.67)$$

The input parameters required for LGS design are shown in Table 5-19.

Table 5-19 Input parameters required for LGS design

Parameter	Value
Mass flow rate of liquid CO ₂ (\dot{m}_{co2})	11 kg/hr
Mass flow rate of gaseous CH ₄ (\dot{m}_{ch4})	4 kg/hr
Density of CO ₂ (ρ_{co2})	468.2 kg/m ³ (Critical density is assumed)
Density of CH ₄ (ρ_{ch4})	51.99 kg/m ³
Volumetric flow rate of CO ₂ (\dot{v}_{co2})	0.023 m ³ /hr
Volumetric flow rate of CH ₄ (\dot{v}_{ch4})	0.077 m ³ /hr
Volume fraction of CO ₂ (y_{co2})	0.23
Volume fraction of CH ₄ (y_{ch4})	0.76

The final parameters of LGS are shown in Table 5-20.

Table 5-20 Final parameters of LGS

Parameter	Value
CO ₂ liquid droplet size (D_p)	100 μ m
Design parameter (K_s)	0.023 m/s
Maximum gas velocity (v_{gmax})	0.068 m/s
Design gas velocity (v_d)	0.01 m/s
Vessel diameter (D_v)	94.95 mm
Gas space (L_g)	94.95 mm
Liquid space (L_l)	165.87 mm

Inlet diameter (D_{in})	11.48 mm
Liquid outlet diameter (D_{lo})	11.48 mm
Gas outlet diameter (D_{go})	18.56 mm
Thickness	3.01 mm
Mass of LGS	0.653 kg

CAD modeling of Liquid Gas Separator shown in Figure 5-35.

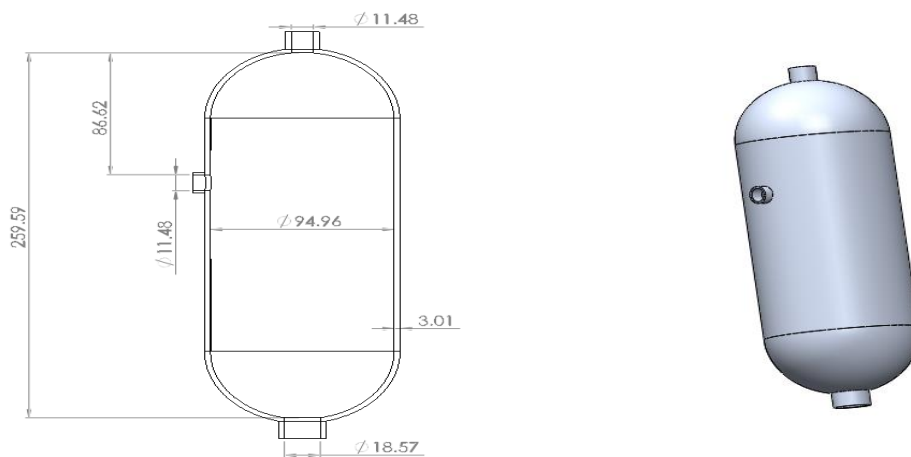


Figure 5-35 2D and 3D model of LGS

5.4.2 CFD multi-phase Analysis

The design is validated by steady-state Multi-Phase Analysis using ANSYS – CFX. This analysis is carried out by importing fluid geometry from CAD software, meshing it to create finite number of elements then assign domain properties and boundary conditions to approximate the solution by solving governing equations using various numerical techniques. Later, the results are analyzed to validate the design.

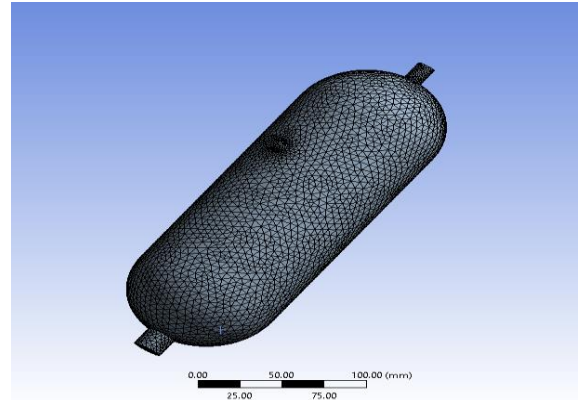
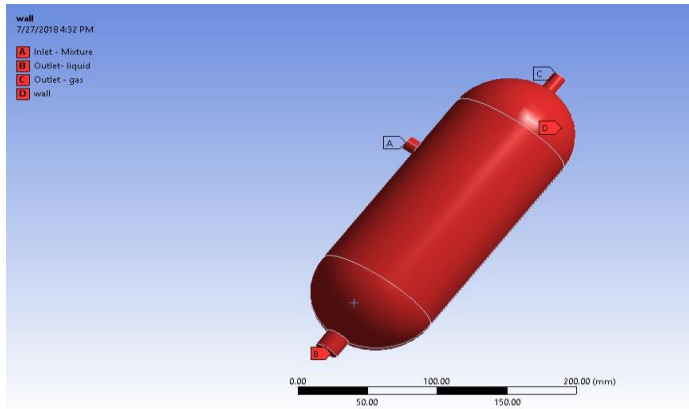

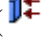


Figure 5-36 a) Imported fluid CAD geometry with named selections and b) Fine mesh

The Parameters/models are assigned to fluid volume () and surfaces (). Figure 5-37 shows the ANSYS – CFX (pre) problem setup tree and fluid domain with the boundary conditions, respectively.

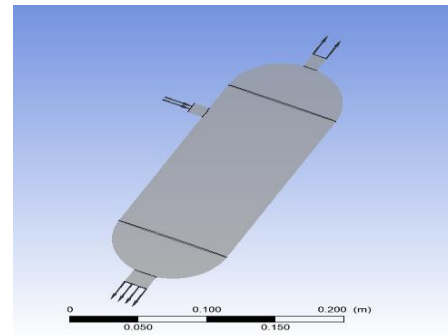
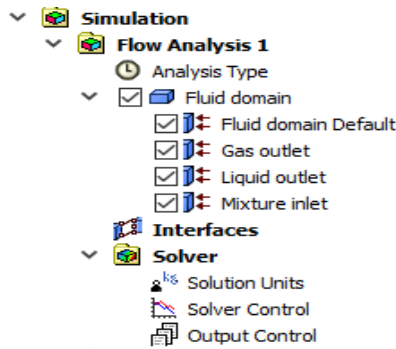
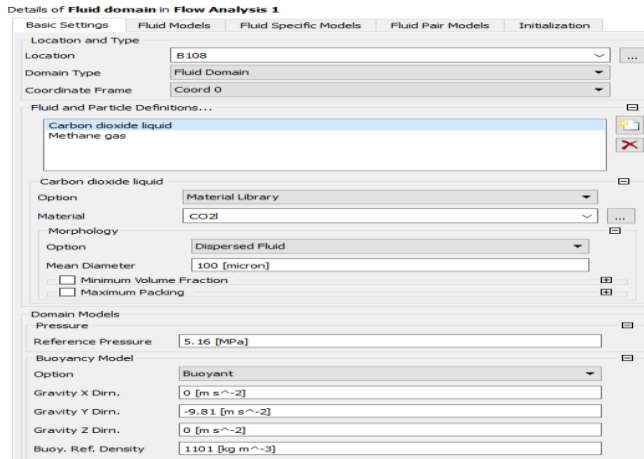


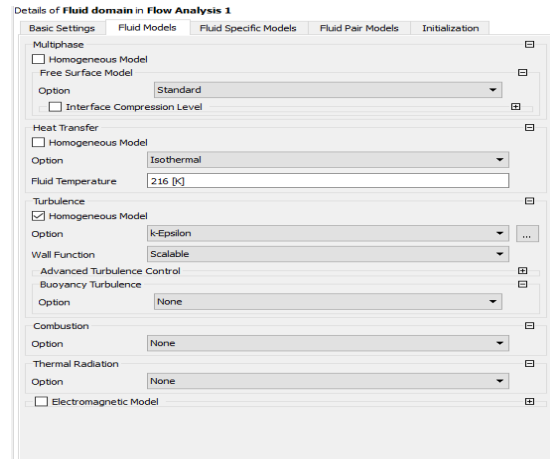
Figure 5-37 a) Problem setup tree and b) fluid domain with the boundary conditions

The fluid domain section has various panels to setup multi-phase problem such as basic settings, fluid models, fluid specific models, fluid pairs, initialization. The fluid material, domain properties are assigned in basic settings panel as shown in figure 5-38 (a). The fluid model section is to select the model for analysis. The available models in this panel are multiphase, heat transfer, turbulence, combustion, and thermal radiation. Figure 5-38 (b), shows the models used in the analysis. The fluid specific models are used to assign fluid buoyancy model for individual fluid, density difference model

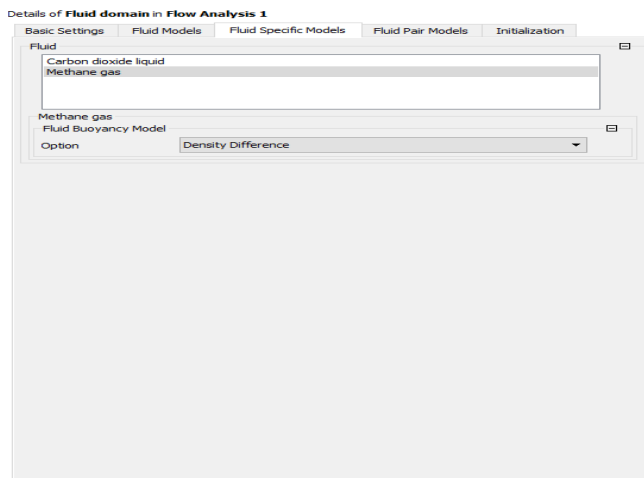
is chosen as shown in figure 5-38 (c). The fluid pair model defines the interface between gas molecule and liquid droplet as shown in figure 5-38 (d).



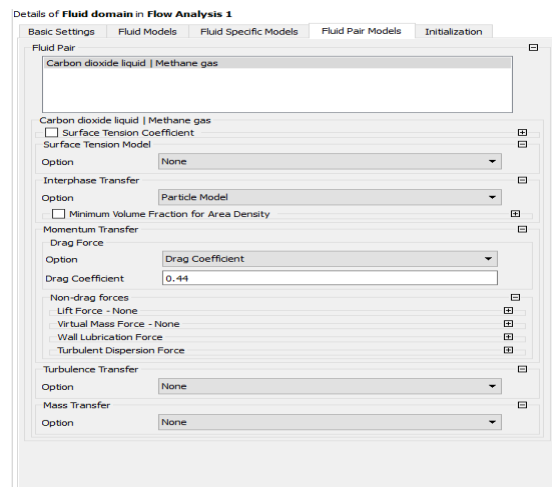
a) Basic domain settings.



b) Fluid models.



c) Fluid specific models.



d) Fluid pair models.

Figure 5-38 Fluid domain setup

The next step is to assign the boundary conditions. As shown in Figure 5-37 (b), the present model has three boundaries such as Mixture inlet, Gas outlet and Liquid outlet. The boundary conditions are tabulated in the table 5-21.

Table 5-21 Boundary conditions

Input	Mixture inlet	Gas outlet	Liquid outlet
Flow regime	Subsonic	Subsonic	Subsonic
Mass and momentum	Fluid dependent	Degassing Condition	Fluid dependent
Inlet CO ₂ velocity	0.063 m/s
Inlet CH ₄ velocity	0.206 m/s
Inlet CO ₂ volume fraction	0.23
Inlet CH ₄ volume fraction	0.76

Figures 5-39 & 5-40 shows the velocity vectors of CH₄ gas and CO₂ liquid. It can be observed that the velocity vectors moving in the upward direction in Figure 5-39 and downward direction in Figure 5-40. This indicates the separation of liquid from the gas. The maximum gas velocity is observed in gravity liquid separation section at an interface between liquid and gas. The figures 5-39 & 5-40 also shows the velocity of the CH₄ gas and CO₂ liquid in gas gravity separation section using a probe. It can be clearly seen that maximum velocity is observed for CO₂ liquid at the same location of CH₄ gas.

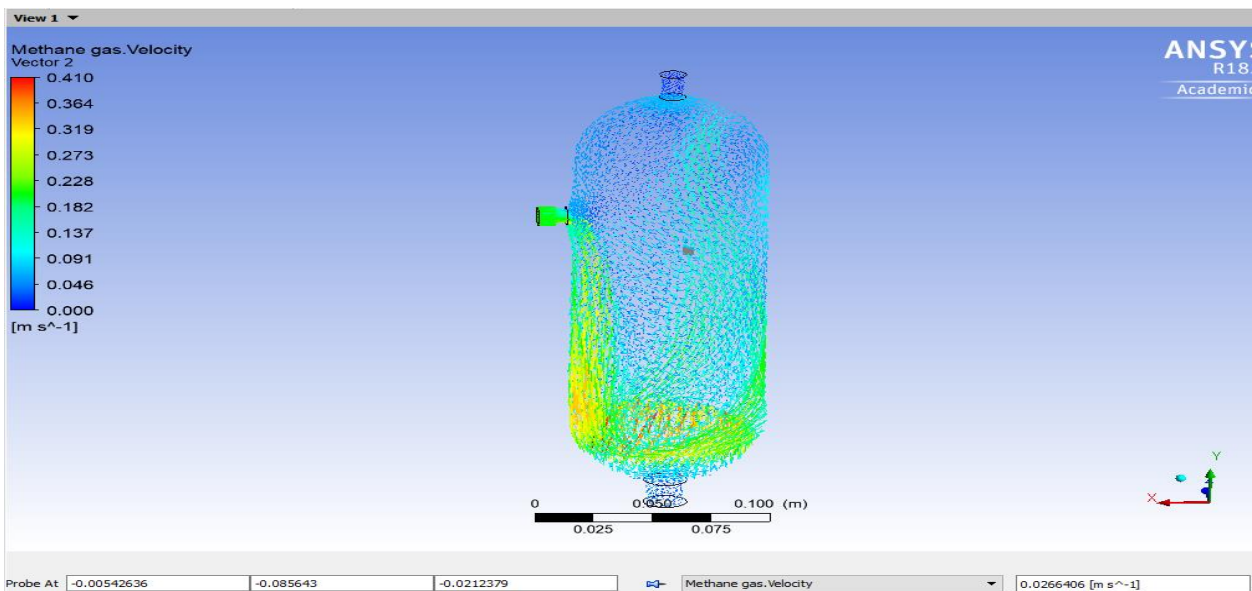


Figure 5-39 Velocity vectors of CH₄ gas

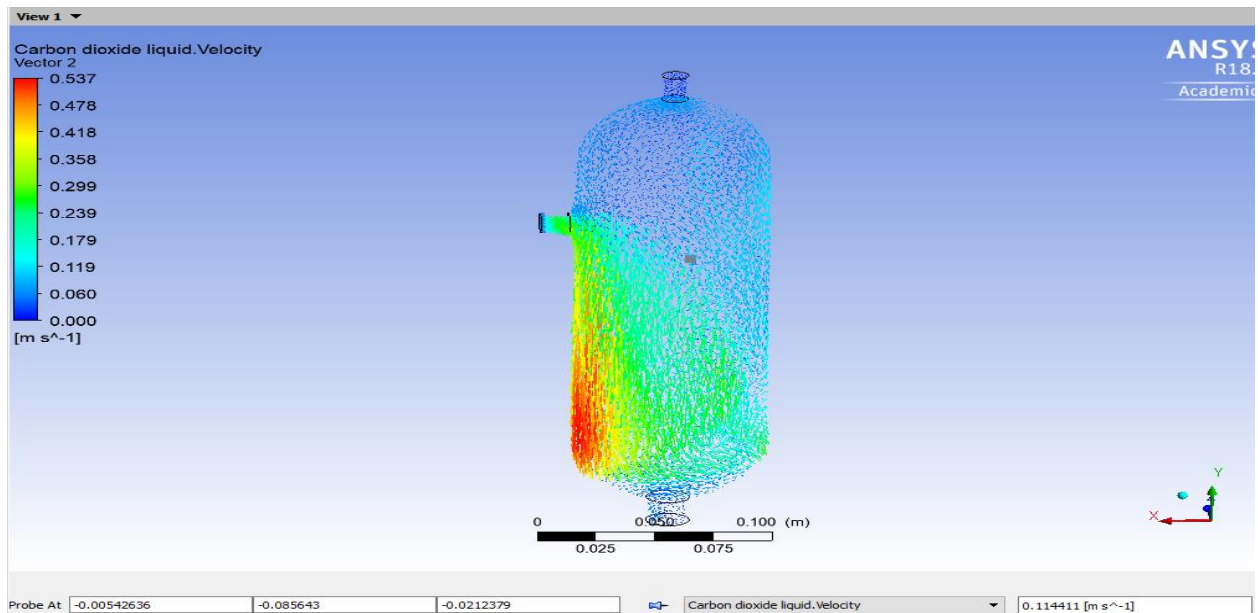


Figure 5-40 Velocity vectors of CO₂ liquid

Figure 5-41 shows the volume fractions of CH₄ gas and CO₂ liquid. The maximum CO₂ volume fraction is observed at the bottom of the vessel whereas, the maximum CH₄ volume fraction observed at the top of the vessel. Based on the velocity vector and volume fraction results, the design is valid.

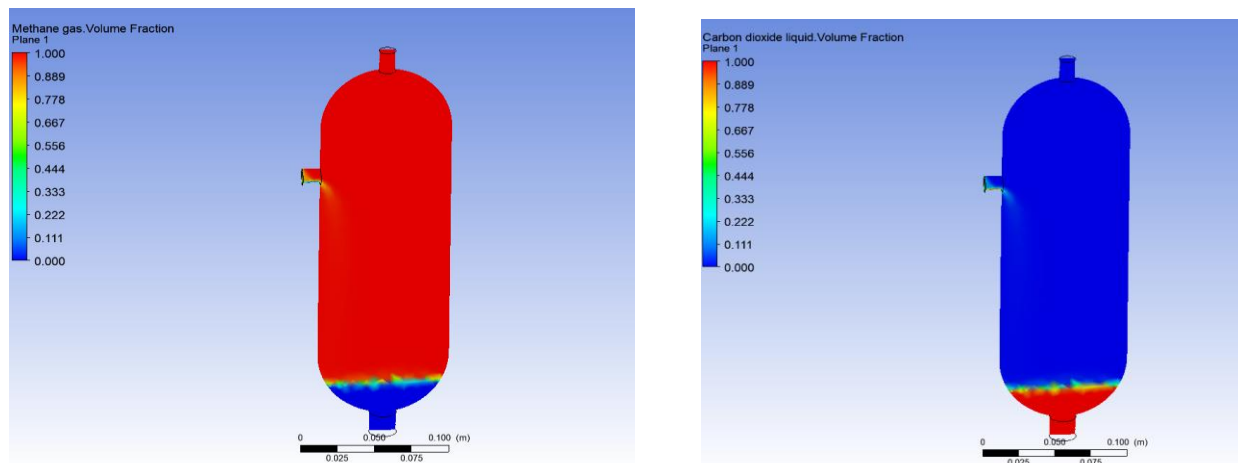


Figure 5-41 Volume fraction of CH₄ gas and CO₂ liquid

5.5 Light-weight storage tank design and FEA composite analysis

Although the storage tank is not an integral part of the system the design of light - weight storage tank is critical for the system to make it marketable. The aim of this section is to design a light – weight storage tank to store biomethane at 22.06 MPa (CNG quality). The CNG pressure vessels are verified for the proposed design in order to store biomethane at CNG quality. Typical CNG pressure vessel types available in the market are shown in Figure 5-42.

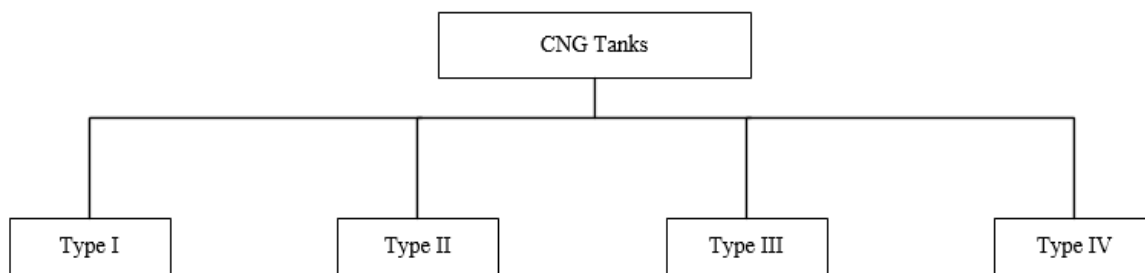


Figure 5-42 Types of CNG pressure vessels

Type I storage tanks are constructed with metals, the typical material used for these type of pressure vessels is CrMo steel. These are less expensive, which has 93 % market share throughout the world. These tanks weigh approximately 1.4 kg/L. Type II storage tanks are constructed by metal liner reinforced with resin impregnated continuous composite fiber overwrap in the hoop direction. Equal loads are shared by the metal liner and composite material. Generally, CrMo or steel/aluminum metal liner with glass fiber composite is used for construction. These vessels share 4% worldwide market and weigh 0.84 kg/L. Type III gas storage tanks are also constructed by the metal liner reinforced with resin impregnated composite fiber but with fully overwrapped in all directions. The typical materials used for the liner and the composite wrap are aluminum and carbon/glass fiber composites. In this, composite material carries 80 % and the metal liner carries 20 % load. The typical specific weight is 0.54 kg/L. Type IV pressure vessel is constructed with resin impregnated continuous

filament with a non-metallic liner typically, high – density polyethylene (HDPE) with carbon fiber composite. These are the lightest CNG vessel weighing 0.39 kg/L [17][40].

5.5.1 Design

The first step in Light – weight storage tank design is to identify the required volume based on the fluid properties inside the tank as shown in table 5-22.

Table 5-22 Design parameters of storage tank

Property	Value
Working pressure (P_w)	22.06 MPa
Working temperature (T)	300 K
Gas constant of biomethane (R)	518.3 J/kg*K
Mass of biomethane (m)	4 kg

The required volume is calculated by

$$V = \frac{\text{Mass } (m)}{\text{Density } (\rho)} \quad (5.68)$$

The density can be determined by the ideal gas equation as

$$\rho = \frac{p}{R T} \quad (5.69)$$

Table 5-23 shows the weight of each tank type for the proposed system calculated based on the specific volume and required tank volume.

Table 5-23 CNG tank weight

CNG tank type	Weight
Type I	38.34 kg
Type II	23 kg
Type III	14.78 kg
Type IV	10.68 kg

Though type IV tank is lighter among all the CNG tanks, Type III is chosen for the design. This is because most of the developing countries use Liquid propane gas (LPG) for their household energy needs. Once it compressed the proposed biomethane has almost equal energy as LPG. The typical dry LPG tank weighs 15 to 18 kg with a volume of 27 to 32 L.

Later, the inner radius required for the storage tank is calculated, by selecting the storage tank shape. Generally, the pressure vessels are available in cylindrical and spherical shape. The spherical shape is chosen for the proposed design. These are twice as efficient as cylindrical vessels in terms of wall thickness. It allows half the wall thickness as in the wall of cylindrical pressure vessel [41]. The required radius is calculated from volume (V) using the spherical geometric relation as

$$r = \left(\frac{3}{4\pi} V\right)^{\frac{1}{3}} \quad (5.70)$$

Material selection is vital for the design. The typical materials used for type III tank are aluminum metal liner and Glass/Carbon fiber composite wrap. Generally, the composite is a combination of two or more individual structural material reinforced together to get high strength. The reinforcement of dissimilar materials forms the fiber and these fibers are glued together by high strength epoxy (typically epoxy) to make the composite material. The composite materials are classified into two types such as the Carbon Fiber Reinforcement Plastic (CFRP) and Glass Fibre Reinforcement Plastic (GFRP) [42]. The properties of CFRP and GFRP are shown in Table 5-23.

Table 5-24 Properties of CFRP and GFRP

Property	CFRP	GFRP
Density (ρ)	1518 kg/m ³	2000 kg/m ³
Yield stress ($\sigma_x, \sigma_y, \sigma_z$)	1632 MPa, 34 MPa, 34 MPa	1100 MPa, 35 MPa, 35 MPa
Young's modulus (E_x, E_y, E_z)	123 GPa, 7.7 GPa, 7.7 GPa	45 GPa, 10 GPa, 10 GPa
Shear modulus (G_{xy}, G_{yz}, G_{xz})	5 GPa, 3 GPa, 5 GPa	5 GPa, 3.8 GPa, 5 GPa
Poisson's ratio ($\nu_{xy}, \nu_{yz}, \nu_{xz}$)	0.27, 0.42, 0.27	0.3, 0.4, 0.3
Minimum burst ratio	2.35	3.65

The Carbon fiber reinforcement plastic (CFRP) is chosen for its high strength and less density over Glass fiber reinforced plastic. The properties of the aluminum liner are shown in Table 5-24.

Table 5-25 Properties of the aluminum liner

Properties	Value
Density (ρ)	2770 kg/m ³
Tensile yield strength (σ_{ty})	280 MPa
Tensile ultimate strength (σ_{tu})	310 MPa
Compressive yield strength (σ_{cy})	280 MPa
Young's modulus (E)	71 GPa
Bulk modulus (G)	69 GPa
Shear modulus (K)	26 GPa
Poisson's ratio (ν)	0.33

Safety is of primary concern in the design of high-pressure gas storage tank, the failure of storage tanks leads to loss of life, health hazards and property damages. There are various national and international safety standards and codes used for design, testing, inspection, and maintenance. The ASME Boiler Pressure Vessel Section VIII, Division III code is used in the proposed design. The

ASME code indicates minimum metal liner thickness for Type III CNG pressure vessel as 6mm. The pressure capability of a liner is calculated using

$$P_l = \frac{2 \sigma_{yield} t_l}{r} \quad (5.71)$$

The pressure vessel is designed to withstand the burst pressure of the composite material. The burst pressure of the required pressure vessel is calculated using burst ratio (2.35 for carbon composite) of the composite material [43]. The burst pressure of the required pressure vessel is

$$P_{burst} = 2.35 P_w \quad (5.72)$$

The design pressure (P_c) of the composite overwrap is calculated from liner pressure capacity which is

$$P_c = P_{burst} - P_l \quad (5.73)$$

The design pressure of the carbon fiber composite overwrap is 34.05 MPa.

The effective thickness of the carbon fibre composite for design pressure can be calculated based on the ASME, Section VIII, Division I.

$$t = \frac{P_c r}{2 \sigma_c E - 0.2 P_c} \quad (5.74)$$

Where,

P_c is the composite design pressure

r is inner radius of the pressure vessel

σ_c is quasi-isotropic strength of the composite ($\frac{\sigma_x}{2}$)

E is the joint efficiency (assumed as 1)

The manufacturing of a composite pressure vessel is different from the typical metal pressure vessel. The filament winding – process is widely used in composite pressure vessel manufacturing. In this process filament winding consists of winding resin impregnated fibers of CFRP/GFRP form plies or laminates of some angle (ranging from 45^0 to 88^0) on a rotating mandrel. Mukund Kavekar et al. suggested an optimum 54^0 winding angle based on FE analysis. The liner thickness is kept constant throughout the spherical pressure vessel but at the polar opening full metal is used because of the practical winding difficulties. The thickness of the polar opening is calculated using

$$t = \frac{P_{burst} r}{2 \sigma_{tu} E - 0.2 P_{burst}} \quad (5.75)$$

The final properties of the pressure vessel are shown Table 5-25.

Table 5-26 Final properties of the pressure vessel

Properties of the vessel	Value
Volume	28.19 L
Inside radius	188.88 mm
Hydrostatic pressure	28.682 MPa
Burst pressure	51.84 MPa
Liner thickness	6 mm
Pressure capability of liner	17.797 MPa
Pressure capability of composite	34.05 MPa
Composite thickness	4.08 mm
Total thickness	10.08 mm
Thickness at the polar opening	15.90 mm

CAD modeling of the spherical pressure vessel as shown in Figure 5-43.

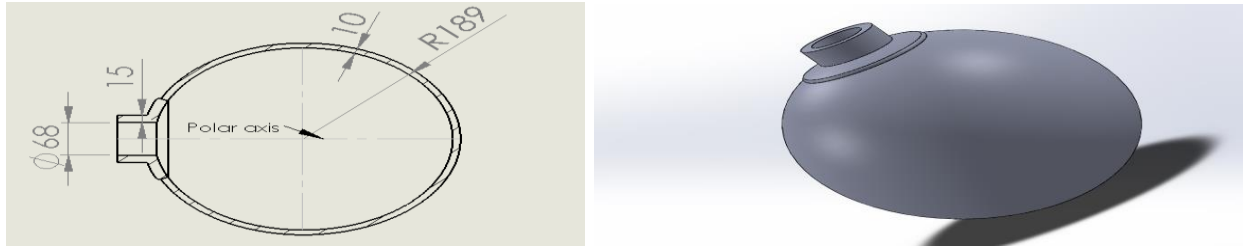


Figure 5-43 2D and 3D model of the spherical pressure vessel

5.5.2 FEA composite analysis

The Composite analysis is performed to validate the design using ANSYS workbench 18.2. The figure 5-44 shows the ANSYS project schematic.

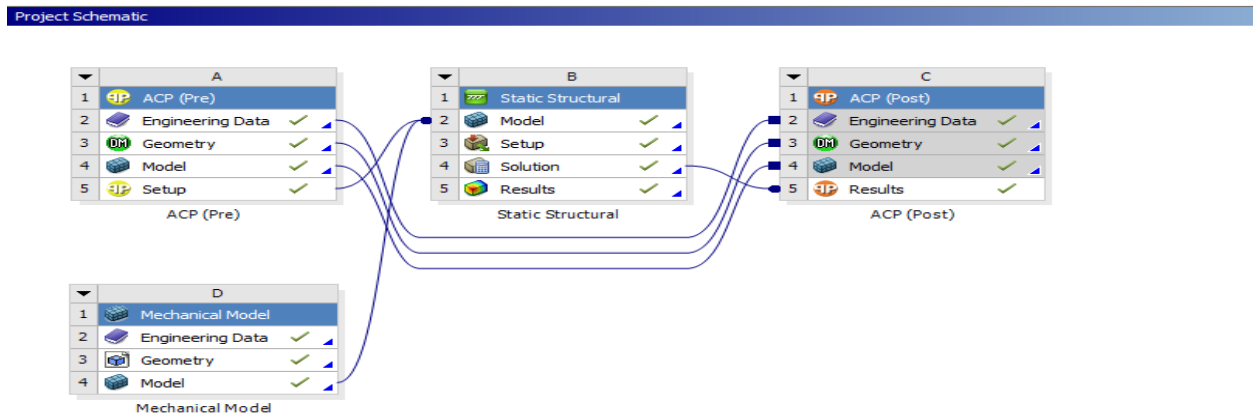


Figure 5-44 ANSYS project schematic

The components used in the present analysis are ANSYS Composite Pre (ACP-pre), Mechanical model, Static Structural, and ANSYS Composite post (ACP-post). ANSYS Composite PrePost is specially designed to set up the composite model, it allows the user to input the number of plies, ply sequence, winding angle, etc. In this analysis, this component is used to set up the composite part of the pressure vessel. The mechanical model is used to set up the solid part of the vessel. The composite and solid models are merged in Static-Structural component to analyze it for specific boundary conditions.

The first step in ANSYS Composite Pre (ACP-pre) is to assign material data to project schematic from pre-defined Engineering Data Source library. The materials, Aluminum alloy (for metallic liner), Epoxy Carbon UD (230 GPa) wet (for composite laminate), Resin epoxy (to layup the plies) and the Aluminum alloy (for metallic polar opening) are assigned. Figure 5-45, shows the material assigned to ACP-Pre model and material assigned to the mechanical model.

Outline of Schematic A2: C2: Engineering Data					
	A	B	C	D	E
1	Contents of Engineering Data			Source	Description
2	Material				
3	Aluminum Alloy			Ger	General aluminum alloy. Fatigue properties come from MIL-HDBK-5H, page 3-277.
4	Epoxy Carbon UD (230 GPa) Wet			Con	
5	Resin Epoxy			Con	
*	Click here to add a new material				

Outline of Schematic D2: Engineering Data					
	A	B	C	D	E
1	Contents of Engineering Data			Source	Description
2	Material				
3	Aluminum Alloy			Ger	General aluminum alloy. Fatigue properties come from MIL-HDBK-5H, page 3-277.
*	Click here to add a new material				

Figure 5-45 Materials assigned to ACP-Pre and Mechanical model

Geometry is imported from solid works to ANSYS workbench. ACP-Pre requires the surface geometry to set up the composite ply whereas the Mechanical model requires solid geometry. Figure 5-46(a) & (b) shows the pressure vessel surface imported to ACP-Pre and the solid pressure vessel imported to Mechanical Model.

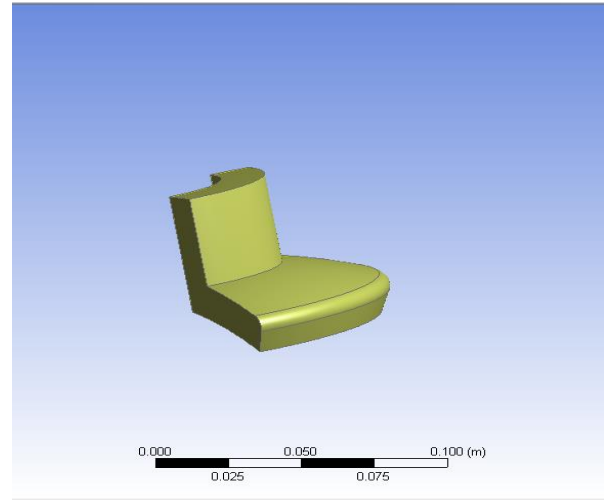
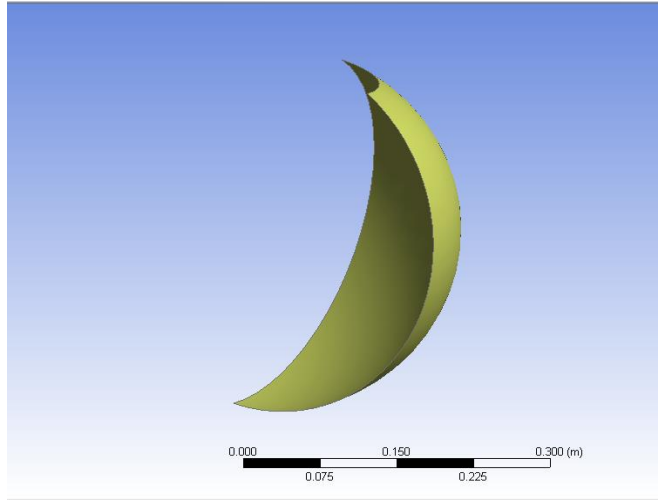


Figure 5-46 a) Pressure vessel surface and b) Solid pressure vessel polar opening

The model is meshed to solve the governing equation. Default fine mesh setup is used in both the models. The mesh is performed only for solid material. A dummy material and thickness is assigned to surface body to avoid errors and this can be corrected by assigning actual metal liner thickness in ACP-pre problem setup step. Figure 5-47 (a) and (b) shows the mesh model of ACP-pre and Mechanical model.

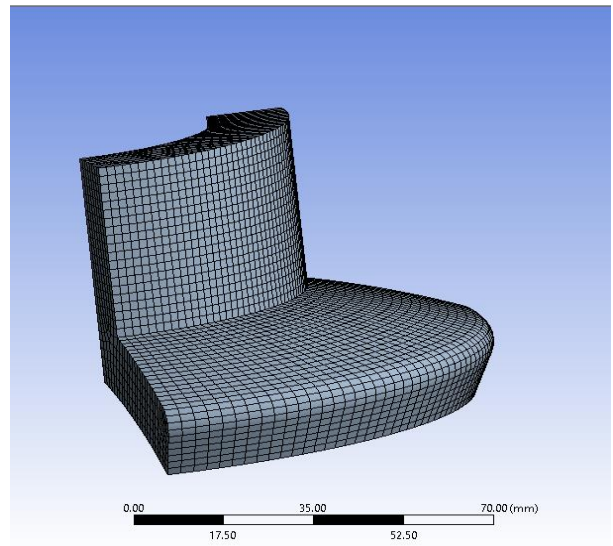


Figure 5-47 a) ACP mesh model and b) Mechanical mesh model

Composite problem setup in ACP-Pre is vital for the analysis as it is aimed to set up laminate ply based on given materials, ply orientation, ply sequence, and winding angle. The first stage in problem setup is to import the material properties to ACP-pre as shown in the top left image of figure 5-48, The next step is to identify and enter fabric thickness in fabric window. The top right image shows the epoxy carbon fabric window. Then the mesh elements are selected from predefined named selection in mesh step. The bottom left figure 5-48 shows the element setup window. Now, the coordinate system is defined for laminate which is shown in the bottom right image in figure 5-48. In the image red arrow shows the laminate wrapping direction, the blue arrow shows the ply direction and the green shows the wrapping angle.

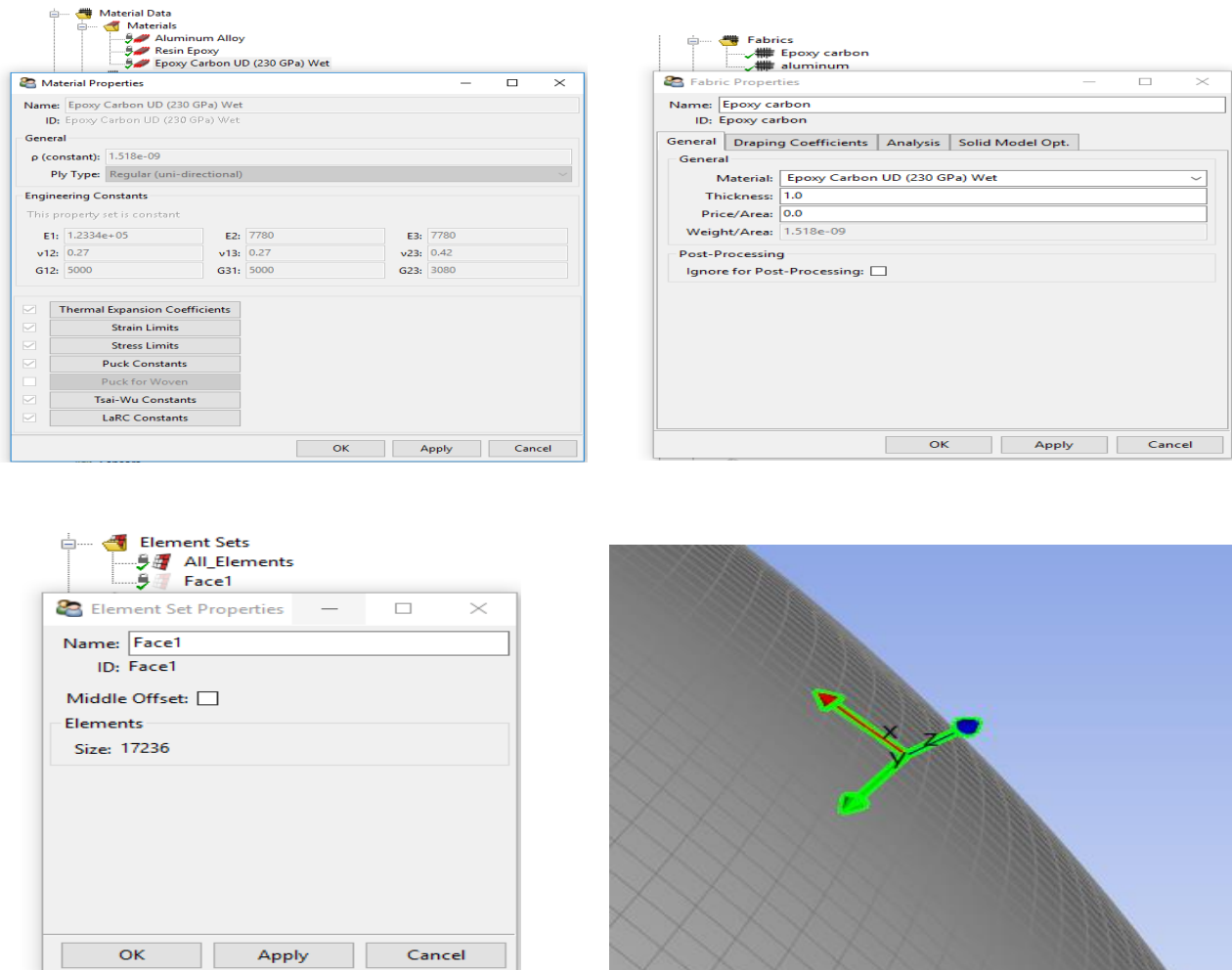


Figure 5-48 ACP problem setup

Once the coordinate system setup is completed the next step is to assign the laminate for each layer by given optimum winding angle. In figure 5-49, the yellow arrow in the top left image shows the laminate wrapping direction, the violet arrow shows the ply direction and the green arrow shows the winding angle. The top right image shows the number of layers on the pressure vessel. The bottom left image shows the composite solid model of five layers (1 metallic layer and 4 composite layers). The bottom right image is the clear view of layers.

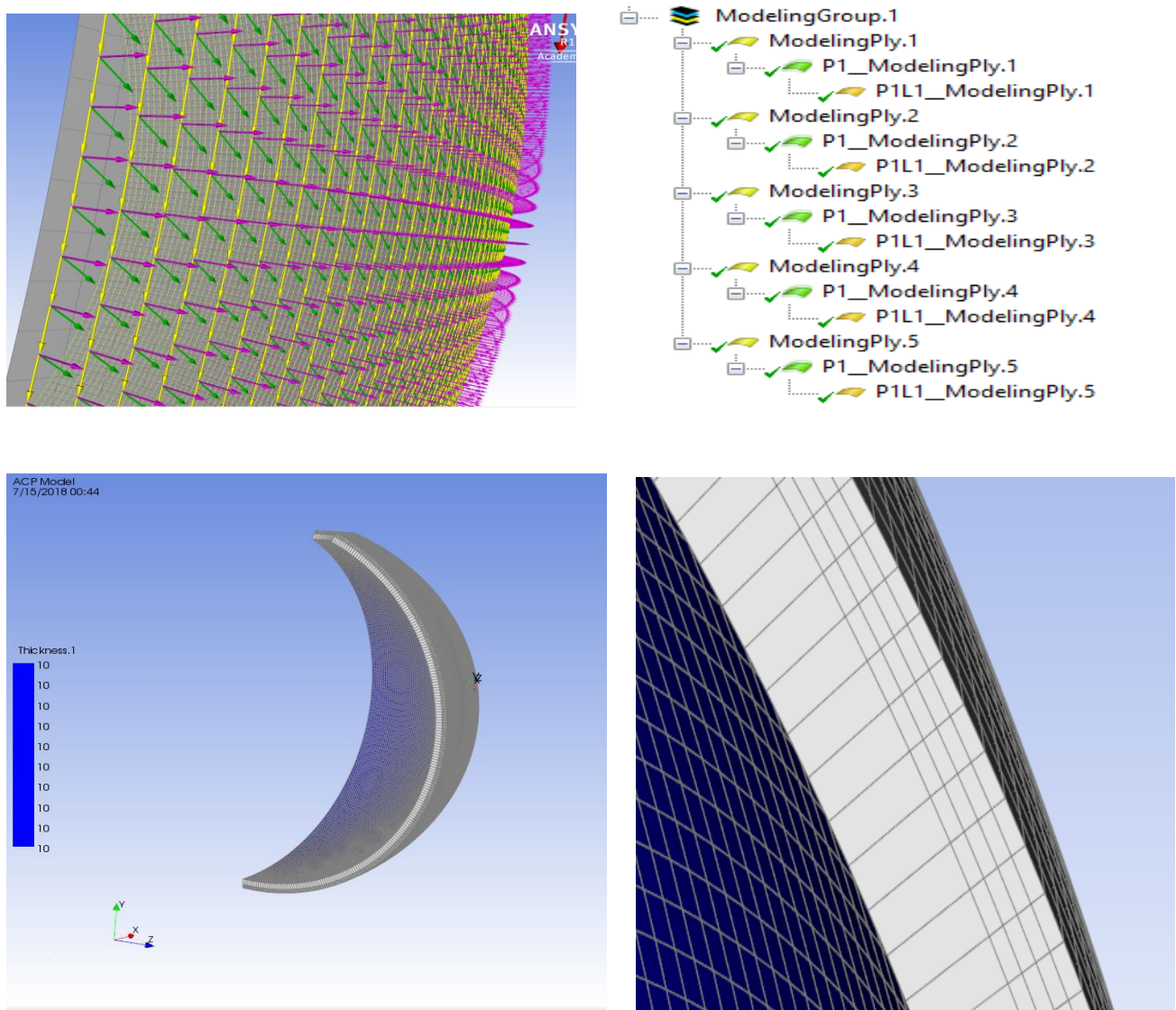


Figure 5-49 Composite laminate

Once the composite model is generated in ACP-Pre, the ACP model and Mechanical Model are merged and transferred to Static structural for further analysis. Figure 5-50 shows the solid model of the pressure vessel merged by two solids.

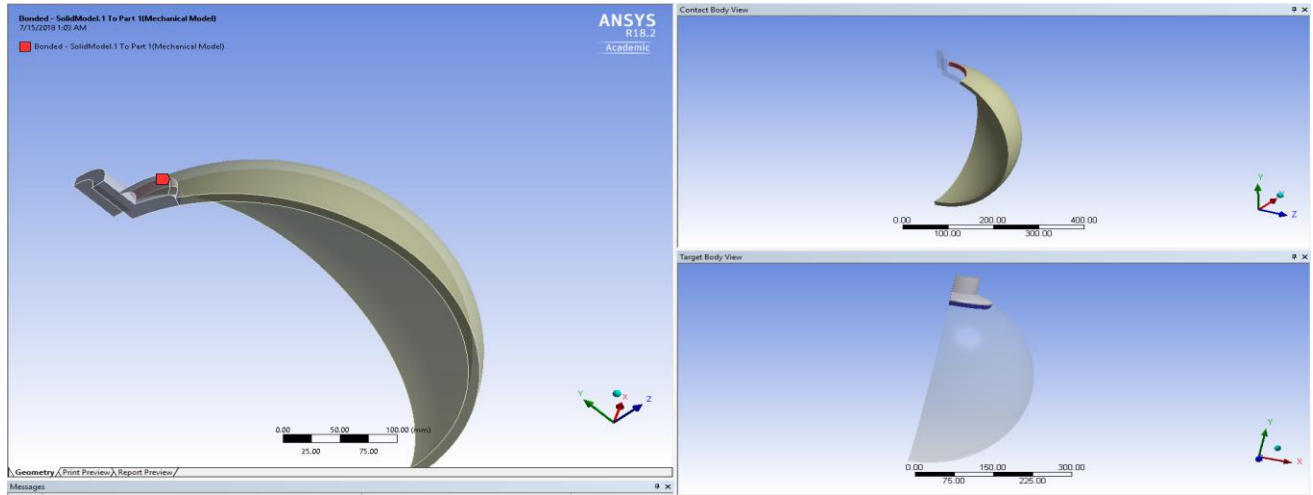


Figure 5-50 ACP-Pre and mechanical model assembly

Boundary conditions and pressures are assigned to solve the FEA model for Von Mises stresses. In Figure 5-51, (a) and (b) boundary conditions and the burst pressure on the pressure vessel.

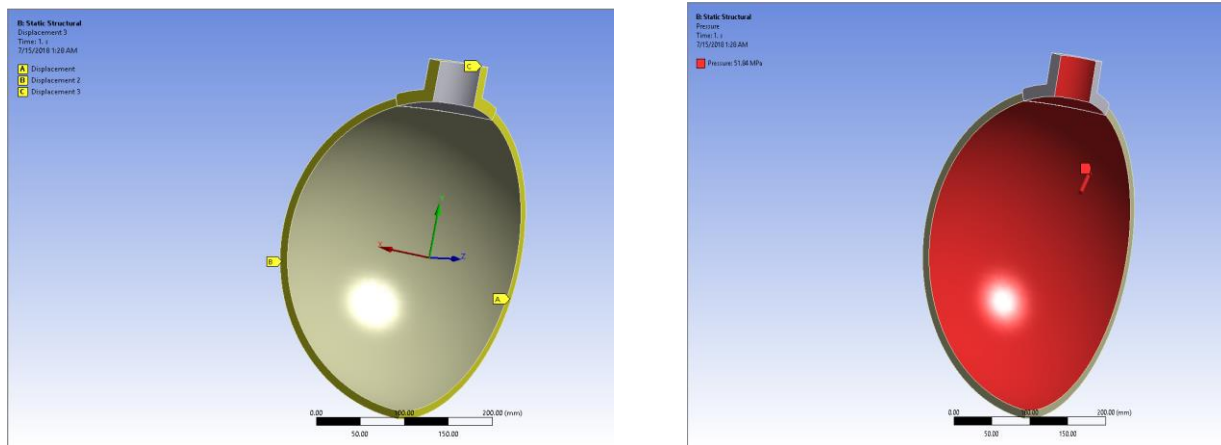


Figure 5-51 a) Boundary conditions and b) Burst pressure

Once the problem setup is completed, the FEA solver solves the governing equations for Equivalent stress and strain, Total deformation, Maximum and Minimum principal stresses, Middle principle stress, Maximum shear stress, Normal stress, and shear stress. The equivalent stress is important to validate the design. For an acceptable composite pressure vessel design the equivalent stress calculated at burst pressure should be less than the quasi-isotropic strength of the material. The figure below shows the equivalent stress variation in the pressure vessel.

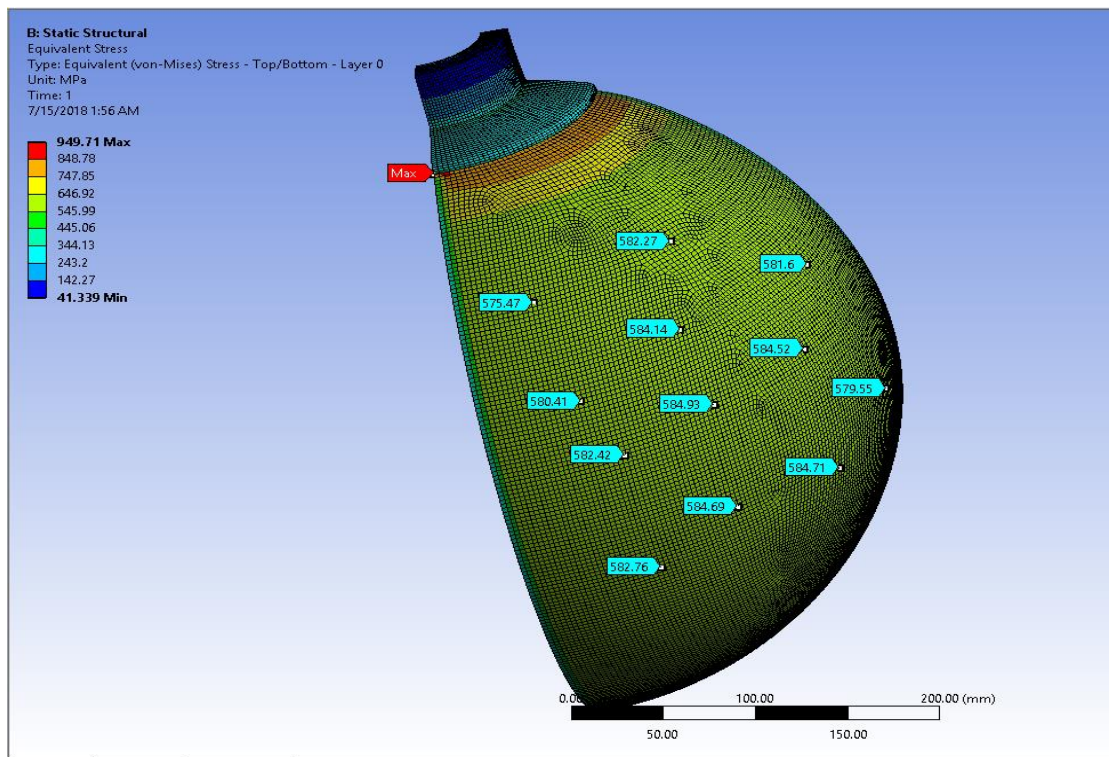


Figure 5-52 Von-Mises stresses of pressure vessel

From Figure 5-52, it can be observed that maximum stress is located at the contact location. This is because of the imperfections in mesh connection. An accurate mesh model needs to be developed for proper element connection. Though the maximum Von Mises stress is 949.71 MPa, the average Von Mises stress is on the composite structure is 580 MPa which is less than 816 MPa (quasi-isotropic strength of the carbine fiber material). So, the design is valid.

6 SUMMARY AND CONCLUSION

The objective of the current study was to propose a commercial portable biogas purification and storage system to commercialize the biogas produced from household/non-commercial biogas plants. The selection of the purification process was based on the portability of the purification system which is completed based on the available commercial purification processes used in the industrial/commercial biogas plants. The literature review concludes the selection of commercial cryogenic purification process with some modification. The commercial cryogenic process relies on the desublimation of CO_2 for the separation of CO_2 from $\text{CO}_2 - \text{CH}_4$ binary mixture whereas the modified cryogenic process was decided to use the condensation of CO_2 . This modification lowers the energy consumption of the system by increasing efficiency, it also gives the flexibility in heat exchanger selection by making it cost effective.

The design of the purification system starts by defining the thermo-physical properties of the biogas and the critical properties of $\text{CO}_2 - \text{CH}_4$ binary mixture. Some of the previous works identified that the influence of lower critical condition of gases influences the higher critical condition of gases in a binary mixture. This influence was successfully quantified by modifying the Peng-Robinson equation of state by including the binary interaction parameters of $\text{CO}_2 - \text{CH}_4$ proposed by various literature. Later, an experiment was designed to validate the modified Peng – Robinson equation of state to use the quantified data in proposed purification system design. The experiment is performed for the pure CO_2 , 80% $\text{CO}_2 - 20\% \text{CH}_4$, and 50% $\text{CO}_2 - 50\% \text{CH}_4$. The data obtained from the experiments were successfully validated the saturated vapor pressures of CO_2 in $\text{CO}_2 - \text{CH}_4$ binary mixture obtained from the Peng – Robinson equation of state.

For a preliminary design, a condensation point was chosen in the liquid region of the equation of state of 50% $\text{CO}_2 - 50\% \text{CH}_4$ mixture. The pressure and temperatures of the selected condensation point is 206 K (-67 °C), 5.65 MPa (748.39 psi) respectively. The operating principle of the proposed system is to compress and cool the biogas to condensation point in the liquid region of CO_2 in $\text{CO}_2 - \text{CH}_4$ binary mixture then the CO_2 changes its phase from gas to liquid. The liquid CO_2 and the gaseous CH_4 will then be separated and the gaseous CH_4 is further compressed to store it in CNG quality. The

components identified in proposed purification system based on the thermodynamic states of the gases explained in Chapter 5.1 are Compressors, Heat exchangers, Liquid – Gas separator, and CH₄ storage tank.

As discussed in the thesis objective the entire purification system (excluding CH₄ storage tank) should be under 15 kg, which a normal person can carry on his/her backpack. All the components were designed to meet this criterion, the mass flow rate of biogas was chosen to be 15 kg/hr (which separates and stores 4 kg/hr methane in CNG quality). Two compressors were decided to use in the system to compress the biogas (compressor 1) and methane (compressor 2) to achieve the required pressure ratio. The major parts of the compressors were designed and validated using FEA structural analysis. The weight of the compressor 1 and 2 we estimated as 3.5 kg and 2 kg respectively.

The proposed purification process requires to cool the biogas from 908.68 K to 206.38 K. It was decided to use two heat exchangers to achieve the required heat dissipation. Chapter 5.3 successfully discussed the design and CFD conjugate heat transfer analysis of heat exchangers. The final heat exchanger (including 1 and 2) assembly weighs 3.7 kg. Liquid-gas separator is the vital part of the system which separates the liquid CO₂ from gaseous CH₄. Chapter 5.4 presented the discussion on design and CFD Multi-Phase analysis of liquid-gas separator. It weighs 0.653 kg. The final component of the system is the CH₄ storage tank. This was designed based on Type III CNG tank; the validation is done by using the FEA Composite analysis. The total weight of the purification system including an estimated piping and control system weights but excluding the storage tank is shown in Table 6-1. The total weight of the system meets the objective with a good margin.

Table 6-1 Weight of portable biogas purification system

Component name	Weight (kg)
Compressor 1 assembly	3.5
Compressor 2 assembly	2
Heat exchanger 1	2.5
Heat exchanger 2	1.2

Table 6-1 – continued

Liquid gas separator	0.653
Piping and control system	2
Total weight	11.853

7 FUTURE SCOPE

The present work successfully identified and proposed a portable purification and storage system for biogas. The preliminary design of the components is completed to meet the design criteria based on various ideal assumptions. This work can be extended to test the proposed cooling system and identify the best alternative cooling methods. Once the cooling system test completed, the next step is to build and test the prototype to validate the purification system design experimentally. The alternative purification methods could also verify for the final product.

REFERENCES

- [1] H. Sulfide, “Biogas bottling in India - a case study,” pp. 1–4, 2008.
- [2] K. Rajendran, S. Aslanzadeh, and M. J. Taherzadeh, *Household biogas digesters-A review*, vol. 5, no. 8. 2012.
- [3] P. C. Narváez Rincón, “The current state of non-conventional sources of energy and related perspectives,” *Ing. e Investig.*, vol. Volumen 30, pp. 165–173, 2010.
- [4] U. Nations, M. Project, and P. Lpg, “Energy for Cooking in Developing Countries,” pp. 419–445, 2006.
- [5] J. Goldemberg, A. K. N. Reddy, K. R. Smith, and R. H. Williams, “Rural energy in developing countries,” *World energy Assess. Energy Chall. Sustain.*, no. 10, pp. 367–384, 2000.
- [6] A. V. Herzog, T. E. Lipman, and D. M. Kammen, “Renewable energy sources,” *Encycl. Life ...*, pp. 1–63, 2001.
- [7] Q. Sun, H. Li, J. Yan, L. Liu, Z. Yu, and X. Yu, “Selection of appropriate biogas upgrading technology-a review of biogas cleaning, upgrading and utilisation,” *Renew. Sustain. Energy Rev.*, vol. 51, no. January, pp. 521–532, 2015.
- [8] A. Damgaard, “Anaerobic Digestion,” no. Mueller 2007, pp. 1–7, 2015.
- [9] L. Chen and H. Neibling, “Anaerobic Digestion Basics,” *Univ. Idaho Ext.*, vol. CIS 1215, pp. 1–6, 2014.
- [10] L. Fuel, “a Green and Low-cost Fuel for Automobiles in India Upgraded Bottled Biogas,” no. April, pp. 20–23, 2014.
- [11] Bharadwaj Kummamuru, “Wba Global Bioenergy Statistics 2017,” p. 80, 2017.
- [12] K. E. H. Warren, “A techno-economic comparison of biogas upgrading technologies in Europe,” *MSc Thesis*, p. 44, 2012.
- [13] J. Stambasky and E. B. A. President, “Biogas & Biomethane in Europe,” 2015.
- [14] B. Overview, N. G. Regulations, N. G. Quiz, and C. Dioxide, “NaturalGas.org,” 2018. [Online]. Available: <http://naturalgas.org/overview/background/>.
- [15] Q. Zhao, E. Leonhardt, C. MacConnell, C. Frear, and S. Chen, “Purification Technologies for Biogas Generated by Anaerobic Digestion,” *Clim. Friendly Farming Improv. Carbon Footpr. Agric. Pacific Northwest. CSANR Res. Rep. 2010-00*, p. 24, 2010.
- [16] E. Ryckebosch, M. Drouillon, and H. Vervaeren, “Techniques for transformation of biogas to

- biomethane,” *Biomass and Bioenergy*, vol. 35, no. 5, pp. 1633–1645, 2011.
- [17] R. M. Kapoor and V. K. Vijay, “Evaluation of Existing Low Cost Gas Bottling Systems for Vehicles Use Adaption in Developing Economies,” p. 59, 2013.
 - [18] V. K. Vijay, R. Chandra, P. M. V Subbarao, and S. S. Kapdi, “Biogas Purification and Bottling into CNG Cylinders : Producing Bio-CNG from Biomass for Rural Automotive Applications,” *Second Jt. Int. Conf. Sustain. Energy Environ.*, vol. 3, no. November, pp. 1–6, 2006.
 - [19] A. Srichat, R. Suntivarakorn, and K. Kamwilaisak, “ScienceDirect A Development of Biogas Purification System Using Calcium Hydroxide and Amine Solution,” vol. 138, pp. 441–445, 2017.
 - [20] E. Akila, S. Pugalendhi, and G. Boopathi, “Biogas Purification using Coconut Shell Based Granular Activated Carbon by Pressure Swing Adsorption,” vol. 6, no. 4, pp. 1178–1183, 2017.
 - [21] V. Vrbova and K. Ciahotny, “Upgrading Biogas to Biomethane Using Membrane Separation,” 2017.
 - [22] A. Ali, “Energy Minimization in Cryogenic Packed Beds during Purification of Natural Gas with High CO₂ Content,” no. 10, pp. 1675–1685, 2014.
 - [23] S. S. Yaru, I. K. Adegun, and M. A. Akintunde, “Characterization and Determination of Some Thermo – Physical Properties of Cattle Dung Biogas,” *Appl. Sci. Reports*, vol. 9, no. 1, 2015.
 - [24] A. Malachowska, “Analysis of the cold gas spraying process and determination of selected properties of metallic coatings Aleksandra Malachowska To cite this version : HAL Id : tel-01741350 Faculté des Sciences et Techniques de Limoges Analysis of the cold gas spraying pro,” 2018.
 - [25] I. Urieli and F. M. White, “Dynamic Viscosity of Ideal Gases , Sutherland Model,” pp. 6–7, 2018.
 - [26] S. K. Fateen, M. M. Khalil, and A. O. Elnabawy, “Semi-empirical correlation for binary interaction parameters of the Peng – Robinson equation of state with the van der Waals mixing rules for the prediction of high-pressure vapor – liquid equilibrium,” pp. 137–145, 2013.
 - [27] G. Xu, F. Liang, Y. Yang, Y. Hu, K. Zhang, and W. Liu, “An improved CO₂ separation and purification system based on cryogenic separation and distillation theory,” *Energies*, vol. 7, no. 5, pp. 3484–3502, 2014.
 - [28] D. Learning and A. Requirements, “University of nairobi,” no. August, 2006.
 - [29] A. Morriesen and C. J. Deschamps, “Experimental investigation of transient fluid flow and

- superheating in the suction chamber of a refrigeration reciprocating compressor,” *Appl. Therm. Eng.*, vol. 41, pp. 61–70, 2012.
- [30] P. Heinz, *No Title*. .
- [31] Z. S. Filipi and D. N. Assanis, “The effect of the stroke-to-bore ratio on combustion, heat transfer and efficiency of a homogeneous charge spark ignition engine of given displacement,” *Int. J. Engine Res.*, vol. 1, no. 2, pp. 191–208, 2000.
- [32] I. Combustion and E. Parts, “32 1125 32.1.”
- [33] L. Vegi and V. Vegi, “Design and analysis of Connecting rod using forged steel,” *Int. J. Sci. Eng. ...*, vol. 4, no. 6, pp. 2081–2090, 2013.
- [34] I. S. O. Designation, “Compressor oils.”
- [35] R. K. Sinnott, J. M. Coulson, J. F. Richardson, and C. & Richardson ’s, “(a) Plat and frame exchanger,” *McGraw-Hill Sci.*, vol. 6, no. 11, pp. 66–81, 2005.
- [36] F. Mueller, “FUNDAMENTALS OF GAS SOLIDS / LIQUIDS Fundamentals of Gas Solids / Liquids Separation.”
- [37] A. Pall, “□ 1/13,” pp. 1–13, 2018.
- [38] F. G. Russell, S. Adler, L. R. Albaugh, and G. J. Aldana, “GPSA Engineering Data Book,” *Gas Process. Suppliers Assoc.*, p. 821, 2004.
- [39] T. Uki, S. T. Sarda, and T. Mathew, “Design of Gas-Liquid Separator for Complete Degasing,” *Int. J. Chem. Eng. Aplpications*, vol. 3, no. 6, pp. 477–480, 2012.
- [40] M. LEGAULT, “Pressure vessel tank types,” pp. 1–3, 2012.
- [41] A. Ibrahim, Y. Ryu, and M. Saidpour, “Stress Analysis of Thin Walled Pressure Vessels,” *Mod. Mech. Eng.*, no. February, pp. 1–9, 2015.
- [42] O. F. Mechanical, “Ijmet © I a E M E Design , Fabrication and Testing of a Modified Single,” pp. 8–14, 2013.
- [43] V. B. Chandran, S. B. Tiwari, R. Suresh, C. K. Krishnadasan, B. Sivasubramonian, and A. S. Kumar, “Design and Analysis of Composite Overwrapped Pressure Vessel,” *Proc. Int. Conf. Mater. Futur. - Innov. Mater. Process. Prod. Appl.*, pp. 109–114, 2013.